

京都大学大学院工学研究科  
社会基盤工学専攻修士論文  
平成24年2月



Master's Thesis  
Department of Civil and Earth Resources Engineering  
Graduate School of Engineering  
February 2012

---

# Large displacement formulation of beam and its application to dynamic soil-structure interaction analysis

京都大学大学院 工学研究科 社会基盤工学専攻

防災工学講座 地盤防災工学分野

Frederico Furst Bittencourt

## Abstract

In January 12 of 2007, a crater 30m deep and 80m wide was suddenly created in the middle of the city of Sao Paulo, Brazil. This happened on top of the construction site of the Sao Paulo subway, during the rainy season. This accident is an example of the many accidents presenting anecdotal evidence that currently adopted small displacement finite element analyses may not be enough. In order to start tackling this problem within the context of soil-structure interaction (SSI) finite element analysis (FEA), the present work proposes a couple of large displacement formulations of beams. These beams were formulated and implemented in FEA-capable software (more specifically, FLIP), and subjected to a battery of analyses meant to validate their usability, and to explore their caveats and benefits. The occurrence of buckling was also investigated, as were the basic assumptions underlying beam theory. Finally, soil-structure interaction analysis was also conducted as means of comparison between formulations, and results point to the worthiness of the proposed formulations.

# TOC

1	Introduction.....	1
1.1	Background.....	1
1.2	Objectives and methodology .....	1
1.3	Structure.....	1
2	Formulations.....	3
2.1	Overview .....	3
2.2	Step-by-step formulation walkthrough .....	3
2.2.1	Total Lagrangian for small rotations (TLsmall) .....	4
2.2.2	Total Lagrangian for finite rotations (TLfinite).....	12
2.2.3	Brief comment on formulations.....	20
2.3	Afterword on Implementation Issues .....	20
3	Validation.....	21
3.1	Overview of validation methodology.....	21
3.1.1	Mesh Types .....	21
3.1.2	Element Formulation Types.....	23
3.1.3	Loading Modes .....	23
3.1.4	Position .....	24
3.1.5	Material Properties .....	25
3.2	Moment analysis.....	26
3.2.1	Displacements .....	26
3.2.2	Strains.....	28
3.2.3	Stresses.....	29
3.2.4	Position .....	31
3.3	Shear analysis .....	33
3.3.1	Displacements .....	33
3.3.2	Strains.....	34
3.3.3	Stresses.....	35
3.3.4	Position .....	37
3.4	Clamped-hinged arch analysis .....	38
3.4.1	Displacements .....	39
3.5	Tentative conclusions.....	41
4	Buckling.....	42
4.1	Overview of buckling methodology.....	42
4.2	Plane Elements Mesh.....	42
4.2.1	Indicators of buckling.....	43

4.2.2	Strains.....	43
4.2.3	Stresses.....	44
4.2.4	Reaction.....	45
4.3	Initial Inspection .....	46
4.3.1	Dynamic analysis and Symmetry .....	46
4.3.2	Displacements .....	46
4.3.3	Strains.....	47
4.3.4	Stresses.....	48
4.3.5	Buckling .....	50
4.4	Refined Inspection .....	54
4.4.1	Determination of critical load .....	55
4.4.2	Batch of analyses .....	58
4.5	Tentative conclusions and critique.....	63
5	Assumptions.....	64
5.1	Coarse analysis .....	64
5.2	Refined analysis.....	68
5.2.1	Curvature .....	72
5.3	Conclusions .....	73
6	SSI analysis.....	74
6.1	Sheetpile Permeability analysis (P-analysis).....	74
6.1.1	Liquefaction modes .....	75
6.1.2	Displacements .....	76
6.1.3	Strains.....	77
6.1.4	Stress.....	79
6.1.5	Moment-curvature diagrams .....	81
6.1.6	Conclusions .....	87
6.1.7	Suggested lines for further inquiry.....	87
6.2	Sheetpile Large Displacement analysis (LD-analysis).....	87
6.2.1	Initial LD-analysis .....	88
6.2.2	Refined LD-analysis .....	91
6.2.3	Conclusions .....	93
7	Conclusions & Afterword.....	94
	References .....	95
	Thanks.....	96

# 1 Introduction

## 1.1 Background

In January 12 of 2007, a crater suddenly took the place of what was Conselheiro Pereira Pinto street in Sao Paulo, Brazil. The accident happened during the rainy season, at the construction site of the Sao Paulo Metro. This is only an isolated event when it comes to its magnitude and its impact on society. However, several smaller accidents presenting problems that involve soil-structure interaction (SSI) occur routinely, and are overlooked as outliers by the local engineering community.

A numerical analysis to predict and avoid such a disaster would have to account for large displacements. More specifically, the scope of this particular work is to formulate a beam element that accounts for large displacements and for the buckling one might expect to occur in such SSI analysis.

## 1.2 Objectives and methodology

This work's objective is to initiate the exploration of the largely unexplored domain of large displacement SSI analysis. This is done by means of undergoing the entire process necessary to implement a fully functional element capable of responding properly to large displacements. Within the background of this research, the element chosen was the beam element.

The goals of this project were pursued with a simple methodology in mind:

1. Formulate it.
2. Implement it.
3. Test it.

Each of these simple steps corresponds to one or several of the chapters presented herein, except for the implementation phase. Chapter 2 presents the two large displacement proposed formulations, and chapters 3 through 6 focus on testing the elements against themselves or against similar elements.

The implementation phase is specific to the software of choice, namely: Finite element analysis program for Liquefaction Process (FLIP). This software was written in FORTRAN, a traditional procedural language in scientific settings. Wherever possible, an object-oriented approach was implemented, with varying degrees of success. Also, numerical tasks that were not required to be processed within FLIP were handled with external software. This external software was Python 2.7, with additional libraries matplotlib, ipython, numpy and scipy.

## 1.3 Structure

This work was divided in two types of chapters: (1) chapters related to the analytical formulation of elements, and (2) chapters that present related groups of analyses-results. Chapter 2 is the only chapter of the first type, and it is comprised of a short overall explanation about the formulation process, followed by a step-by-step formulation of the two proposed beam elements.

Chapter 3 groups analyses that fit in the category of simple cantilever beam analyses aimed at testing the usability of proposed elements and comparing their results with that of similar analyses. Chapter 4 focuses on the buckling behavior of the proposed elements. Chapter 5 takes a slightly different turn, because it is concerned with assessing the validity of the assumption that a beam's cross-section doesn't warp. Chapter 6 explores the manner in which the different behavior of proposed elements affects a full-fledged SSI dynamic analysis. Finally, chapter 7 presents conclusions and a few possible lines for future inquiries.

## 2 Formulations

### 2.1 Overview

The first and foremost step in construing the Finite Element Method (FEM) is formulating the elements which will be simulated. This step is of paramount importance, and a great deal of the complexity of FEM is concentrated in this single step. It is very important to note that the behavior of the large displacement beam formulation can be expected to be quite distinct from the behavior observed in large displacement plane elements, thus the difference in behavior is considered part of the current study.

Mathematically speaking, elements are the domains where certain functions are operated upon. For a typical mechanical element, this is stated in terms of displacements, strains and stresses. Therefore, the entire edifice of FEM rests upon an element's formulation. All element behavior subsequently observed can be traced back to terms within its formulation. The full formulations are presented in section 2.2.

### 2.2 Step-by-step formulation walkthrough

This section presents a short commented walkthrough of a full-fledged formulation. In this particular case, each step must be performed twice: first for the analytical result and second for the discretized result. The discretized result is the most important within the context of the present work, due to the fact that its result is the one that will eventually be implemented in software, and thus generate the numerical results subsequently presented.

1. Define shape functions, i.e. functions that represent the way in which the element is allowed to suffer deformation. In simpler terms, these functions may be thought of as returning the local displacement, when given the nodal displacements for an element.
2. Obtain the strains in the domain of an element using local displacements that can be later calculated from nodal displacements.
3. Obtain the stresses from the strains.
4. Calculate the weak form of the equilibrium equations and integrate them over each element (this can be done using numerical integration methods).
5. This last step is where the element stiffness matrix is calculated, so that it may be coupled to the global stiffness matrix. For large displacement formulations, the stiffness matrix is calculated at each new step, and is commonly called tangent stiffness matrix.

Note that this step-by-step process is not exactly clean or elegant. As a matter of fact, it is quite cumbersome from a mathematical viewpoint, although its results are undeniably valuable. This goes to show that a great deal of the complexity of defining and implementing a FEA-capable formal system and/or software is contained within this phase.

### 2.2.1 Total Lagrangian for small rotations (TLsmall)

The convention adopted throughout this work is loosely based on Holzapfel [1]. Capital letters represent coordinates prior to the occurrence of movement, and small-case letters represent coordinates after movement has occurred. One peculiarity of the beam formulation may be pointed out: the fact that nodal displacements include the rotation angle, thus each node possesses a third degree of freedom besides the two orthogonal displacements. The basic scheme on which this formulation is based can be shown in Fig. 2.1

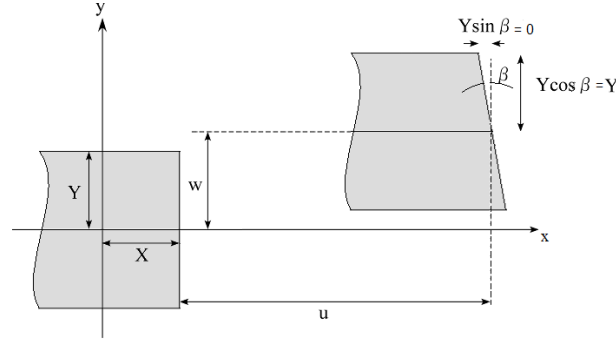


Fig. 2.1 - Schematics for the shape functions utilized in formulation TLsmall.

Coordinates after deformation  $\{x \ y \ z\}^T$ , also known as spatial coordinates, can be obtained from coordinates before deformation  $\{X \ Y \ Z\}^T$ , also known as material coordinates, through the transformation presented in Eqs. 2-1 and 2-2. The former shows the entire transformation, while the latter shows the rotation matrix.

$$\begin{Bmatrix} x \\ y \\ z \end{Bmatrix} = \begin{Bmatrix} X \\ 0 \\ 0 \end{Bmatrix} + \begin{Bmatrix} u \\ w \\ 0 \end{Bmatrix} + \Lambda \begin{Bmatrix} 0 \\ Y \\ Z \end{Bmatrix} = \begin{Bmatrix} X + u(X) - Y \sin(\beta(X)) \\ w(X) + Y \cos(\beta(X)) \\ Z \end{Bmatrix} \quad \text{Eq. 2-1}$$

$$\Lambda = \begin{bmatrix} \cos \beta & -\sin \beta & 0 \\ \sin \beta & \cos \beta & 0 \\ 0 & 0 & 1 \end{bmatrix} \quad \text{Eq. 2-2}$$

The above equation can be denoted in a more compact form by hiding function inputs, see Eq. 2-3. Also, since small rotations are being considered, the simplifications  $\cos \beta \cong 1$  and  $\sin \beta \cong \beta$  can be adopted, further simplifying the deformation function, as shown in Eq. 2-4.



$$\begin{Bmatrix} x \\ y \\ z \end{Bmatrix} = \begin{Bmatrix} X + u - Y \sin \beta \\ w + Y \cos \beta \\ Z \end{Bmatrix} \quad \text{Eq. 2-3}$$

$$\begin{Bmatrix} x \\ y \\ z \end{Bmatrix} = \begin{Bmatrix} X + u - Y \beta \\ w + Y \\ Z \end{Bmatrix} \quad \text{Eq. 2-4}$$

The deformation function can be used to obtain the deformation gradient  $F$ , essential to this formulation. Furthermore, the Green-Lagrange strain tensor  $E$  can be calculated from the deformation gradient as shown in Eqs. 2-5 and 2-6.

$$F(X, t) = \frac{\partial \chi(X, t)}{\partial X} = \nabla_X \chi(X, t) \Rightarrow F = \begin{bmatrix} 1 + u_{,x} - Y \beta_{,x} & -\beta & 0 \\ w_{,x} & 1 & 0 \\ 0 & 0 & 1 \end{bmatrix} \quad \text{Eq. 2-5}$$

$$E = \frac{1}{2} (F^T F - I) = \begin{bmatrix} E_{xx} & E_{xy} & 0 \\ E_{xy} & 0 & 0 \\ 0 & 0 & 0 \end{bmatrix} \quad \text{Eq. 2-6}$$

$$\begin{aligned} E_{xx} &= u_{,x} + \frac{1}{2} (u_{,x}^2 + w_{,x}^2) - Y \beta_{,x} = E^0 - Y K^0 \\ E_{xy} &= \frac{1}{2} (w_{,x} - \beta) = \frac{1}{2} \Gamma^0 \end{aligned} \quad \text{Eq. 2-7}$$

The components of the Green-Lagrange strain can then be broken down into three custom strain components  $E^0$ ,  $K^0$  and  $\Gamma^0$ , as shown in Eq. 2-7. This can be done because there are only three stresses to be considered in the Timoshenko beam: normal stress, shear stress and bending momentum.

Now, for the stresses. The second Piola-Kirchoff stress tensor can be obtained as shown in Eq. 2-8. Forces can now be clearly obtained through the integration of this stress tensor in the domain of the element, as seen in Eqs. 2-9, 2-10 and 2-11. The usual forms of these formulae is then obtained as seen in Eq. 2-12, which relies on terms of the integral being zero for symmetric cross-sections. The term shown in Eq. 2-13 accounts for the appearance of the moment of inertia term in direct relation to bending moment.

$$\begin{aligned} S_{xx} &= E E_{xx} = E (E^0 - Y K^0) \\ S_{xy} &= 2G E_{xy} = G \Gamma^0 \end{aligned} \quad \text{Eq. 2-8}$$

$$P^0 = \int_{A^0} S_{xx} dA^0 = \int_{A^0} E (E^0 - Y K^0) dA^0 = E A^0 E^0 - E K^0 \int_{A^0} Y dA^0 \quad \text{Eq. 2-9}$$

$$S^0 = \int_{A^0} S_{xy} dA^0 = \int_{A^0} G \Gamma^0 dA^0 = \kappa G A^0 \Gamma^0 \quad \text{Eq. 2-10}$$

$$M^0 = - \int_{A^0} S_{xx} Y dA^0 = - \int_{A^0} E (E^0 - Y K^0) Y dA^0 = - E E^0 \int_{A^0} Y dA^0 + E K^0 \int_{A^0} Y^2 dA^0 \quad \text{Eq. 2-11}$$

$$P^0 = E A^0 E^0 \quad \text{Eq. 2-12}$$

$$M^0 = E I^0 K^0$$

$$I^0 = \int_{A^0} Y^2 dA^0 \quad \text{Eq. 2-13}$$

Now we survey the equations of movement for these stresses. Since the present work is focused in the Total Lagrangian formulation, these equations must be represented in material coordinates, as seen in Eqs. 2-14 through 2-16.

$$\frac{\partial P^0}{\partial X} + q_x = \rho^0 A^0 \ddot{u} \quad \text{Eq. 2-14}$$

$$\frac{\partial S^0}{\partial X} + q_y = \rho^0 A^0 \ddot{w} \quad \text{Eq. 2-15}$$

$$\frac{\partial M^0}{\partial X} + S^0 + m_z = \rho^0 I^0 \ddot{\beta} \quad \text{Eq. 2-16}$$

The weak form of these equilibrium equations must be calculated, and this is equivalent to a direct application of the principle of virtual work. The principle of virtual work can be visualized by parts as seen in Eqs. 2-17 through 2-21. Looking at these equations term by term, Eq. 2-18 shows the internal work, Eq. 2-19 shows the inertial work, and Eq. 2-20 represents the Dirichlet boundary conditions.

$$\delta \Pi(u, w, \beta) = \delta W + \delta W_M - \delta \Pi_{ext} \quad \text{Eq. 2-17}$$

$$\delta W = \int_{\Omega_0} S : \delta E dV \quad \text{Eq. 2-18}$$

$$\delta W_M = \int_{L_0} \left[ \delta u (\rho^0 A^0 \ddot{u} - q_x) + \delta w (\rho^0 A^0 \ddot{w} - q_y) + \delta \beta (\rho^0 I^0 \ddot{\beta} - m_z) \right] dX \quad \text{Eq. 2-19}$$

$$\delta \Pi_{ext} = (\delta u \bar{P}) \Big|_{\partial P^0} + (\delta \beta \bar{M}) \Big|_{\partial M^0} + (\delta w \bar{S}) \Big|_{\partial S^0} \quad \text{Eq. 2-20}$$

$$\begin{aligned} \delta \Pi(u, w, \beta) = & \int_{\Omega_0} S : \delta E dV + \\ & + \int_{L_0} \left[ \delta u (\rho^0 A^0 \ddot{u} - q_x) + \delta w (\rho^0 A^0 \ddot{w} - q_y) + \delta \beta (\rho^0 I^0 \ddot{\beta} - m_z) \right] dX \\ & - (\delta u \bar{P}) \Big|_{\partial P^0} - (\delta \beta \bar{M}) \Big|_{\partial M^0} - (\delta w \bar{S}) \Big|_{\partial S^0} \end{aligned} \quad \text{Eq. 2-21}$$

The virtual internal work can then be calculated based on our three custom pairs of strains and stresses, as seen in Eqs. 2-22 through 2-25. In this equation, the virtual strains correspondent to the three custom stress

components can be obtained by computing the variation of Eq. 2-7.

$$\delta W = \int_{L^0} (\delta E^0 P^0 + \delta K^0 M^0 + \delta \Gamma^0 S^0) dX \quad \text{Eq. 2-22}$$

$$\delta E^0 = \delta u_{,X} + u_{,X} \delta u_{,X} + w_{,X} \delta w_{,X} \quad \text{Eq. 2-23}$$

$$\delta K^0 = \delta \beta_{,X} \quad \text{Eq. 2-24}$$

$$\delta \Gamma^0 = \delta w_{,X} - \delta \beta \quad \text{Eq. 2-25}$$

The next step is the discretization of the equations obtained thus far, so as to achieve matrices that are ready to be used in code. Note that these matrices are specific for a two-node element, but the code that was actually implemented is capable of properly handling three-node elements as well. The shape functions and matrix  $N$  can be obtained trivially from the linear shape functions chosen. Refer to Eqs. 2-26 to 2-31 for their explicit matrix form.

$$u = N_u \tilde{u}, \quad w = N_w \tilde{w}, \quad \beta = N_\beta \tilde{\beta} \quad \text{Eq. 2-26}$$

$$N_u = N_w = N_\beta = [N_1 \quad N_2] \quad \text{Eq. 2-27}$$

$$\tilde{u} = \begin{bmatrix} u_1 \\ u_2 \end{bmatrix}, \quad \tilde{w} = \begin{bmatrix} w_1 \\ w_2 \end{bmatrix}, \quad \tilde{\beta} = \begin{bmatrix} \beta_1 \\ \beta_2 \end{bmatrix} \quad \text{Eq. 2-28}$$

$$N_1 = \frac{x_2 - x}{L^0}, \quad N_2 = \frac{x - x_1}{L^0} \quad \text{Eq. 2-29}$$

$$\varphi = N \tilde{\varphi}$$

$$\varphi = [u \quad w \quad \beta] \quad \text{Eq. 2-30}$$

$$\tilde{\varphi} = [u_1 \quad w_1 \quad \beta_1 \quad u_2 \quad w_2 \quad \beta_2]$$

$$N = \begin{bmatrix} N_1 & 0 & 0 & N_2 & 0 & 0 \\ 0 & N_1 & 0 & 0 & N_2 & 0 \\ 0 & 0 & N_1 & 0 & 0 & N_2 \end{bmatrix} \quad \text{Eq. 2-31}$$

The displacement fields in the matrix  $\tilde{\varphi}$  were ordered here in the same manner as they are ordered in the internal vectors of the Fortran FLIP source code. We can now write the stress-displacement matrix for a two-node element, as seen in Eqs. 2-32 to 2-36. Also, note how Eqs. 2-37 to 2-40, summarize the matrix form of the internal virtual work and inertial virtual work.

$$\delta E^0 = (1 + u_{,X}) N_{u,X} \delta \tilde{u} + w_{,X} N_{w,X} \delta \tilde{w} \quad \text{Eq. 2-32}$$

$$\delta \mathbf{K}^0 = N_{\beta, X} \delta \tilde{\beta} \quad \text{Eq. 2-33}$$

$$\delta \mathbf{T}^0 = \delta w_{,X} - \delta \beta = N_{w, X} \delta \tilde{w} - N_{\beta} \delta \tilde{\beta} \quad \text{Eq. 2-34}$$

$$\boldsymbol{\varepsilon}^0 = \begin{Bmatrix} \delta \mathbf{E}^0 \\ \delta \mathbf{K}^0 \\ \delta \mathbf{T}^0 \end{Bmatrix} = \begin{bmatrix} (1+u_{,X})N_{1,X} & w_{,X}N_{1,X} & 0 & (1+u_{,X})N_{2,X} & w_{,X}N_{2,X} & 0 \\ 0 & 0 & N_{1,X} & 0 & 0 & N_{2,X} \\ 0 & N_{1,X} & -N_1 & 0 & N_{2,X} & -N_2 \end{bmatrix} \begin{bmatrix} u_1 \\ w_1 \\ \beta_1 \\ u_2 \\ w_2 \\ \beta_2 \end{bmatrix} \quad \text{Eq. 2-35}$$

$$\mathbf{B} = \begin{bmatrix} (1+u_{,X})N_{1,X} & w_{,X}N_{1,X} & 0 & (1+u_{,X})N_{2,X} & w_{,X}N_{2,X} & 0 \\ 0 & 0 & N_{1,X} & 0 & 0 & N_{2,X} \\ 0 & N_{1,X} & -N_1 & 0 & N_{2,X} & -N_2 \end{bmatrix} \quad \text{Eq. 2-36}$$

$$\delta \Pi_{\text{int}} = \delta W + \delta W_M = \int_{L^0} \begin{bmatrix} \delta \mathbf{E}^0 & \delta \mathbf{K}^0 & \delta \mathbf{T}^0 \end{bmatrix} \begin{bmatrix} \mathbf{P}^0 \\ \mathbf{M}^0 \\ \mathbf{S}^0 \end{bmatrix} dX + \int_{L^0} (N \delta \tilde{\varphi})^T \begin{Bmatrix} \rho^0 A^0 \ddot{u} - q_X \\ \rho^0 A^0 \ddot{w} - q_Y \\ \rho^0 I^0 \ddot{\beta} - m_Z \end{Bmatrix} dX \quad \text{Eq. 2-37}$$

$$\delta \Pi_{\text{int}} = \delta \tilde{\varphi}^T \int_{L^0} \mathbf{B}^T \begin{Bmatrix} \mathbf{P}^0 \\ \mathbf{M}^0 \\ \mathbf{S}^0 \end{Bmatrix} + N^T \begin{Bmatrix} \rho^0 A^0 \ddot{u} - q_X \\ \rho^0 A^0 \ddot{w} - q_Y \\ \rho^0 I^0 \ddot{\beta} - m_Z \end{Bmatrix} dX = \delta \tilde{\varphi} [\hat{W}^0 + \hat{M}^0 \ddot{\tilde{\varphi}} - \hat{f}^0] \quad \text{Eq. 2-38}$$

$$\hat{f}^0 = \int_{L^0} N^T \begin{Bmatrix} q_X \\ q_Y \\ m_Z \end{Bmatrix} dX \quad \text{Eq. 2-39}$$

$$\hat{M}^0 = \int_{L^0} \rho^0 N^T \begin{bmatrix} A^0 & 0 & 0 \\ 0 & A^0 & 0 \\ 0 & 0 & I^0 \end{bmatrix} N dX \quad \text{Eq. 2-40}$$

Then, in order to find the tangent stiffness matrix, the next step is to calculate the increase of the virtual work stationary, as shown in Eq. 2-41. The linear term is then calculated using as shown in Eqs. 2-42 to 2-45.

$$\begin{aligned} \Delta(\delta \Pi_{\text{int}}) &= \delta \tilde{\varphi}^T \int_{L^0} \Delta \mathbf{B}^T \begin{Bmatrix} \mathbf{P}^0 \\ \mathbf{M}^0 \\ \mathbf{S}^0 \end{Bmatrix} + \mathbf{B}^T \begin{Bmatrix} \Delta \mathbf{P}^0 \\ \Delta \mathbf{M}^0 \\ \Delta \mathbf{S}^0 \end{Bmatrix} + N^T \begin{Bmatrix} \rho^0 A^0 \Delta \ddot{u} \\ \rho^0 A^0 \Delta \ddot{w} \\ \rho^0 I^0 \Delta \ddot{\beta} \end{Bmatrix} dX = \\ &= \delta \tilde{\varphi} [\Delta \Pi_{\text{int}}^{NL} + \Delta \Pi_{\text{int}}^L + \Delta \Pi_{\text{int}}^M] \end{aligned} \quad \text{Eq. 2-41}$$

$$\Delta \Pi_{\text{int}}^L = \int_{L^0} B^T \begin{Bmatrix} \Delta P^0 \\ \Delta M^0 \\ \Delta S^0 \end{Bmatrix} dX = \int_{L^0} B^T \begin{bmatrix} EA^0 & 0 & 0 \\ 0 & EI^0 & 0 \\ 0 & 0 & \kappa GA^0 \end{bmatrix} \begin{Bmatrix} \Delta E^0 \\ \Delta K^0 \\ \Delta \Gamma^0 \end{Bmatrix} dX \quad \text{Eq. 2-42}$$

$$\Delta \Pi_{\text{int}}^L = \int_{L^0} B^T DB \Delta \tilde{\phi} dX \quad \text{Eq. 2-43}$$

$$D = \begin{bmatrix} EA^0 & 0 & 0 \\ 0 & EI^0 & 0 \\ 0 & 0 & \kappa GA^0 \end{bmatrix} \quad \text{Eq. 2-44}$$

$$K_T^L = \int_{L^0} B^T DB \Delta \tilde{\phi} dX \quad \text{Eq. 2-45}$$

To account for geometrical non-linearity, the next step is to obtain the nonlinear stiffness matrix. Note how the nonlinearity being taken into account here is geometrical rather than material. Eqs. 2-46 through 2-50 give an overview of how the nonlinear stiffness matrix can be obtained.

$$\Delta B = \begin{bmatrix} \Delta u_{,X} N_{u,X} & \Delta w_{,X} N_{w,X} & 0 \\ 0 & 0 & 0 \\ 0 & 0 & 0 \end{bmatrix} \quad \text{Eq. 2-46}$$

$$\Delta \Pi_{\text{int}}^{NL} = \int_{L^0} \Delta B^T \begin{Bmatrix} P^0 \\ M^0 \\ S^0 \end{Bmatrix} dX = \int_{L^0} \begin{bmatrix} \Delta u_{,X} N_{u,X} & 0 & 0 \\ \Delta w_{,X} N_{w,X} & 0 & 0 \\ 0 & 0 & 0 \end{bmatrix} \begin{Bmatrix} P^0 \\ M^0 \\ S^0 \end{Bmatrix} dX \quad \text{Eq. 2-47}$$

$$\Delta \Pi_{\text{int}}^{NL} = \int_{L^0} \begin{Bmatrix} \Delta u_{,X} N_{u,X} P^0 \\ \Delta w_{,X} N_{w,X} P^0 \\ 0 \end{Bmatrix} dX = \int_{L^0} \begin{bmatrix} N_{u,X} P^0 & 0 & 0 \\ 0 & N_{w,X} P^0 & 0 \\ 0 & 0 & 0 \end{bmatrix} \begin{Bmatrix} \Delta u_{,X} \\ \Delta w_{,X} \\ \Delta \beta_{,X} \end{Bmatrix} dX \quad \text{Eq. 2-48}$$

$$\Delta \Pi_{\text{int}}^{NL} = \int_{L^0} \begin{bmatrix} N_{u,X} P^0 & 0 & 0 \\ 0 & N_{w,X} P^0 & 0 \\ 0 & 0 & 0 \end{bmatrix} \begin{Bmatrix} N_{u,X} \Delta \tilde{u} \\ N_{w,X} \Delta \tilde{w} \\ N_{\beta,X} \Delta \tilde{\beta} \end{Bmatrix} dX = K_T^{NL} \Delta \tilde{\phi} \quad \text{Eq. 2-49}$$

$$K_T^{NL} = \int_{L^0} \begin{bmatrix} N_{u,X} P^0 N_{u,X} & 0 & 0 \\ 0 & N_{w,X} P^0 N_{w,X} & 0 \\ 0 & 0 & 0 \end{bmatrix} dX \quad \text{Eq. 2-50}$$

To be able to utilize this formulation programmatically in software, we now write the discretized version of it for two nodes (in the actual implementation it is also possible to use 3-node elements). At first, Eqs. 2-46 and 2-47 must be taken in their discretized form, that is shown in Eqs. 2-51 through 2-53. This formula can be

further reduced, as shown in Eqs. 2-54 to 2-58. Note that custom matrix  $N_{NL}$  was used for ease of programming.

$$\Delta B = [\Delta B_1 \quad \Delta B_2] \quad \text{Eq. 2-51}$$

$$\Delta B_i = \begin{bmatrix} \Delta u_{,X} N_{i,X} & \Delta w_{,X} N_{i,X} & 0 \\ 0 & 0 & 0 \\ 0 & 0 & 0 \end{bmatrix} \quad \text{Eq. 2-52}$$

$$\Delta \Pi_{\text{int}}^{NL} = \int_{L^0} \Delta B^T \begin{Bmatrix} P^0 \\ M^0 \\ S^0 \end{Bmatrix} dX = \int_{L^0} \begin{bmatrix} \Delta u_{,X} N_{1,X} & 0 & 0 \\ \Delta w_{,X} N_{1,X} & 0 & 0 \\ 0 & 0 & 0 \\ \Delta u_{,X} N_{2,X} & 0 & 0 \\ \Delta w_{,X} N_{2,X} & 0 & 0 \\ 0 & 0 & 0 \end{bmatrix} \begin{Bmatrix} P^0 \\ M^0 \\ S^0 \end{Bmatrix} dX \quad \text{Eq. 2-53}$$

$$\Delta \Pi_{\text{int}}^{NL} = \int_{L^0} \begin{Bmatrix} \Delta u_{,X} N_{1,X} P^0 \\ \Delta w_{,X} N_{1,X} P^0 \\ 0 \\ \Delta u_{,X} N_{2,X} P^0 \\ \Delta w_{,X} N_{2,X} P^0 \\ 0 \end{Bmatrix} dX \quad \text{Eq. 2-54}$$

$$\Delta \Pi_{\text{int}}^{NL} = \int_{L^0} \begin{bmatrix} N_{1,X} P^0 N_{1,X} & 0 & 0 & N_{1,X} P^0 N_{2,X} & 0 & 0 \\ 0 & N_{1,X} P^0 N_{1,X} & 0 & 0 & N_{1,X} P^0 N_{2,X} & 0 \\ 0 & 0 & 0 & 0 & 0 & 0 \\ N_{2,X} P^0 N_{1,X} & 0 & 0 & N_{2,X} P^0 N_{2,X} & 0 & 0 \\ 0 & N_{2,X} P^0 N_{1,X} & 0 & 0 & N_{2,X} P^0 N_{2,X} & 0 \\ 0 & 0 & 0 & 0 & 0 & 0 \end{bmatrix} \begin{Bmatrix} \Delta u_1 \\ \Delta w_1 \\ \Delta \beta_1 \\ \Delta u_2 \\ \Delta w_2 \\ \Delta \beta_2 \end{Bmatrix} dX \quad \text{Eq. 2-55}$$

$$\Delta \Pi_{\text{int}}^{NL} = \int_{L^0} N_{NL}^T P^0 N_{NL} \begin{Bmatrix} \Delta u_1 \\ \Delta w_1 \\ \Delta \beta_1 \\ \Delta u_2 \\ \Delta w_2 \\ \Delta \beta_2 \end{Bmatrix} dX \quad \text{Eq. 2-56}$$

$$N_{NL} = \begin{bmatrix} N_{1,X} & 0 & 0 & N_{2,X} & 0 & 0 \\ 0 & N_{1,X} & 0 & 0 & N_{2,X} & 0 \\ 0 & 0 & 0 & 0 & 0 & 0 \end{bmatrix} \quad \text{Eq. 2-57}$$

$$K_T^{NL} = \int_{L^0} \begin{bmatrix} N_{1,X} P^0 N_{1,X} & 0 & 0 & N_{1,X} P^0 N_{2,X} & 0 & 0 \\ 0 & N_{1,X} P^0 N_{1,X} & 0 & 0 & N_{1,X} P^0 N_{2,X} & 0 \\ 0 & 0 & 0 & 0 & 0 & 0 \\ N_{2,X} P^0 N_{1,X} & 0 & 0 & N_{2,X} P^0 N_{2,X} & 0 & 0 \\ 0 & N_{2,X} P^0 N_{1,X} & 0 & 0 & N_{2,X} P^0 N_{2,X} & 0 \\ 0 & 0 & 0 & 0 & 0 & 0 \end{bmatrix} dX \quad \text{Eq. 2-58}$$

Finally, the large deformation equations can then be rewritten. Eq. 2-59 shows the resulting system for one element, and the mass matrix is shown in Eqs. 2-60 and 2-61.

$$\Delta(\delta \Pi_{\text{int}}) = \delta \tilde{\varphi} K_T \Delta \tilde{\varphi} = \delta \tilde{\varphi} (K_T^L + K_T^{NL}) \Delta \tilde{\varphi} \quad \text{Eq. 2-59}$$

$$\Delta \Pi_{\text{int}}^M = \int_{L^0} N^T \begin{bmatrix} \rho^0 A^0 & 0 & 0 \\ 0 & \rho^0 A^0 & 0 \\ 0 & 0 & \rho^0 I^0 \end{bmatrix} \begin{Bmatrix} \Delta \ddot{u} \\ \Delta \ddot{w} \\ \Delta \ddot{\beta} \end{Bmatrix} dX \quad \text{Eq. 2-60}$$

$$= \int_{L^0} N^T \begin{bmatrix} \rho^0 A^0 & 0 & 0 \\ 0 & \rho^0 A^0 & 0 \\ 0 & 0 & \rho^0 I^0 \end{bmatrix} c_M N \Delta \tilde{\varphi} dX = c_M M^0 \Delta \tilde{\varphi}$$

$$M^0 = \int_{L^0} \rho^0 N^T \begin{bmatrix} A^0 & 0 & 0 \\ 0 & A^0 & 0 \\ 0 & 0 & I^0 \end{bmatrix} N dX \quad \text{Eq. 2-61}$$

### 2.2.2 Total Lagrangian for finite rotations (TLfinite)

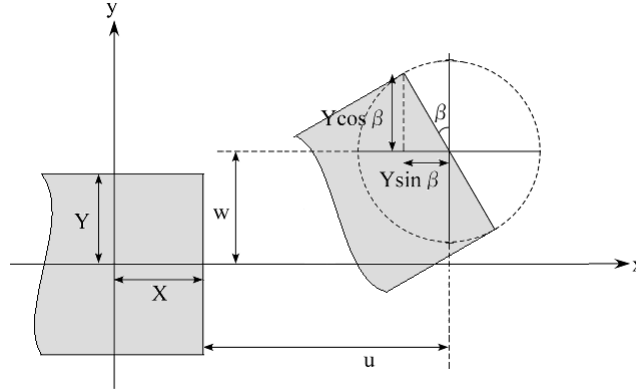


Fig. 2.2 - Schematics for the shape functions utilized in formulation TLfinite.

The basic scheme for this formulation is shown in Fig. 2.2. The steps followed henceforth are very similar to the ones in the previous section, with the difference that the sine and cosine simplifications for small rotations are not adopted. This can be ascertained by Eqs. 2-62 to 2-64.

$$\begin{Bmatrix} x \\ y \\ z \end{Bmatrix} = \begin{Bmatrix} X \\ 0 \\ 0 \end{Bmatrix} + \begin{Bmatrix} u \\ w \\ 0 \end{Bmatrix} + \Lambda \begin{Bmatrix} 0 \\ Y \\ Z \end{Bmatrix} = \begin{Bmatrix} X + u(X) - Y \sin(\beta(X)) \\ w(X) + Y \cos(\beta(X)) \\ Z \end{Bmatrix} \quad \text{Eq. 2-62}$$

$$\Lambda = \begin{bmatrix} \cos \beta & -\sin \beta & 0 \\ \sin \beta & \cos \beta & 0 \\ 0 & 0 & 1 \end{bmatrix} \quad \text{Eq. 2-63}$$

$$\begin{Bmatrix} x \\ y \\ z \end{Bmatrix} = \begin{Bmatrix} X + u - Y \sin \beta \\ w + Y \cos \beta \\ Z \end{Bmatrix} \quad \text{Eq. 2-64}$$

Then, the deformation gradient and the Green-Lagrange strain tensor can be calculated as shown in Eqs. 2-65 through 2-67.

$$F(X, t) = \frac{\partial \chi(X, t)}{\partial X} = \nabla_X \chi(X, t) \Rightarrow F = \begin{bmatrix} 1 + u_{,x} - Y \cos(\beta) \beta_{,x} & -\sin \beta & 0 \\ w_{,x} - Y \sin(\beta) \beta_{,x} & \cos \beta & 0 \\ 0 & 0 & 1 \end{bmatrix} \quad \text{Eq. 2-65}$$

$$E = \frac{1}{2} (F^T F - I) = \begin{bmatrix} E_{XX} & E_{XY} & 0 \\ E_{XY} & 0 & 0 \\ 0 & 0 & 0 \end{bmatrix} \quad \text{Eq. 2-66}$$



$$E_{xx} = u_{,x} + \frac{1}{2}(u_{,x}^2 + w_{,x}^2) - Y[(1 + u_{,x})\cos\beta + w_{,x}\sin\beta]\beta_{,x} + \underline{Y^2\beta_{,x}^2} = E_f^0 - YK_f^0$$

Eq. 2-67

$$2E_{xy} = w_{,x}\cos\beta - (1 + u_{,x})\sin\beta = \Gamma_f^0$$

The term  $Y^2\beta_{,x}^2$  must be ignored, otherwise the following steps cannot be executed. This is not exactly unwarranted, since the partial derivative of the angular deformation is already relatively small, let alone its square. This might bring about less accurate results nevertheless.

The second Piola-Kirchoff stress tensor is then calculated, as is the usual form of forces: normal, shear and bending moment. Also, note that the moment of inertia can be deduced by the same means as before. These results are shown in Eqs. 2-68 through 2-73.

$$S_{xx} = EE_{xx} = E(E^0 - YK^0)$$

$$S_{xy} = 2GE_{xy} = G\Gamma^0$$

Eq. 2-68

$$P^0 = \int_{A^0} S_{xx} dA^0 = \int_{A^0} E(E^0 - YK^0) dA^0 = EA^0E^0 - EK^0 \int_{A^0} Y dA^0$$

Eq. 2-69

$$S^0 = \int_{A^0} S_{xy} dA^0 = \int_{A^0} G\Gamma^0 dA^0 = \kappa GA^0\Gamma^0$$

Eq. 2-70

$$M^0 = - \int_{A^0} S_{xx} Y dA^0 = - \int_{A^0} E(E^0 - YK^0) Y dA^0 = -EE^0 \int_{A^0} Y dA^0 + EK^0 \int_{A^0} Y^2 dA^0$$

Eq. 2-71

$$P^0 = EA^0E^0$$

$$M^0 = EI^0K^0$$

Eq. 2-72

$$I^0 = \int_{A^0} Y^2 dA^0$$

Eq. 2-73

Now, as for the movement equations, they are unchanged from the previous formulation. The same can be said for the virtual work principle, as seen in Eqs. 2-74 through 2-81.

$$\frac{\partial P^0}{\partial X} + q_x = \rho^0 A^0 \ddot{u}$$

Eq. 2-74

$$\frac{\partial S^0}{\partial X} + q_y = \rho^0 A^0 \ddot{w}$$

Eq. 2-75

$$\frac{\partial M^0}{\partial X} + S^0 + m_z = \rho^0 I^0 \ddot{\beta}$$

Eq. 2-76

$$\delta\Pi(u, w, \beta) = \delta W + \delta W_M - \delta\Pi_{ext}$$

Eq. 2-77

$$\delta W = \int_{\Omega_0} S : \delta E dV$$

Eq. 2-78

$$\delta W_M = \int_{L_0} \left[ \delta u (\rho^0 A^0 \ddot{u} - q_X) + \delta w (\rho^0 A^0 \ddot{w} - q_Y) + \delta \beta (\rho^0 I^0 \ddot{\beta} - m_Z) \right] dX \quad \text{Eq. 2-79}$$

$$\delta \Pi_{ext} = (\delta u \bar{P}) \Big|_{\partial P^0} + (\delta \beta \bar{M}) \Big|_{\partial M^0} + (\delta w \bar{S}) \Big|_{\partial S^0} \quad \text{Eq. 2-80}$$

$$\begin{aligned} \delta \Pi(u, w, \beta) = & \int_{\Omega_0} S : \delta E dV + \\ & + \int_{L_0} \left[ \delta u (\rho^0 A^0 \ddot{u} - q_X) + \delta w (\rho^0 A^0 \ddot{w} - q_Y) + \delta \beta (\rho^0 I^0 \ddot{\beta} - m_Z) \right] dX \\ & - (\delta u \bar{P}) \Big|_{\partial P^0} - (\delta \beta \bar{M}) \Big|_{\partial M^0} - (\delta w \bar{S}) \Big|_{\partial S^0} \end{aligned} \quad \text{Eq. 2-81}$$

Most importantly, the internal work can then be calculated based on our three custom strain-stresses, which are quite different from the ones in the previous formulation. In the following equations, the prefix "f" indicates the value of the quantity for the finite rotation (TLfinite) formulation. This is shown in Eqs. 2-82 through 2-85.

$$\delta W = \int_{L^0} (\delta E_f^0 P_f^0 + \delta K_f^0 M^0 + \delta \Gamma_f^0 S^0) dX \quad \text{Eq. 2-82}$$

$$\delta E_f^0 = (1 + u_{,X}) \delta u_{,X} + w_{,X} \delta w_{,X} \quad \text{Eq. 2-83}$$

$$\begin{aligned} \delta K_f^0 = & \beta_{,X} \cos \beta \delta u_{,X} + \beta_{,X} \sin \beta \delta w_{,X} + \\ & + \beta_{,X} \left[ (1 + u_{,X}) (-\sin \beta) + w_{,X} \cos \beta \right] \delta \beta + \left[ (1 + u_{,X}) \cos \beta + w_{,X} \sin \beta \right] \delta \beta_{,X} \end{aligned} \quad \text{Eq. 2-84}$$

$$\delta \Gamma_f^0 = (-\sin \beta) \delta u_{,X} + \cos \beta \delta w_{,X} - \left[ (1 + u_{,X}) \cos \beta + w_{,X} \sin \beta \right] \delta \beta \quad \text{Eq. 2-85}$$

In order to simplify the visualization of these terms, the shorthand variables shown in Eqs. 2-86 and 2-87.

$$\nu_f = (1 + u_{,X}) (-\sin \beta) + w_{,X} \cos \beta \quad \text{Eq. 2-86}$$

$$\pi_f = (1 + u_{,X}) \cos \beta + w_{,X} \sin \beta \quad \text{Eq. 2-87}$$

The simplified equations are shown in Eqs. 2-88 through 2-90.

$$\delta E_f^0 = (1 + u_{,X}) \delta u_{,X} + w_{,X} \delta w_{,X} \quad \text{Eq. 2-88}$$

$$\delta K_f^0 = \beta_{,X} \cos \beta \delta u_{,X} + \beta_{,X} \sin \beta \delta w_{,X} + \beta_{,X} \nu_f \delta \beta + \pi_f \delta \beta_{,X} \quad \text{Eq. 2-89}$$

$$\delta \Gamma_f^0 = (-\sin \beta) \delta u_{,X} + \cos \beta \delta w_{,X} - \pi_f \delta \beta \quad \text{Eq. 2-90}$$

Now, the first step in the discretization step is also exactly the same as in the TLsmall formulation, as shown in Eqs. 2-91 through 2-96. The main difference between TLsmall and TLfinite formulations lies in the expressions shown in Eqs. 2-97 to 2-99. Finally, Eqs. 2-100 to 2-106 display the discretized form of the

virtual work principle applied to this element.

$$u = N_u \tilde{u}, \quad w = N_w \tilde{w}, \quad \beta = N_\beta \tilde{\beta} \quad \text{Eq. 2-91}$$

$$N_u = N_w = N_\beta = [N_1 \quad N_2] \quad \text{Eq. 2-92}$$

$$\tilde{u} = \begin{bmatrix} u_1 \\ u_2 \end{bmatrix}, \quad \tilde{w} = \begin{bmatrix} w_1 \\ w_2 \end{bmatrix}, \quad \tilde{\beta} = \begin{bmatrix} \beta_1 \\ \beta_2 \end{bmatrix} \quad \text{Eq. 2-93}$$

$$N_1 = \frac{x_2 - x}{L^0}, \quad N_2 = \frac{x - x_1}{L^0} \quad \text{Eq. 2-94}$$

$$\varphi = N \tilde{\varphi}$$

$$\varphi = [u \quad w \quad \beta] \quad \text{Eq. 2-95}$$

$$\tilde{\varphi} = [u_1 \quad w_1 \quad \beta_1 \quad u_2 \quad w_2 \quad \beta_2]$$

$$N = \begin{bmatrix} N_1 & 0 & 0 & N_2 & 0 & 0 \\ 0 & N_1 & 0 & 0 & N_2 & 0 \\ 0 & 0 & N_1 & 0 & 0 & N_2 \end{bmatrix} \quad \text{Eq. 2-96}$$

$$\delta E_f^0 = (1 + u_{,X}) \delta u_{,X} + w_{,X} \delta w_{,X} \quad \text{Eq. 2-97}$$

$$\delta K_f^0 = \beta_{,X} \cos \beta \delta u_{,X} + \beta_{,X} \sin \beta \delta w_{,X} + \beta_{,X} v_f \delta \beta + \pi_f \delta \beta_{,X} \quad \text{Eq. 2-98}$$

$$\delta \Gamma_f^0 = (-\sin \beta) \delta u_{,X} + \cos \beta \delta w_{,X} - \pi_f \delta \beta \quad \text{Eq. 2-99}$$

$$\varepsilon_f^0 = \begin{Bmatrix} \delta E_f^0 \\ \delta K_f^0 \\ \delta \Gamma_f^0 \end{Bmatrix} = B_f \begin{bmatrix} u_1 \\ w_1 \\ \beta_1 \\ u_2 \\ w_2 \\ \beta_2 \end{bmatrix} = B_f \tilde{\varphi} \quad \text{Eq. 2-100}$$

$$B_f = [B_{f,1} \quad B_{f,2}] \quad \text{Eq. 2-101}$$

$$B_{f,i} = \begin{bmatrix} (1 + u_{,X}) N_{i,X} & w_{,X} N_{i,X} & 0 \\ \beta_{,X} \cos \beta N_{i,X} & \beta_{,X} \sin \beta N_{i,X} & \beta_{,X} v_f N_i + \pi_f N_{i,X} \\ (-\sin \beta) N_{i,X} & \cos \beta N_{i,X} & -\pi_f N_i \end{bmatrix} \quad \text{Eq. 2-102}$$

$$\delta\Pi_{\text{int}} = \delta W + \delta W_M = \int_{L^0} \begin{bmatrix} \delta E^0 & \delta K^0 & \delta I^0 \end{bmatrix} \begin{bmatrix} P^0 \\ M^0 \\ S^0 \end{bmatrix} dX + \int_{L^0} (N\delta\tilde{\varphi})^T \begin{Bmatrix} \rho^0 A^0 \ddot{u} - q_X \\ \rho^0 A^0 \ddot{w} - q_Y \\ \rho^0 I^0 \ddot{\beta} - m_Z \end{Bmatrix} dX \quad \text{Eq. 2-103}$$

$$\delta\Pi_{\text{int}} = \delta\tilde{\varphi}^T \int_{L^0} B^T \begin{Bmatrix} P^0 \\ M^0 \\ S^0 \end{Bmatrix} + N^T \begin{Bmatrix} \rho^0 A^0 \ddot{u} - q_X \\ \rho^0 A^0 \ddot{w} - q_Y \\ \rho^0 I^0 \ddot{\beta} - m_Z \end{Bmatrix} dX = \delta\tilde{\varphi} \left[ \hat{W}^0 + \hat{M}^0 \ddot{\tilde{\varphi}} - \hat{f}^0 \right] \quad \text{Eq. 2-104}$$

$$\hat{f}^0 = \int_{L^0} N^T \begin{Bmatrix} q_X \\ q_Y \\ m_Z \end{Bmatrix} dX \quad \text{Eq. 2-105}$$

$$\hat{M}^0 = \int_{L^0} \rho^0 N^T \begin{bmatrix} A^0 & 0 & 0 \\ 0 & A^0 & 0 \\ 0 & 0 & I^0 \end{bmatrix} N dX \quad \text{Eq. 2-106}$$

In the next step, the variation of the virtual work stationary (Eq. 2-107) is then calculated, so that its linear (Eq. 2-108 to 2-110) and nonlinear (Eq. 2-111 to 2-121) terms can be obtained separately.

$$\begin{aligned} \Delta(\delta\Pi_{\text{int}}) &= \delta\tilde{\varphi}^T \int_{L^0} \Delta B_f^T \begin{Bmatrix} P^0 \\ M^0 \\ S^0 \end{Bmatrix} + B_f^T \begin{Bmatrix} \Delta P^0 \\ \Delta M^0 \\ \Delta S^0 \end{Bmatrix} + N^T \begin{Bmatrix} \rho^0 A^0 \Delta \ddot{u} \\ \rho^0 A^0 \Delta \ddot{w} \\ \rho^0 I^0 \Delta \ddot{\beta} \end{Bmatrix} dX = \\ &= \delta\tilde{\varphi} \left[ \Delta\Pi_{\text{int}}^{NL} + \Delta\Pi_{\text{int}}^L + \Delta\Pi_{\text{int}}^M \right] \end{aligned} \quad \text{Eq. 2-107}$$

$$\Delta\Pi_{\text{int}}^L = \int_{L^0} B_f^T \begin{Bmatrix} \Delta P^0 \\ \Delta M^0 \\ \Delta S^0 \end{Bmatrix} dX = \int_{L^0} B_f^T \begin{bmatrix} EA^0 & 0 & 0 \\ 0 & EI^0 & 0 \\ 0 & 0 & \kappa GA^0 \end{bmatrix} \begin{Bmatrix} \Delta E^0 \\ \Delta K^0 \\ \Delta \Gamma^0 \end{Bmatrix} dX \quad \text{Eq. 2-108}$$

$$\Delta\Pi_{\text{int}}^L = \int_{L^0} B_f^T D B_f \Delta\tilde{\varphi} dX \quad \text{where } D = \begin{bmatrix} EA^0 & 0 & 0 \\ 0 & EI^0 & 0 \\ 0 & 0 & \kappa GA^0 \end{bmatrix} \quad \text{Eq. 2-109}$$

$$K_T^L = \int_{L^0} B_f^T D B_f dX \quad \text{Eq. 2-110}$$

To account for geometrical non-linearity, the nonlinear tangent stiffness must be obtained.

$$\Delta B_f = \begin{bmatrix} \Delta u_{,X} N_{u,X} & \Delta w_{,X} N_{w,X} & 0 \\ (\Delta\beta_{,X} \cos \beta - \beta_{,X} \sin \beta \Delta\beta) N_{u,X} & (\Delta\beta_{,X} \sin \beta + \beta_{,X} \cos \beta \Delta\beta) N_{w,X} & \Delta\eta_f^* \\ (-\cos \beta) \Delta\beta N_{u,X} & (-\sin \beta) \Delta\beta N_{w,X} & -\Delta\pi_f N_\beta \end{bmatrix} \quad \text{Eq. 2-111}$$

$$\Delta\eta_f^* = \Delta(\beta_{,X}\nu_f N_\beta + \pi_f N_{\beta,X}) = (\Delta\beta_{,X}\nu_f + \beta_{,X}\Delta\nu_f)N_\beta + \Delta\pi_f N_{\beta,X} \quad \text{Eq. 2-112}$$

$$\begin{aligned} \Delta\pi_f &= \Delta u_{,X} \cos \beta + (1 + u_{,X})(-\sin \beta)\Delta\beta + \Delta w_{,X} \sin \beta + w_{,X}(\cos \beta)\Delta\beta \\ &= (\cos \beta)\Delta u_{,X} + (\sin \beta)\Delta w_{,X} + \nu_f \Delta\beta \end{aligned} \quad \text{Eq. 2-113}$$

$$\begin{aligned} \Delta\nu_f &= \Delta u_{,X}(-\sin \beta) + (1 + u_{,X})(-\cos \beta)\Delta\beta + \Delta w_{,X} \cos \beta + w_{,X}(-\sin \beta)\Delta\beta \\ &= (-\sin \beta)\Delta u_{,X} + (\cos \beta)\Delta w_{,X} + \pi_f \Delta\beta \end{aligned} \quad \text{Eq. 2-114}$$

$$\begin{aligned} \Delta\Pi_{\text{int}}^{NL} &= \int_{L^0} \Delta B^T \begin{Bmatrix} P^0 \\ M^0 \\ S^0 \end{Bmatrix} dX \\ &= \int_{L^0} \left\{ \begin{aligned} &\{N_{u,X} P^0\} \Delta u_{,X} + \{(-\beta_{,X} \sin \beta M^0 - \cos \beta S^0) N_{u,X}\} \Delta\beta + \{\cos \beta N_{u,X} M^0\} \Delta\beta_{,X} \\ &\{N_{w,X} P^0\} \Delta w_{,X} + (\Delta\beta_{,X} \sin \beta + \beta_{,X} \cos \beta \Delta\beta) N_{w,X} M^0 + (-\sin \beta) N_{w,X} S^0 \Delta\beta \\ &\Delta\eta_f^* M^0 - \Delta\pi_f N_\beta S^0 \end{aligned} \right\} dX \end{aligned} \quad \text{Eq. 2-115}$$

$$\begin{aligned} \Delta\eta^* M^0 - \Delta\pi_f N_\beta S^0 &= \{\beta_{,X}(-\sin \beta) N_\beta M^0 + \cos \beta N_{\beta,X} M^0 - \cos \beta N_\beta S^0\} \Delta u_{,X} + \\ &+ \{\beta_{,X}(\cos \beta) N_\beta M^0 + \sin \beta N_{\beta,X} M^0 - \sin \beta N_\beta S^0\} \Delta w_{,X} + \\ &+ \{\nu_f N_{\beta,X} M^0 - \beta_{,X} \pi_f N_\beta M^0 - \nu_f N_\beta S^0\} \Delta\beta + \{\nu_f N_\beta M^0\} \Delta\beta_{,X} \end{aligned} \quad \text{Eq. 2-116}$$

$$\Delta\Pi_{\text{int}}^{NL} = \int_{L^0} \begin{bmatrix} N_{u,X} P^0 N_{u,X} & 0 & T_1 \\ 0 & N_{w,X} P^0 N_{w,X} & T_2 \\ T_1 & T_2 & T_3 \end{bmatrix} \begin{Bmatrix} \Delta\tilde{u} \\ \Delta\tilde{w} \\ \Delta\tilde{\beta} \end{Bmatrix} dX = K_T^{NL} \Delta\tilde{\varphi} \quad \text{Eq. 2-117}$$

$$\begin{aligned} T_1 &= \{\cos \beta N_{\beta,X} M^0 + \beta_{,X}(-\sin \beta) N_\beta M^0 - \cos \beta N_\beta S^0\} N_{u,X} \\ &= \cos \beta N_{\beta,X} M^0 N_{u,X} - (\beta_{,X} \sin \beta M^0 + \cos \beta S^0) N_\beta N_{u,X} \end{aligned} \quad \text{Eq. 2-118}$$

$$\begin{aligned} T_2 &= \{(\sin \beta) N_{\beta,X} M^0 + \beta_{,X} \cos \beta N_\beta M^0 - \sin \beta N_\beta S^0\} N_{w,X} \\ &= \sin \beta N_{\beta,X} M^0 N_{w,X} + (\beta_{,X} \cos \beta M^0 - \sin \beta S^0) N_\beta N_{w,X} \end{aligned} \quad \text{Eq. 2-119}$$

$$\begin{aligned} T_3 &= (\nu_f N_{\beta,X} M^0 - \beta_{,X} \pi_f N_\beta M^0 - \nu_f N_\beta S^0) N_\beta + (\nu_f N_\beta M^0) N_{\beta,X} = \\ &= 2\nu_f N_{\beta,X} M^0 N_\beta - (\beta_{,X} \pi_f M^0 + \nu_f S^0) N_\beta N_\beta \end{aligned} \quad \text{Eq. 2-120}$$

$$K_T^{NL} = \int_{L^0} \begin{bmatrix} N_{u,X} P^0 N_{u,X} & 0 & T_1 \\ 0 & N_{w,X} P^0 N_{w,X} & T_2 \\ T_1 & T_2 & T_3 \end{bmatrix} dX \quad \text{Eq. 2-121}$$

To be able to utilize this formulation programmatically in software, we now write the discretized version of it for two nodes (in the implementation it is also possible to use 3 nodes), as shown in Eqs. 2-122 through 2-125.

$$\Delta B = [\Delta B_1 \quad \Delta B_2]$$

$$\Delta B_i = \begin{bmatrix} \Delta u_{,X} N_{i,X} & \Delta w_{,X} N_{i,X} & 0 \\ (\Delta \beta_{,X} \cos \beta - \beta_{,X} \sin \beta \Delta \beta) N_{i,X} & (\Delta \beta_{,X} \sin \beta + \beta_{,X} \cos \beta \Delta \beta) N_{i,X} & \Delta \eta_i^* \\ (-\cos \beta) \Delta \beta N_{i,X} & (-\sin \beta) \Delta \beta N_{i,X} & -\Delta \pi_f N_i \end{bmatrix} \quad \text{Eq. 2-122}$$

$$\Delta \eta_i^* = (\Delta \beta_{,X} v_f + \beta_{,X} \Delta v_f) N_i + \Delta \pi_f N_{i,X} \quad \text{Eq. 2-123}$$

$$\Delta \pi_f = (\cos \beta) \Delta u_{,X} + (\sin \beta) \Delta w_{,X} + v_f \Delta \beta \quad \text{Eq. 2-124}$$

$$\Delta v_f = (-\sin \beta) \Delta u_{,X} + (\cos \beta) \Delta w_{,X} - \pi_f \Delta \beta \quad \text{Eq. 2-125}$$

It is then necessary to multiply the stress matrix into the variation of the transpose of the strain-displacement matrix, as shown in Eq. 2-115. This can be done with the utilization of Eqs. 2-122 to 2-125. The result of this operation is shown in Eq. 2-126.

$$\Delta \Pi_{\text{int}}^{NL} = \int_{L^0} \begin{bmatrix} \Delta u_{,X} N_{1,X} P^0 + (\Delta \beta_{,X} \cos \beta - \beta_{,X} \sin \beta \Delta \beta) N_{1,X} M^0 + (-\cos \beta) \Delta \beta N_{1,X} S^0 \\ \Delta w_{,X} N_{1,X} P^0 + (\Delta \beta_{,X} \sin \beta + \beta_{,X} \cos \beta \Delta \beta) N_{1,X} M^0 + (-\sin \beta) \Delta \beta N_{1,X} S^0 \\ \Delta \eta_1^* M^0 - \Delta \pi_f N_1 S^0 \\ \Delta u_{,X} N_{2,X} P^0 + (\Delta \beta_{,X} \cos \beta - \beta_{,X} \sin \beta \Delta \beta) N_{2,X} M^0 + (-\cos \beta) \Delta \beta N_{2,X} S^0 \\ \Delta w_{,X} N_{2,X} P^0 + (\Delta \beta_{,X} \sin \beta + \beta_{,X} \cos \beta \Delta \beta) N_{2,X} M^0 + (-\sin \beta) \Delta \beta N_{2,X} S^0 \\ \Delta \eta_2^* M^0 - \Delta \pi_f N_2 S^0 \end{bmatrix} dX \quad \text{Eq. 2-126}$$

Now, the variation of displacements must be separated term by term in each line. The first line is operated upon in Eq. 2-127.

$$\begin{aligned} & \Delta u_{,X} N_{i,X} P^0 + (\Delta \beta_{,X} \cos \beta - \beta_{,X} \sin \beta \Delta \beta) N_{i,X} M^0 + (-\cos \beta) \Delta \beta N_{i,X} S^0 = \\ & = \{N_{i,X} P^0 N_{j,X}\} \Delta u_j + \{\cos \beta N_{i,X} M^0 N_{j,X} - \beta_{,X} \sin \beta N_j M^0 N_{i,X} + (-\cos \beta) N_j S^0 N_{i,X}\} \Delta \beta_j = \\ & = \{N_{i,X} P^0 N_{j,X}\} \Delta u_j + \{T_{1,ij}\} \Delta \beta_j \\ & T_{1,ij} = \cos \beta N_{i,X} M^0 N_{j,X} - (\beta_{,X} \sin \beta M^0 + \cos \beta S^0) N_j N_{i,X} \end{aligned} \quad \text{Eq. 2-127}$$

The second line is operated on in Eq. 2-128.

$$\begin{aligned} & \Delta w_{,X} N_{i,X} P^0 + (\Delta \beta_{,X} \cos \beta + \beta_{,X} \cos \beta \Delta \beta) N_{i,X} M^0 + (-\sin \beta) \Delta \beta N_{i,X} S^0 = \\ & = \{N_{i,X} P^0 N_{j,X}\} \Delta w_j + \{\sin \beta N_{j,X} M^0 N_{i,X} + \beta_{,X} \cos \beta N_j M^0 N_{i,X} + (-\sin \beta) N_j S^0 N_{i,X}\} \Delta \beta_j = \\ & = \{N_{i,X} P^0 N_{j,X}\} \Delta w_j + \{T_{2,ij}\} \Delta \beta_j \end{aligned}$$

$$T_{2,ij} = \sin \beta N_{j,X} M^0 N_{i,X} + (\beta_{,X} \cos \beta M^0 - \sin \beta S^0) N_j N_{i,X} \quad \text{Eq. 2-128}$$

Finally, the third line is operated on in Eqs. 2-129 and 2-130.

$$\begin{aligned} \Delta \eta_i^* M^0 - \Delta \pi_f N_i S^0 &= \left[ \cos \beta N_{i,X} M^0 N_{j,X} - (\beta_{,X} \sin \beta M^0 + \cos \beta S^0) N_i N_{j,X} \right] \Delta u_j + \\ &+ \left[ \sin \beta N_{i,X} M^0 N_{j,X} + (\beta_{,X} \cos \beta M^0 - \sin \beta S^0) N_i N_{j,X} \right] \Delta w_j + \\ &+ \left[ \nu_f N_{i,X} M^0 N_j + \nu_f N_i M^0 N_{j,X} - (\beta_{,X} \pi_f M^0 + \nu_f S^0) N_i N_j \right] \Delta \beta_j \end{aligned}$$

$$\Delta \eta_i^* M^0 - \Delta \pi_f N_i S^0 = T_{1,ji} \Delta u_j + T_{2,ji} \Delta w_j + T_{3,ji} \Delta \beta_j \quad \text{Eq. 2-129}$$

$$T_{3,ij} = \nu_f N_{i,X} M^0 N_j + \nu_f N_i M^0 N_{j,X} - (\beta_{,X} \pi_f M^0 + \nu_f S^0) N_i N_j \quad \text{Eq. 2-130}$$

Note also that  $T_{1,ij} \neq T_{1,ji}$  and  $T_{2,ij} \neq T_{2,ji}$ , but  $T_{3,ij} = T_{3,ji}$ . This is very significant from the standpoint of

theory, since even for a simple element such as 2D beam element has an *unsymmetric* stiffness matrix when taking large displacements into consideration. Then, back to the *unsymmetric* nonlinear term for the virtual work, its full form is shown in Eq. 2-131. Eq. 2-132 shows how to compute the element tangent stiffness matrix at each step, and Eqs. 2-133 and 2-134 show the dynamic term as wells as the consistent mass matrix.

$$\Delta \Pi_{\text{int}}^{NL} = \int_{L^0} \begin{bmatrix} N_{1,X} P^0 N_{1,X} & 0 & T_{1,11} & N_{1,X} P^0 N_{2,X} & 0 & T_{1,12} \\ 0 & N_{1,X} P^0 N_{1,X} & T_{2,11} & 0 & N_{1,X} P^0 N_{2,X} & T_{2,12} \\ T_{1,11} & T_{2,11} & T_{3,11} & T_{1,12} & T_{2,12} & T_{3,12} \\ N_{2,X} P^0 N_{1,X} & 0 & T_{1,21} & N_{2,X} P^0 N_{2,X} & 0 & T_{1,22} \\ 0 & N_{2,X} P^0 N_{1,X} & T_{2,21} & 0 & N_{2,X} P^0 N_{2,X} & T_{2,22} \\ T_{1,21} & T_{2,21} & T_{3,21} & T_{1,22} & T_{2,22} & T_{3,22} \end{bmatrix} \begin{Bmatrix} \Delta u_1 \\ \Delta w_1 \\ \Delta \beta_1 \\ \Delta u_2 \\ \Delta w_2 \\ \Delta \beta_2 \end{Bmatrix} dX \Delta \tilde{\varphi} \quad \text{Eq. 2-131}$$

$$\Delta(\delta \Pi_{\text{int}}) = \delta \tilde{\varphi} K_T \Delta \tilde{\varphi} = \delta \tilde{\varphi} (K_T^L + K_T^{NL}) \Delta \tilde{\varphi} \quad \text{Eq. 2-132}$$

$$\Delta \Pi_{\text{int}}^M = \int_{L^0} N^T \begin{bmatrix} \rho^0 A^0 & 0 & 0 \\ 0 & \rho^0 A^0 & 0 \\ 0 & 0 & \rho^0 I^0 \end{bmatrix} \begin{Bmatrix} \Delta \ddot{u} \\ \Delta \ddot{w} \\ \Delta \ddot{\beta} \end{Bmatrix} dX \quad \text{Eq. 2-133}$$

$$= \int_{L^0} N^T \begin{bmatrix} \rho^0 A^0 & 0 & 0 \\ 0 & \rho^0 A^0 & 0 \\ 0 & 0 & \rho^0 I^0 \end{bmatrix} c_M N \Delta \tilde{\varphi} dX = c_M M^0 \Delta \tilde{\varphi}$$

$$M^0 = \int_{L^0} \rho^0 N^T \begin{bmatrix} A^0 & 0 & 0 \\ 0 & A^0 & 0 \\ 0 & 0 & I^0 \end{bmatrix} N dX \quad \text{Eq. 2-134}$$

### 2.2.3 Brief comment on formulations

A very important point to be made about infinitesimal formulations is that those elements do not use tangent stiffness matrices. For all ends and purposes, they are considered not to dislocate considerably from their initial position, and therefore it makes sense that their stiffness matrix is computed only once, in the beginning of the simulation. This fact implies that these elements will be fundamentally more stable and fast, compared to the proposed elements.

Another essential difference between the proposed formulations and existing infinitesimal formulations is in how these formulations deal with the three custom strain-stress pairs. This is so because infinitesimal formulations can afford to ignore the interplay of these quantities. One such example is that a beam element that was initially loaded with a normal force might have this normal force play the partially role of shear force. The proposed elements are expected to deal with these complications.

Finally, future works may expand on the proposed formulations, but another tangent line of research that may be followed is formulating a beam through the Updated Lagrangian (UL) method. This formulation presents complications which do not appear in the Total Lagrangian (TL) formulation. The formulation and implementation of a UL beam is outside the scope of the present work.

## 2.3 Afterword on Implementation Issues

From the point of view of a computer scientist, a higher-level object-oriented approach to finite element programming might be desirable. The key concept here is that simplicity of implementation provides for ease in any changes in code. The implementation of such an approach is, however, clearly out of the scope of the present work.



### 3 Validation

In order to assess the two proposed formulations - TLsmall and TLfinite<sup>1</sup> -, a plethora of comparative analysis was performed using the various types of available beams. The two main purposes of this section are: (1) to make sure that the beams were implemented correctly, and that they work well within the context of numerical simulation software; and (2) to obtain insight into how large displacement formulations affect element behavior, and what are boundaries of the domain within which these formulations are applicable.

This was done by means of two main batches of analyses that are henceforth referred to as "moment analysis" and "shear analysis". The moment analysis batch contains cantilever beams subjected to a punctual bending moment in their free extremity, whereas the shear analysis batch contains cantilever beams subjected to a punctual shear force in their extremity. Results for these batch of analysis are comprised of data visualization displacements, strains, stresses and position. Specific details for these analysis can be found in section 3.1, where the inner workings of meshes, element formulations, loading modes, position and material properties are thoroughly explained. Also, a clamped-hinged arch analysis was performed.

Sections 3.2 and 3.3 go over the analysis results, and offer some understanding on the results at hand. Section 3.4 is a double-clamped arch which can be compared with bibliographical references. Finally, section 3.5 summarizes the results shown in this chapter in the form of tentative conclusions.

#### 3.1 Overview of validation methodology

##### 3.1.1 Mesh Types

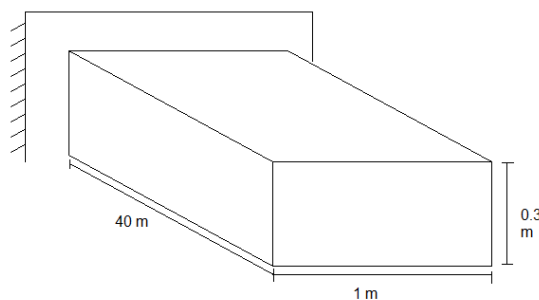


Fig. 3.1 - Geometry of cantilever beam used for moment and shear analyses.

For both moment and shear analyses, there were two types of meshes that were used. The geometry of the arbitrary beam chosen for simulation purposes is shown in Fig. 3.1. Two meshes were used: the first is a mesh comprised solely of linear elements, as seen in Fig. 3.2; and the second is comprised of plane elements,

---

<sup>1</sup> TLsmall stands for Total Lagrangian for small rotations and TLfinite stands for Total Lagrangian for finite rotations. For more details, please refer to Chapter 2.

as seen in Fig. 3.3. The characteristics of the plane elements chosen for comparison will affect the results, and its effects are explored further along. Note, however, that the elements are shaped either in the shape of a line or in the shape of a four-sided polygon. Also, the linearity discussed here is unrelated to the formulation assigned to these elements.

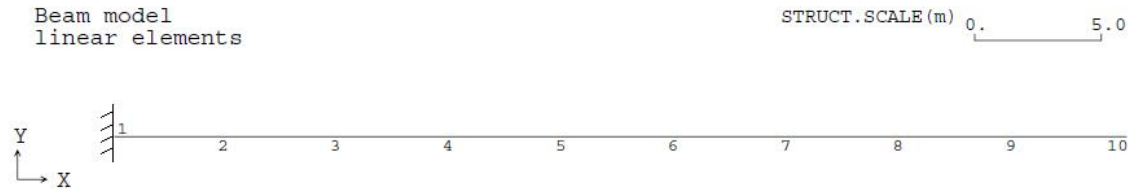


Fig. 3.2 - Mesh composed of linear elements.

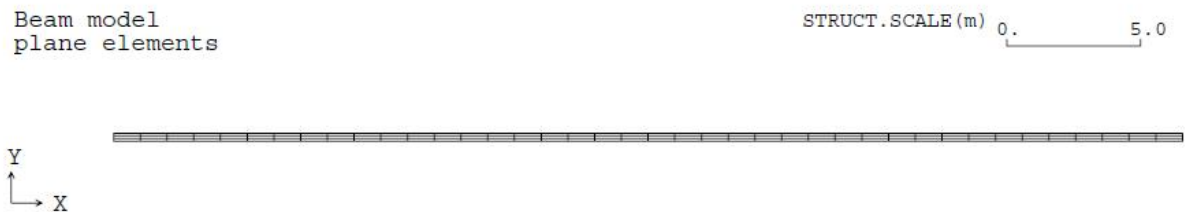


Fig. 3.3 - Mesh composed of four-sided plane elements.

Also, note that analyses that were run using meshes composed of four-sided elements (referred to as plane elements henceforth) do not output their rotation. However, this issue can be easily circumvented. In this case, the x- and y-oriented displacements shown in the results of the following analyses was approximated to the nodal point closest to the center of the tip. The chosen node was node 82, as shown in Fig. 3.4. The beta-rotation presented in the results below was calculated as shown on Fig. 3.5, using the formula from Eq. 3-1.

$$\beta = \tan^{-1} \frac{\Delta u}{\Delta w + L} = \tan^{-1} \frac{u_{123} - u_{82}}{w_{123} - w_{82} + L} \quad \text{Eq. 3-1}$$

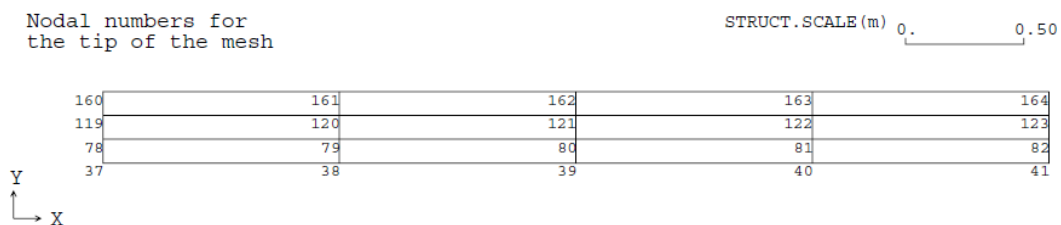


Fig. 3.4 - Detail of the tip of mesh for the numerical simulation of the beam with the use of plane elements.

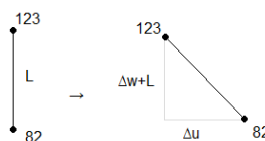


Fig. 3.5 - Calculation of the tip beta-rotation for mesh analyses.

### 3.1.2 Element Formulation Types

For each mesh type shown in section 3.1.1, a number of formulations can be used. The linear mesh can be assigned linear infinitesimal Euler elements (infinitesimal), isoparametric infinitesimal elements (isoparametric), Total Lagrangian for small rotations (TLsmall) or Total Lagrangian for finite rotations (TLfinite). The plane elements used in conjunction with the mesh shown in Fig. 3.3 can also have a number of associated formulations, such as infinitesimal isoparametric (isoparametric), Total Lagrangian (TL) or Updated Lagrangian (UL).

### 3.1.3 Loading Modes

The loading modes used in the moment and shear analyses are quite simple, and depend on the mesh type that's being used in a particular analysis. In the case of moment analysis, a punctual bending moment is applied to the beam extremity (Fig. 3.6) in the case of linear elements, whereas two forces are used in the case of plane elements (Fig. 3.7). For the shear analysis, a punctual shear force is applied to the beam extremity in the case of linear elements (Fig. 3.8), whereas one fourth of the punctual shear force is applied to each of the nodes (Fig. 3.9).

Also, these forces cannot be applied instantly, because that would invariably lead to numerical instabilities. Throughout these analyses, the most used alternative was to linearly apply the load with time, thus leading to comparable results even between very distinct analyses.

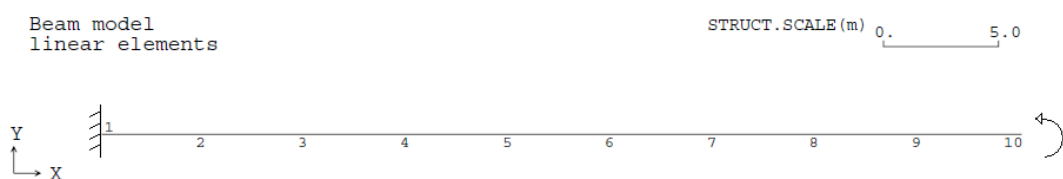


Fig. 3.6 - Loading conditions for meshes of linear elements in moment analyses.

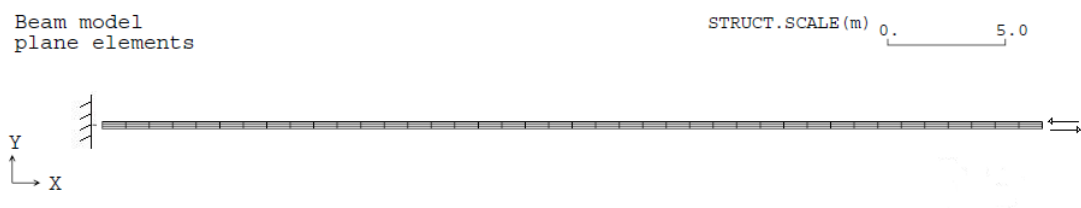


Fig. 3.7 - Loading conditions for meshes of plane elements in moment analyses.

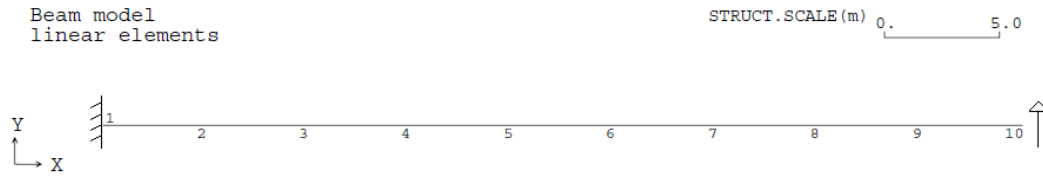


Fig. 3.8 - Loading conditions for meshes of linear elements in shear analyses.

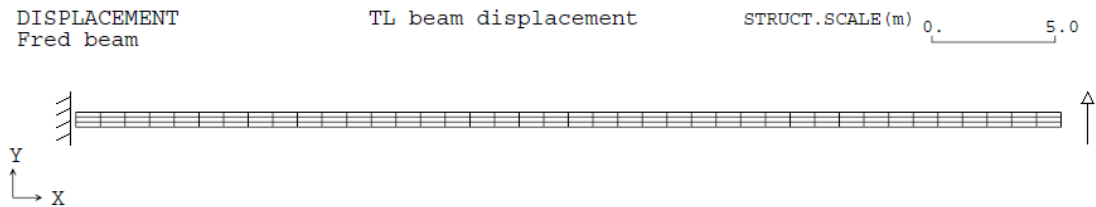


Fig. 3.9 - Loading conditions for meshes of plane elements in shear analyses.

For the moment analyses, the maximum moment  $M = 9.0 \times 10^6 \text{ Nm}$  was applied linearly over the course of ten seconds. For the shear analyses, the maximum force of  $S = 3.0 \times 10^7 \text{ N}$  was also applied linearly over ten seconds. This timeframe was chosen because it is neither too big nor too small, and the dynamic effects are several orders of magnitude smaller than the static displacements, strains and stresses. Varying this timeframe did not affect the results.

#### 3.1.4 Position

This chapter is dedicated to obtaining insight and assessing the usability of the proposed beam formulations, so this particular section of each analysis was dedicated to rotating them around. This was done by hand-picking slope values for the beam models, and then performing the moment and shear analysis on each model. The coordinates and slopes for each of the models are shown in Tab. 3.1, and a couple of these meshes is shown in Fig. 3.10.

Tab. 3.1 - Different positions for models submitted to analysis.

Model Number	X1 (m)	Y1 (m)	X2 (m)	Y2 (m)	Slope (degrees)	Length (m)
P1	10.0	10.0	50.0	10.0	0.0	40.0
P2	10.0	10.0	42.0	34.0	36.9	40.0
P3	10.0	10.0	10.0	50.0	90.0	40.0
P4	10.0	10.0	-14.0	42.0	126.9	40.0
P5	10.0	10.0	-30.0	10.0	180.0	40.0
P6	10.0	10.0	-14.0	-22.0	233.1	40.0
P7	10.0	10.0	10.0	-30.0	270.0	40.0
P8	10.0	10.0	34.0	-22.0	306.9	40.0

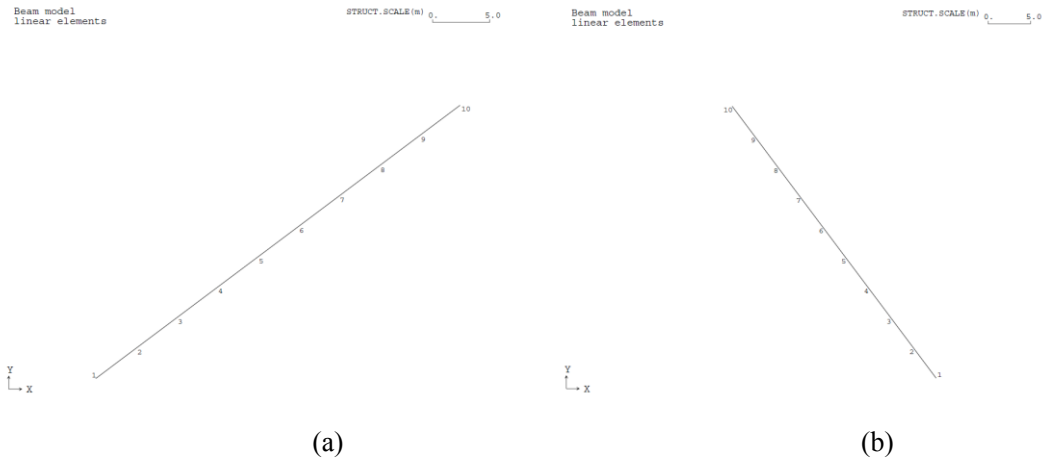


Fig. 3.10 - (a) Model for analysis P2 and (b) model for analysis P4.

### 3.1.5 Material Properties

For all of the analyses presented in this chapter, the material properties were chosen arbitrarily to represent a generic beam. These properties are shown in Tab. 3.2.

Tab. 3.2 - Geometric and material properties chosen for Moment and Shear analyses.

Property	Value
E (GPa)	2.09
$\nu$	0.3
G (MPa)	800
A (m <sup>2</sup> )	0.3
I (10 <sup>-4</sup> m <sup>4</sup> )	22.5

## 3.2 Moment analysis

### 3.2.1 Displacements

The moment analysis was executed as described, and its results in the displacement domain are presented in this section. An example of the final deformed configuration is shown in Fig. 3.11. And a thorough comparison of results is shown in Figs. 3.12 to 3.15. The observed differences in results cannot be assigned exclusively to the different formulations, due to the fact that loading conditions and mesh size were considered as given values for this analysis.

As expected, the results show that infinitesimal, linear formulations tend to return values for the displacements in the axial direction of the beam that are too small, and values that are too big in the transverse direction. It's also interesting to note how the tip beta-rotation of models based on meshes of plane elements behaves differently, especially for lower values of applied moment. This might be due to how the moment load was applied in this particular analysis, and how the beta-displacement was calculated.

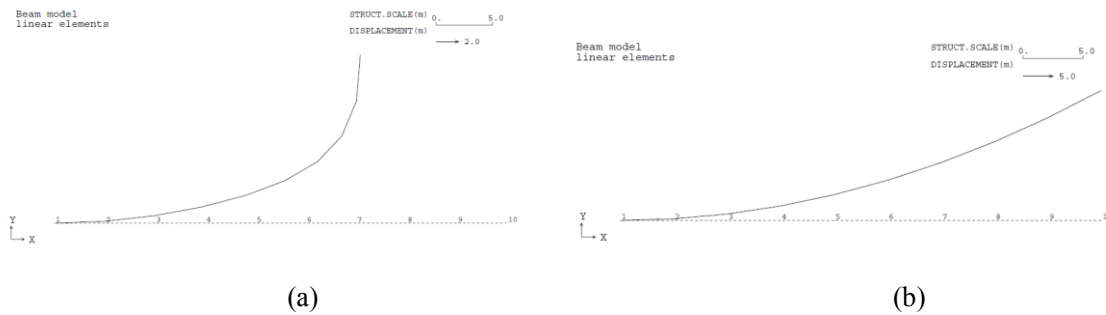


Fig. 3.11 - Deformed configuration of (a) Total Lagrangian beam for finite rotation and (b) infinitesimal isoparametric formulations.

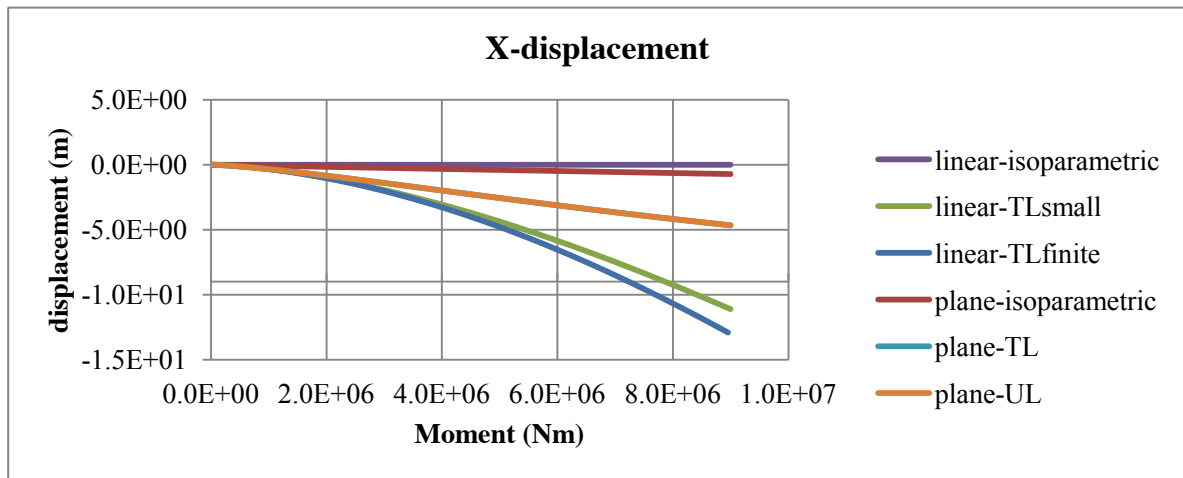


Fig. 3.12 - Comparison of x-displacements for moment analysis.

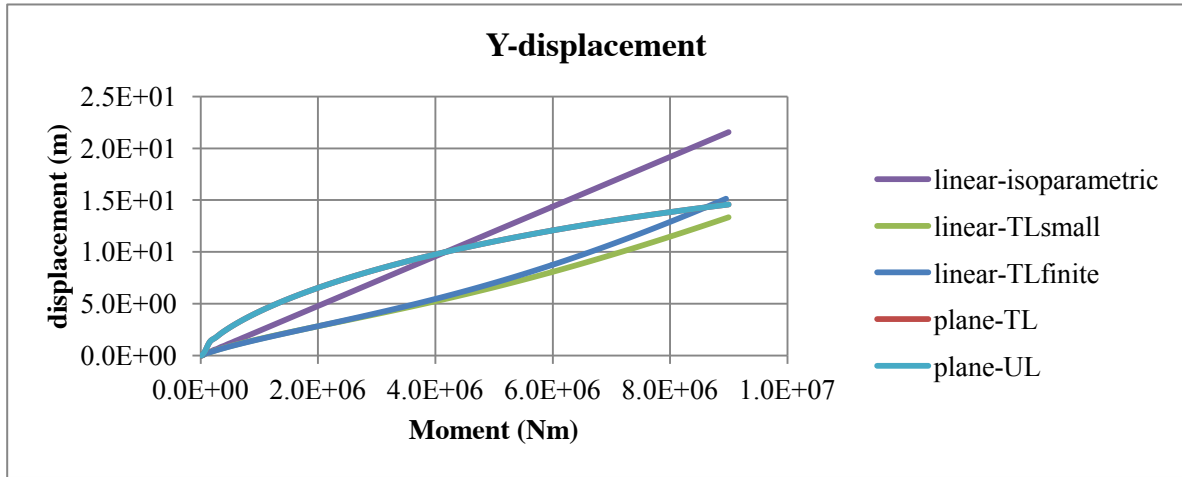


Fig. 3.13 - Comparison of y-displacements for moment analysis.

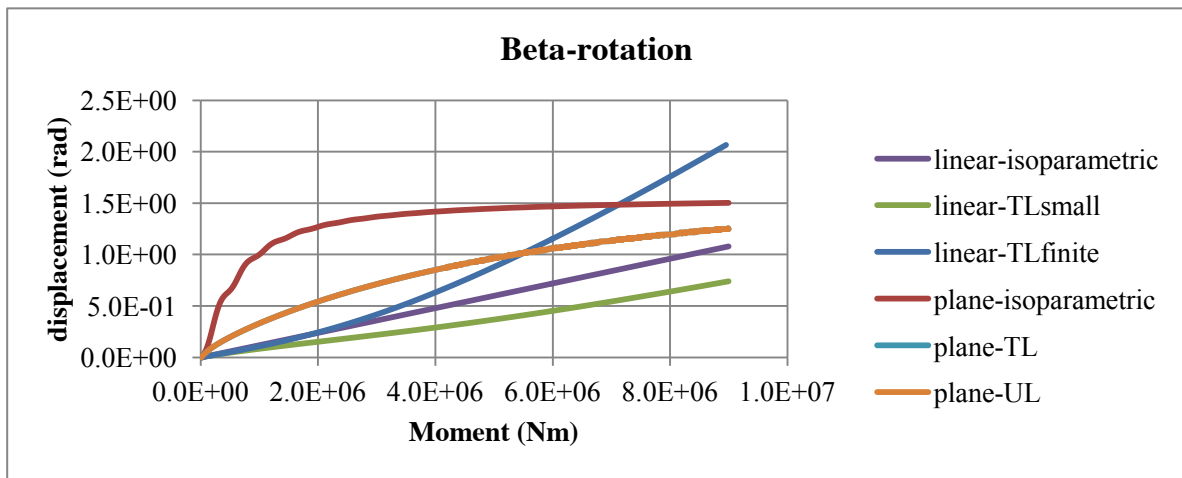


Fig. 3.14 - Comparison of beta-rotation for moment analysis.

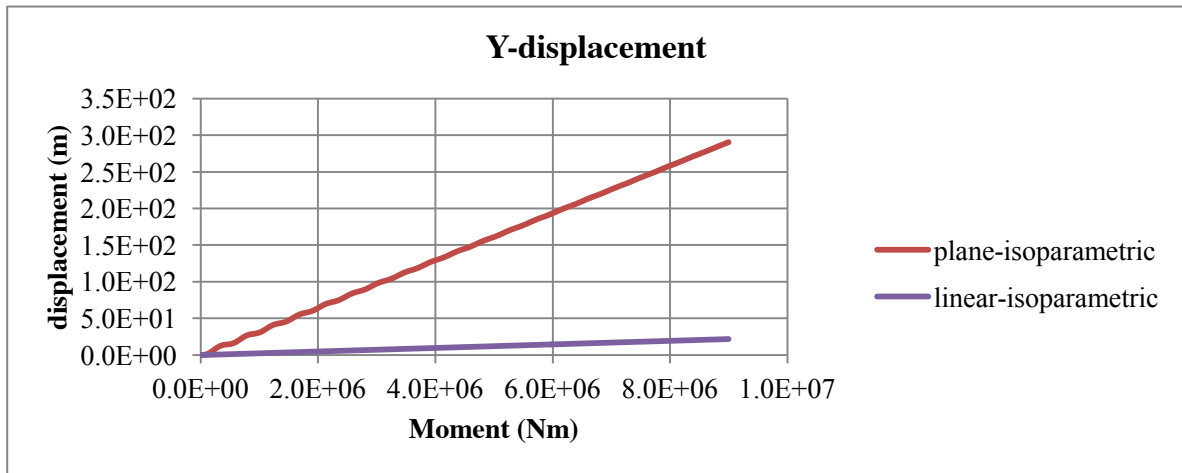


Fig. 3.15 - Comparison of y-displacement for moment analysis (shown separately due to scale).

An interesting phenomenon, similar to an element "stiffening" can be observed in the moment analysis of the Total Lagrangian formulation for small rotations (TLsmall). Hypothetically, this can be explained by considering that the small rotation formulation ignores larger order terms. Thus, when the same loads are applied to elements that use the small rotation and the finite rotation formulations, the computed displacements

will usually be smaller for the former than for the latter. This indicates that elements that use the TLsmall formulation tend to become "stiffer" when greatly rotated from its original position.

### 3.2.2 Strains

A comparison of the strains obtained in the moment analysis can be found on Figs. 3.16 to 3.18. In order to compare values from plane element mesh models to the values from linear meshes, the average between the resultant strain in correspondent plane elements was used.

Observe how there is a change in curvature for the strains and stresses that utilize the TLsmall formulation. In this analysis, this happened in element number 6, which very probably was the last one to rotate beyond the limit where element rotation is within acceptable values. Therefore the "stiffening" phenomenon hinted at by section 3.2.1 can be said to have happened in this analysis.

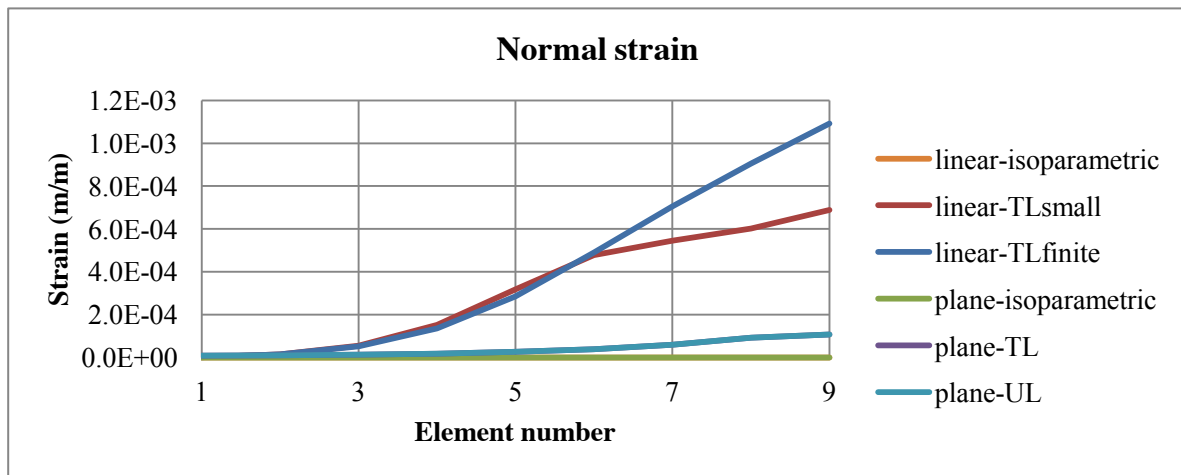


Fig. 3.16 - Normal strain profile comparison for moment analysis.

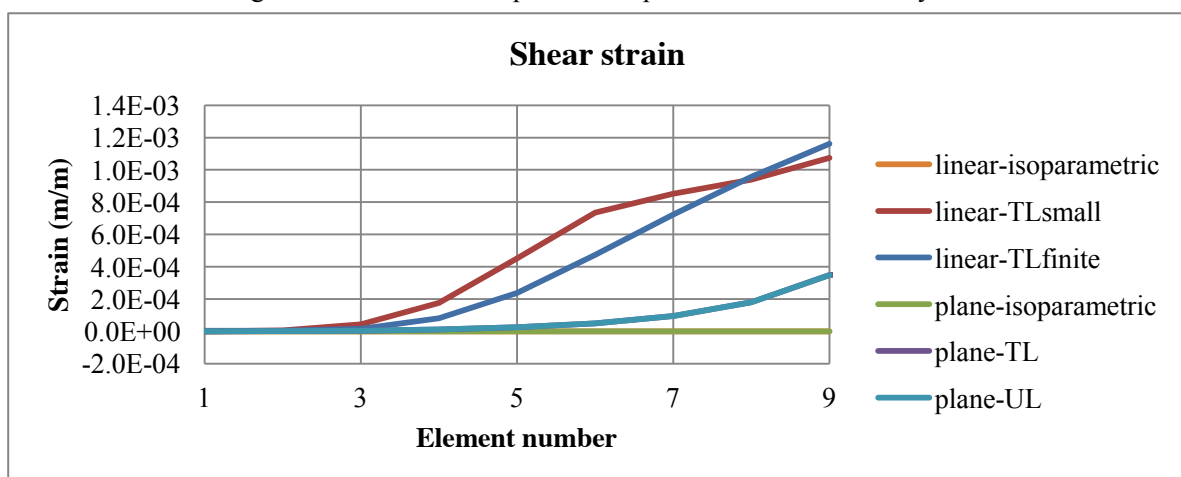


Fig. 3.17 - Shear strain profile comparison for moment analysis.



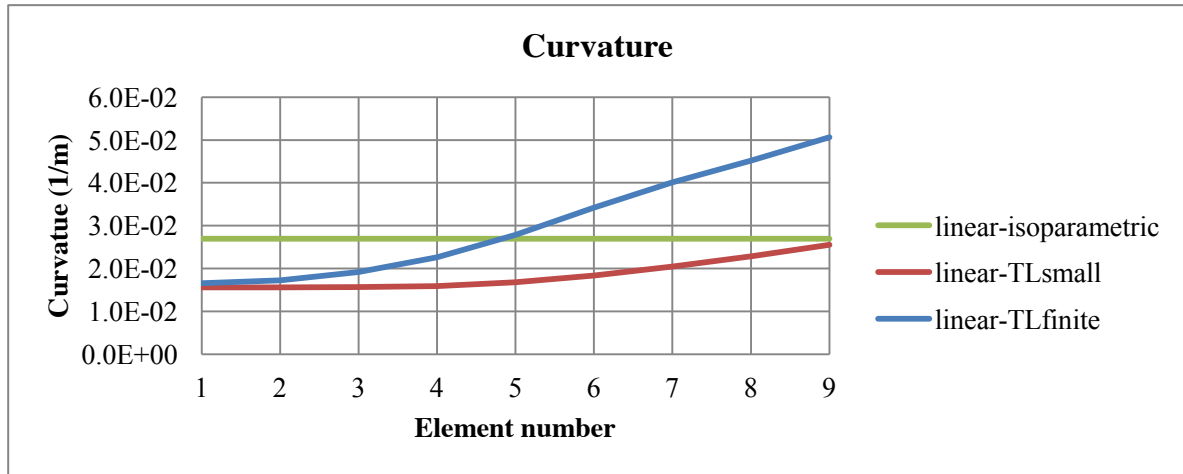


Fig. 3.18 - Curvature profile comparison for moment analysis.

### 3.2.3 Stresses

A comparative overview of the stress profiles for different pairs of meshes and formulations can be seen in Figs. 3.19 through 3.23. Note that the M-1 is the moment in node 1, M-2 is the moment in node 2, and M-0 corresponds to the "central" bending moment. In other words, M-0 can be thought of as portraying the amount of bending moment that was absorbed as energy by the beam in the form of curvature. This conceptual view of M-0 will be used in chapter 6.

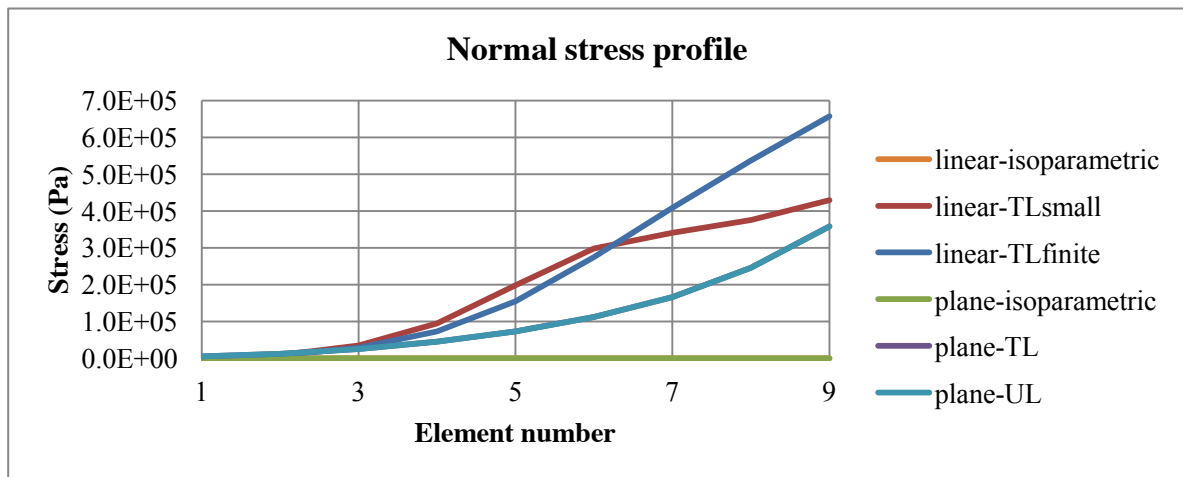


Fig. 3.19 - Normal stress profile comparison for moment analysis.

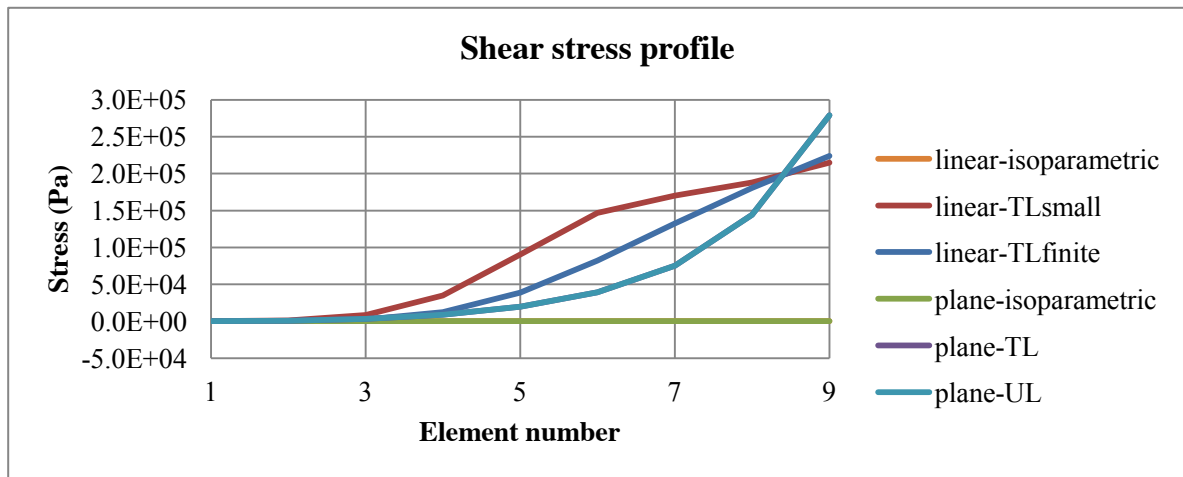


Fig. 3.20 - Shear stress profile comparison for moment analysis.

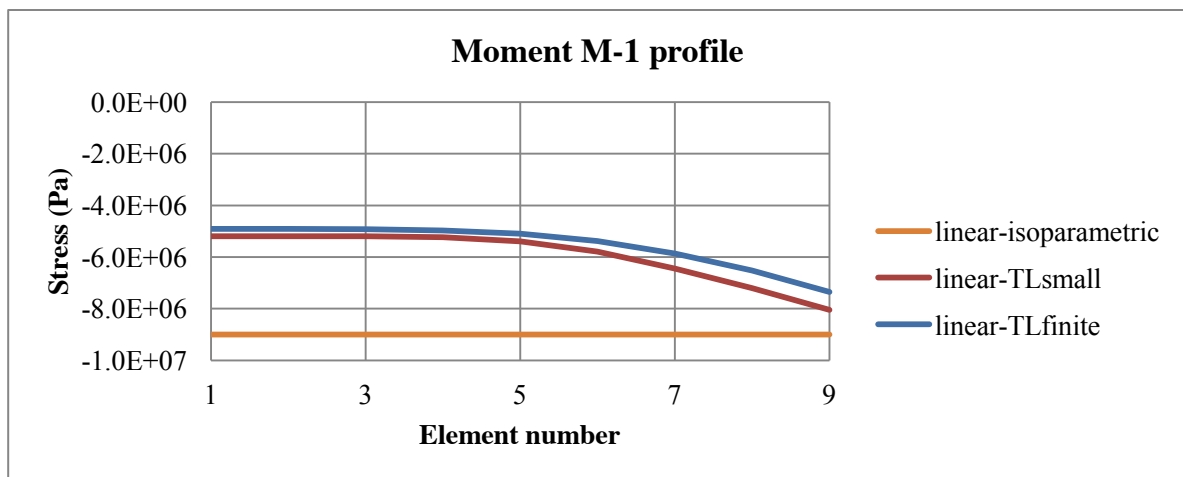


Fig. 3.21 - Bending moment M-1 profile comparison for moment analysis.

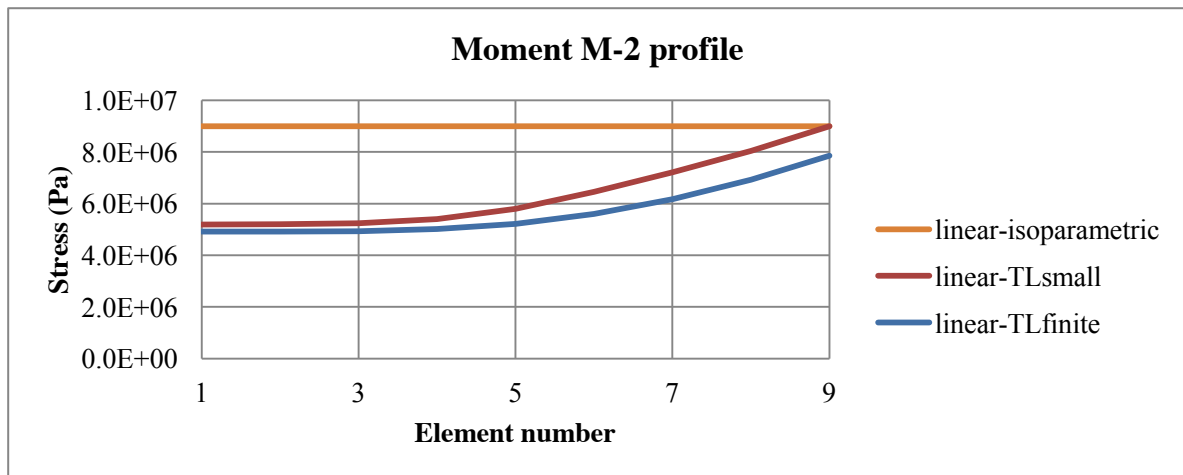


Fig. 3.22 - Bending moment M-2 profile comparison for moment analysis.

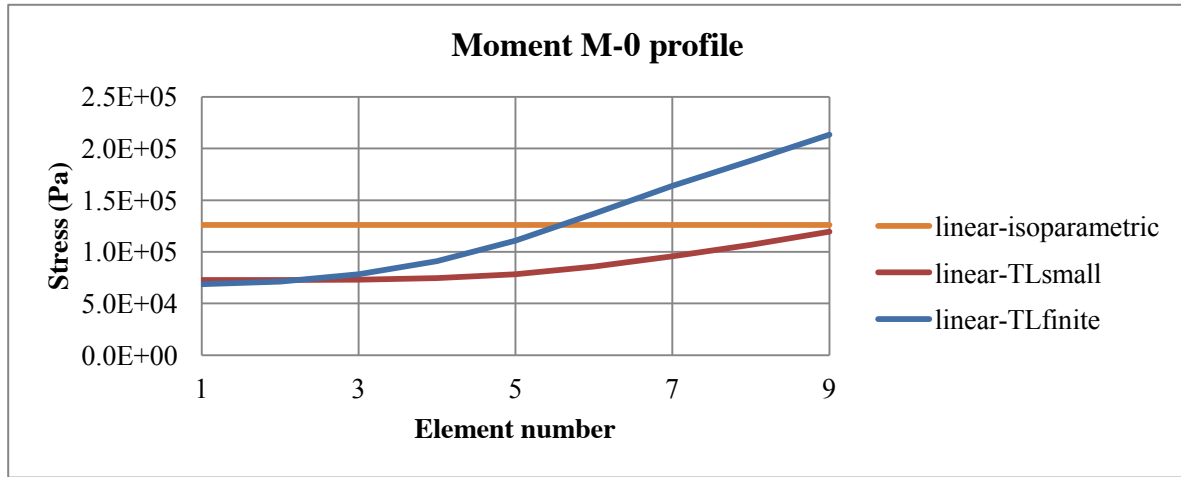


Fig. 3.23 - Bending moment M-0 profile comparison for moment analysis.

### 3.2.4 Position

For all of the eight distinct slopes presented in section 3.1.4, moment analysis was performed with both TLsmall and TLfinite formulations. This was also done in order to check for any errors in the behavior of the implemented beams. This was done by running simulations and checking results against each another, as seen in Fig. 3.24. The x- and y-displacements for the final deformed configurations have been calculated for the models presented here, and can be found on Tabs. 3.3 and 3.4. In these tables, there can also be found the full displacement and its deviation from average.

Note that the deviation peaks around a slope of 230 degrees (Fig. 3.24). This indicates that even larger values of deviation tend not to surpass 0.02%, which can be considered to be within reasonable bounds in the case of numerical simulations.

Tab. 3.3 - Displacement comparison moment analysis with formulation TLsmall.

Model	Slope (degrees)	U-X (m)	U-Y (m)	Displacement (m)	Deviation (%)
P1	0.0	-9.757	11.980	15.451	0.0063
P2	36.9	-14.990	3.731	15.447	-0.0144
P3	90.0	-11.980	9.757	15.451	0.0063
P4	126.9	-3.731	14.990	15.447	-0.0144
P5	180.0	-9.757	11.980	15.451	0.0063
P6	233.1	-15.440	0.617	15.452	0.0178
P7	270.0	-11.980	9.757	15.451	0.0063
P8	306.9	-3.731	14.990	15.447	-0.0144

Tab. 3.4 - Displacement comparison moment analysis with formulation TLfinite.

Model	Slope (degrees)	U-X (m)	U-Y (m)	Displacement (m)	Deviation (%)
P1	0.0	-11.250	13.470	17.550	0.0000
P2	36.9	-17.080	4.029	17.549	-0.0072
P3	90.0	-13.470	-11.250	17.550	0.0000
P4	126.9	-4.029	-17.080	17.549	-0.0072
P5	180.0	11.250	-13.470	17.550	0.0000
P6	233.1	17.530	0.915	17.554	0.0217
P7	270.0	13.470	11.250	17.550	0.0000
P8	306.9	4.029	17.080	17.549	-0.0072

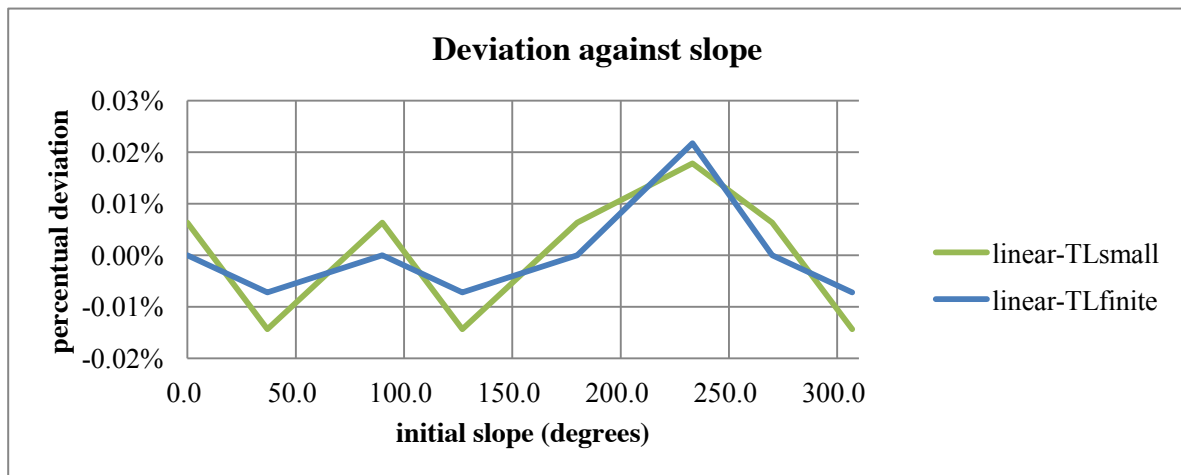


Fig. 3.24 - Deviation of tip displacement plotted against slope variation for position-check in moment analysis.

### 3.3 Shear analysis

#### 3.3.1 Displacements

The shear analysis consists of applying a shearing load on the tip of the beam. This approach has the peculiarity of making numerical convergence slightly more problematic than in the moment analysis. However, this analysis does allow for a clearer visualization of the interplay of strains and stresses in the proposed elements.

For this analysis, an exhaustive comparison of tip displacements of different pairs of meshes and formulations is shown in Figs. 3-25 through 3-27. A separate graph was plotted to display the analysis run on a mesh plane of elements with the isoparametric formulation (plane-isoparametric) due to the fact that its y-displacements are too large (Fig. 3-28). This is so due to the adoption of a formulation that assumes small displacements.

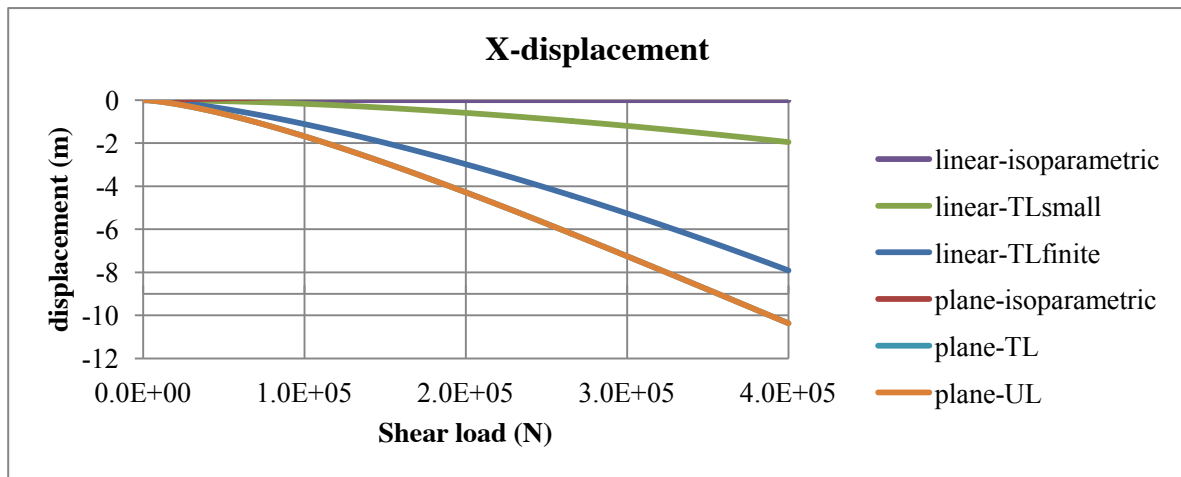


Fig. 3.25 - Comparison of x-displacements for shear analysis.

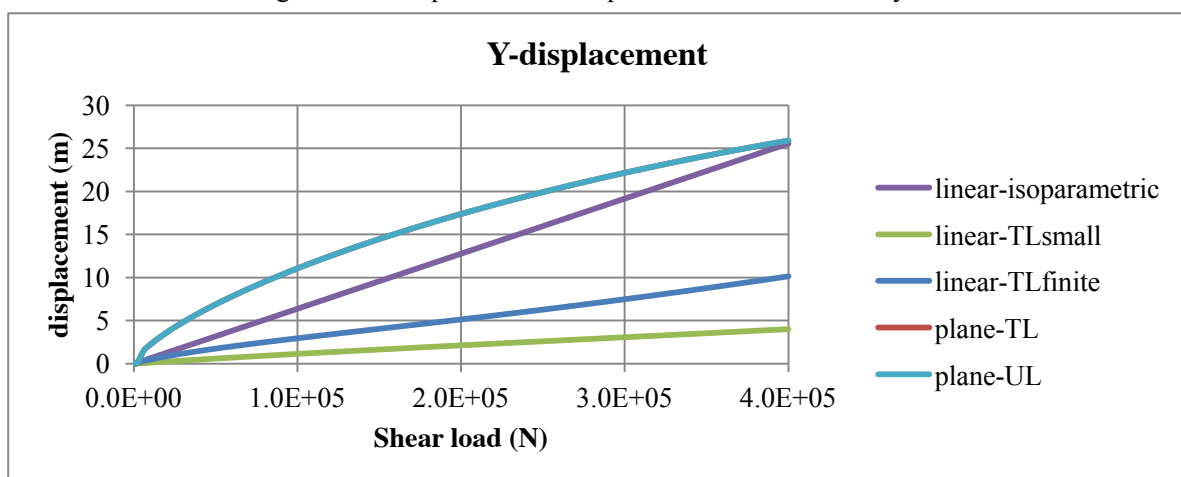


Fig. 3.26 - Comparison of y-displacements for shear analysis.

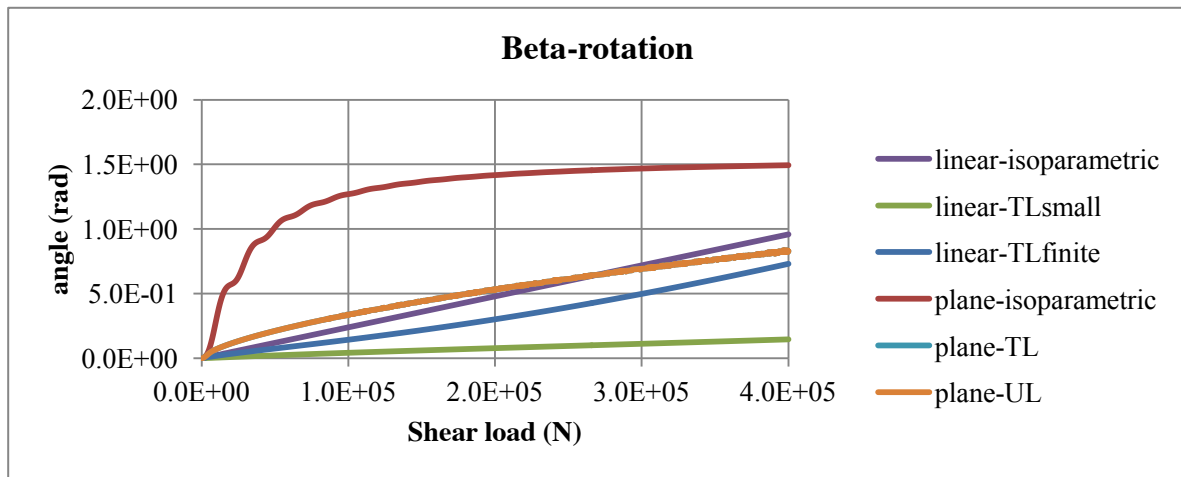


Fig. 3.27 - Comparison of beta-rotation for shear analysis.

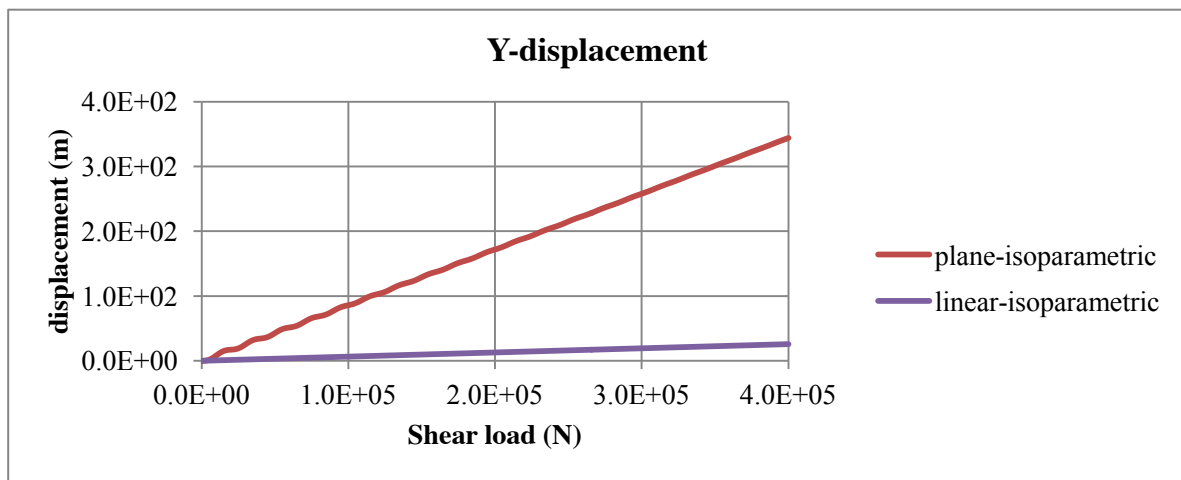


Fig. 3.28 - Comparison of y-displacements for shear analysis.

### 3.3.2 Strains

A comparison of the strains obtained in the moment analysis can be found on Figs. 3.29 to 3.31. Exactly as was in the moment analysis, the average between the resultant strain in correspondent plane elements was used.

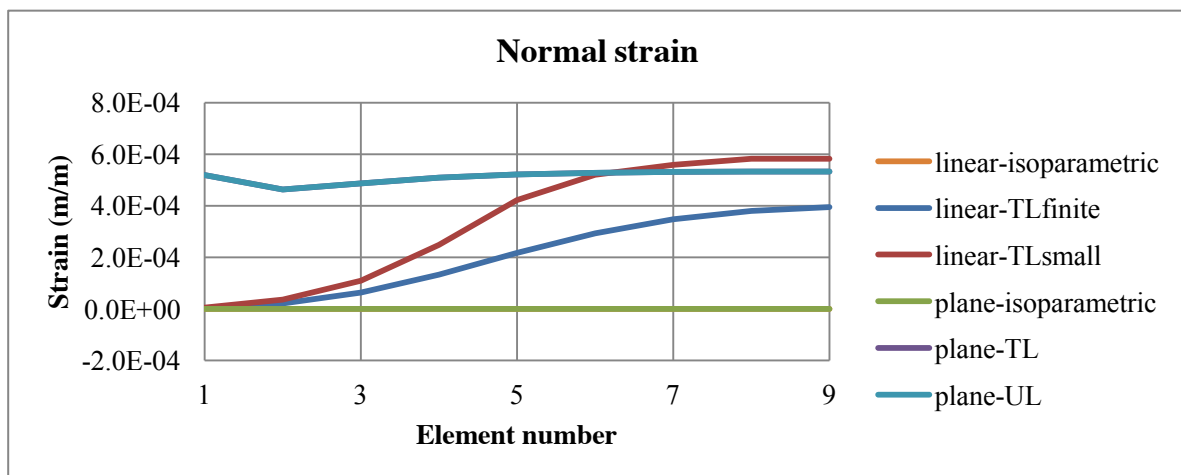


Fig. 3.29 - Normal strain profile comparison for shear analysis.

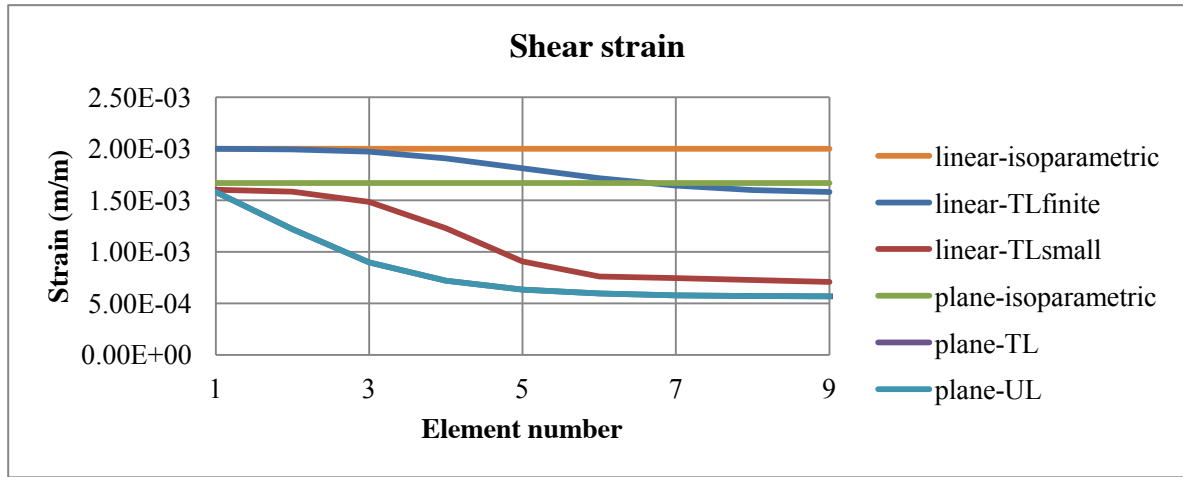


Fig. 3.30 - Shear strain profile comparison for shear analysis.

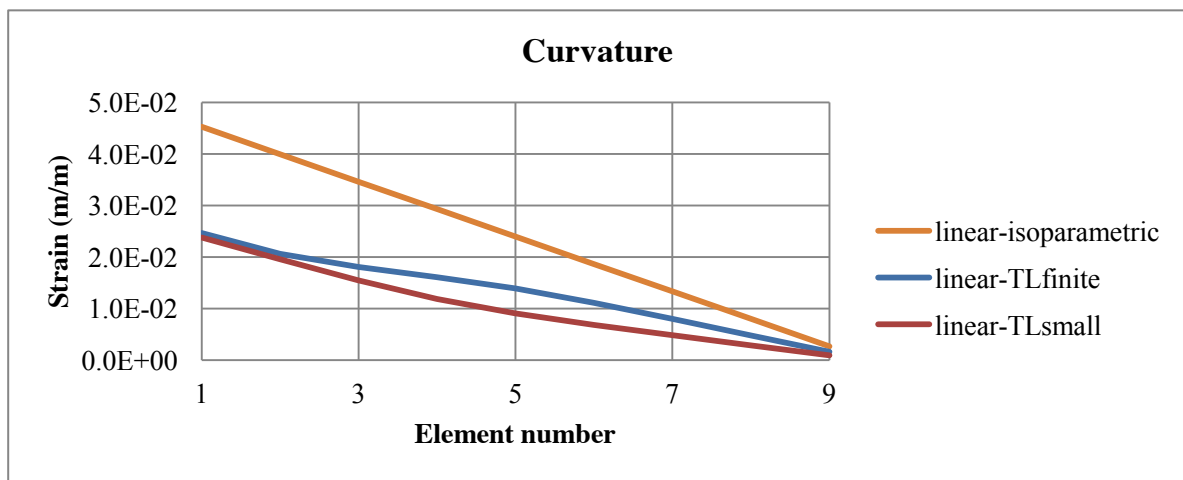


Fig. 3.31 - Curvature profile comparison for shear analysis.

### 3.3.3 Stresses

A comparative overview of the stress profiles for different pairs of meshes and formulations can be seen in Figs. 3.32 through 3.36. Note that the M-1 is the moment in node 1, M-2 is the moment in node 2, and M-0 corresponds to the "central" bending moment. In other words, M-0 can be thought of as portraying the amount of bending moment that was absorbed as energy by the beam in the form of curvature. This conceptual view of M-0 will be used in chapter 6.

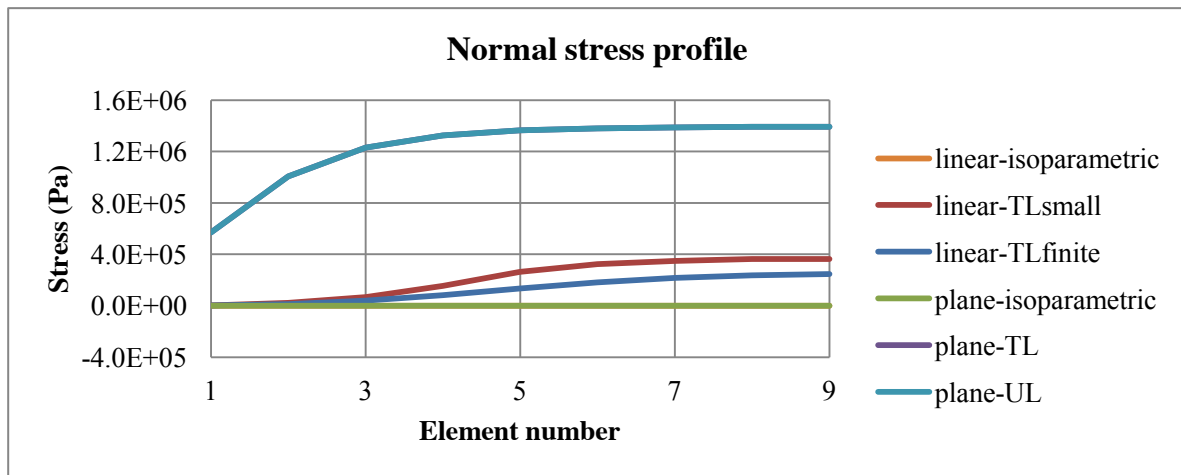


Fig. 3.32 - Normal stress profile comparison for shear analysis.

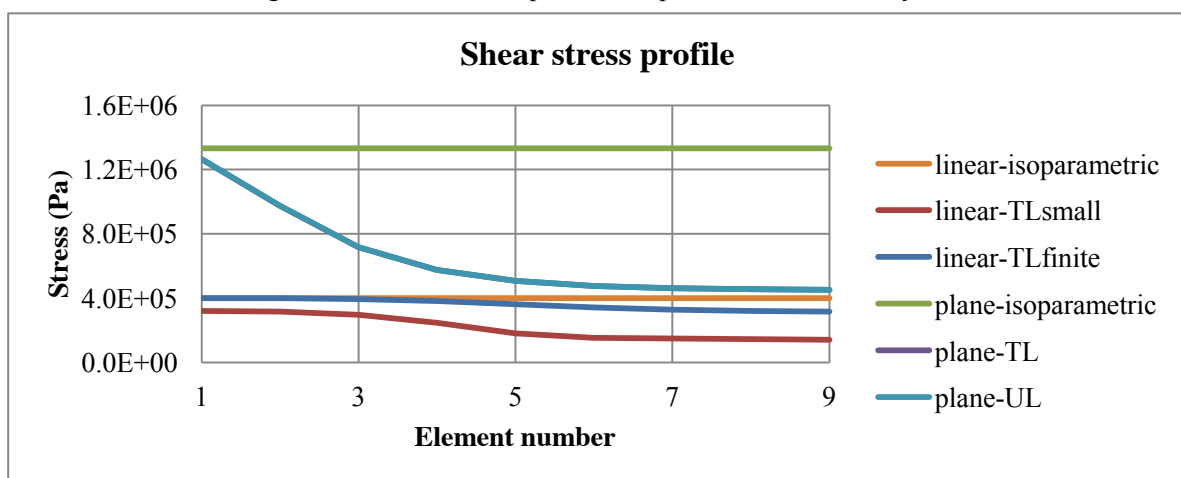


Fig. 3.33 - Shear stress profile comparison for shear analysis.

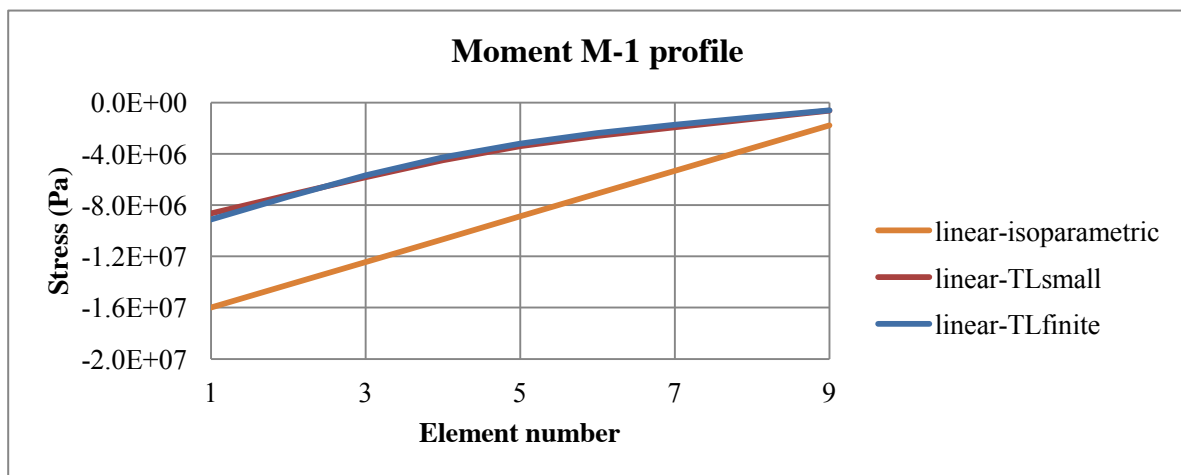


Fig. 3.34 - Moment M-1 profile comparison for shear analysis.



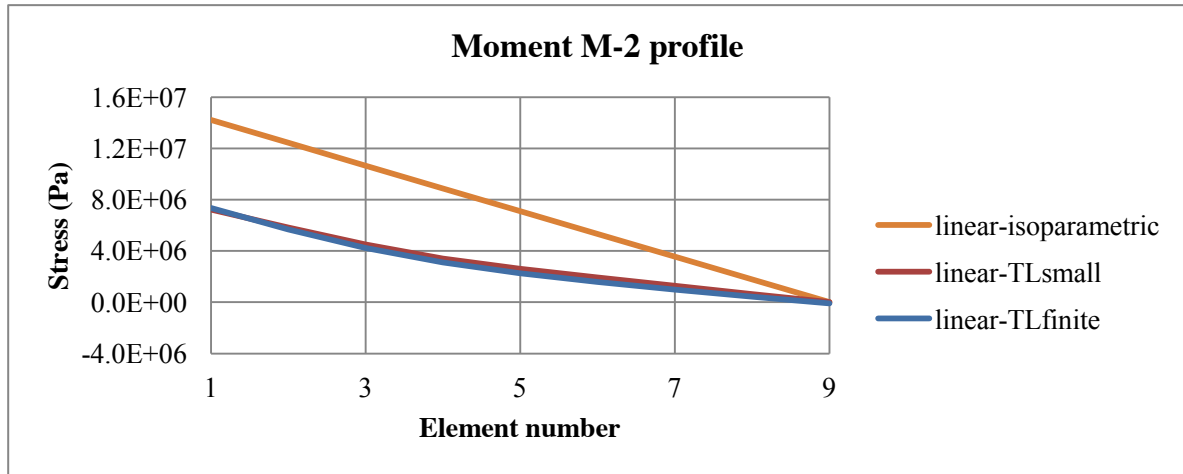


Fig. 3.35 - Moment M-2 profile comparison for shear analysis.

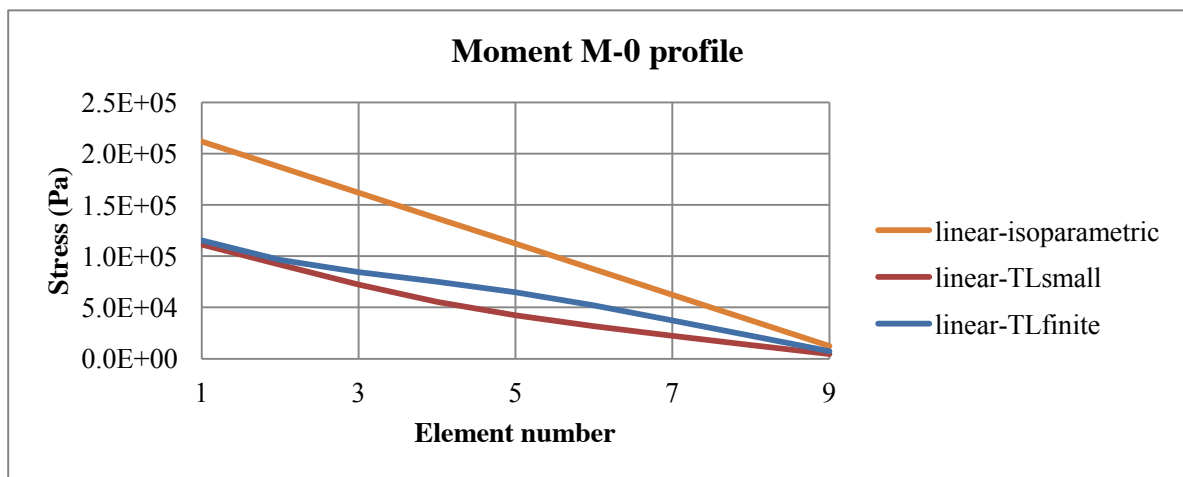


Fig. 3.36 - Moment M-0 profile comparison for shear analysis.

### 3.3.4 Position

For all of the eight distinct slopes presented in section 3.1.4, shear analysis was performed with both TLsmall and TLfinite formulations, in the same manner shown in section 3.2.4 with moment analysis. This was done by running simulations and checking results against each another, as seen in Fig. 3.37. The x- and y-displacements for the final deformed configurations have been calculated for the models presented here, and can be found on Tabs. 3.5 and 3.6. In these tables, there can also be found the full displacement and its deviation from average.

Note that - similarly to the moment analysis - deviation only occurs around a slope of 230 degrees (Fig. 3.37). This deviation is around 0.03%, and is within acceptable limits for a numerical simulation.

Tab. 3.5 - Displacement comparison shear analysis with formulation TLsmall.

Model	Slope (degrees)	U-X (m)	U-Y (m)	Displacement (m)	Deviation (%)
001	0.0	8.075	10.300	13.088	-0.0048
002	36.9	12.640	3.395	13.088	-0.0048
003	90.0	10.300	8.075	13.088	-0.0048
004	126.9	-3.395	-12.640	13.088	-0.0048
005	180.0	8.075	-10.300	13.088	-0.0048
006	233.1	13.090	0.281	13.093	0.0335
007	270.0	10.300	8.075	13.088	-0.0048
008	306.9	3.395	12.640	13.088	-0.0048

Tab. 3.6 - Displacement comparison shear analysis with formulation TLfinite.

Model	Slope (degrees)	U-X (m)	U-Y (m)	Displacement (m)	Deviation (%)
001	0.0	-4.668	6.881	8.315	-0.0006
002	36.9	-7.863	2.704	8.315	-0.0006
003	90.0	-6.881	-4.668	8.315	-0.0006
004	126.9	-2.704	-7.863	8.315	-0.0006
005	180.0	4.668	-6.881	8.315	-0.0006
006	233.1	8.306	-0.394	8.315	0.0040
007	270.0	6.881	4.668	8.315	-0.0006
008	306.9	2.704	7.863	8.315	-0.0006

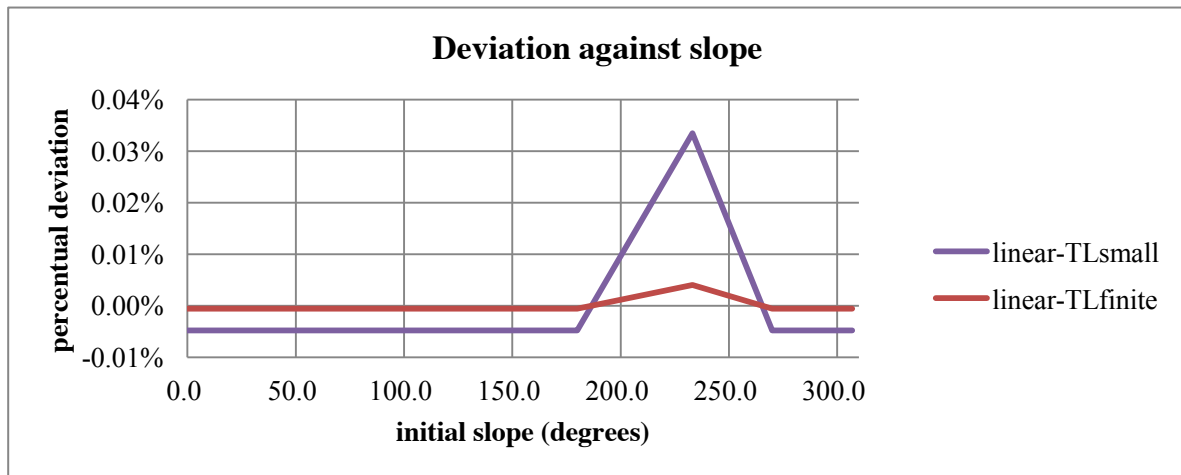
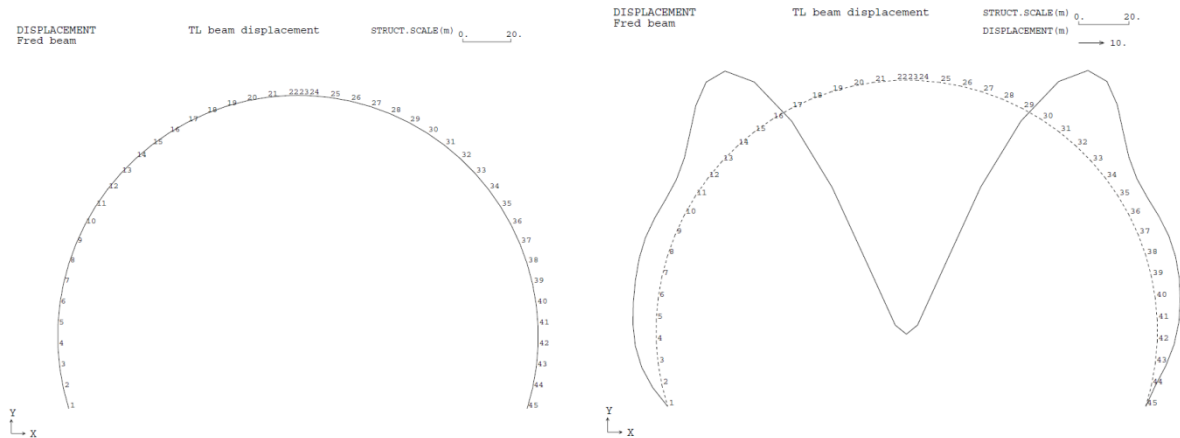


Fig. 3.37 - Deviation of tip displacement plotted against slope variation for position-check in shear analysis.

### 3.4 Clamped-hinged arch analysis

This section was inspired by the appearance of clamped-hinged arches in textbooks in their respective sections about large displacement beams. This analysis' results are probably common because of the way it shows the discrepancy in resulting behavior (see Fig. 3.38).



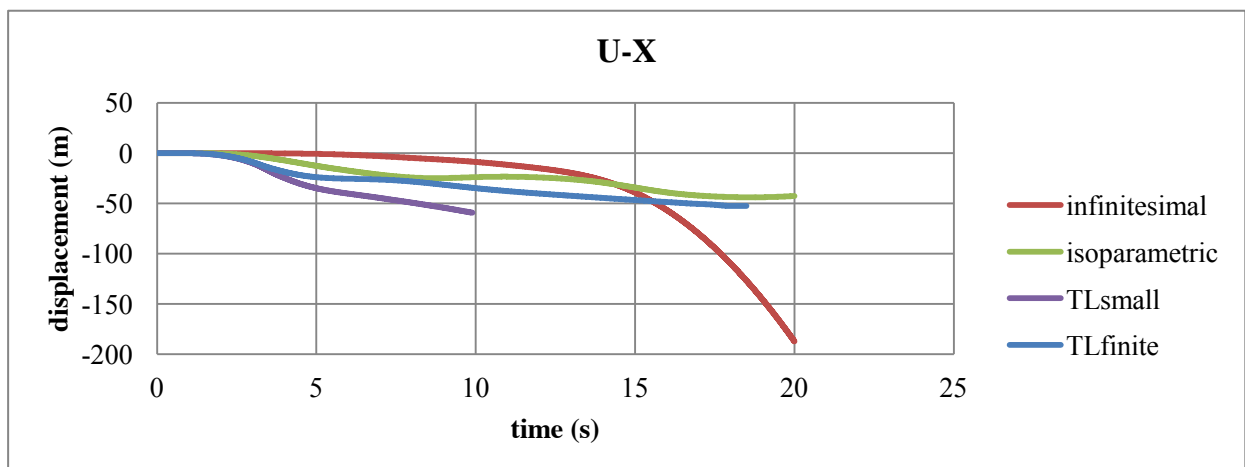
(a) initial configuration (b) deformed configuration for infinitesimal formulation

Fig. 3.38 - Mesh for clamped-hinged arch analysis.

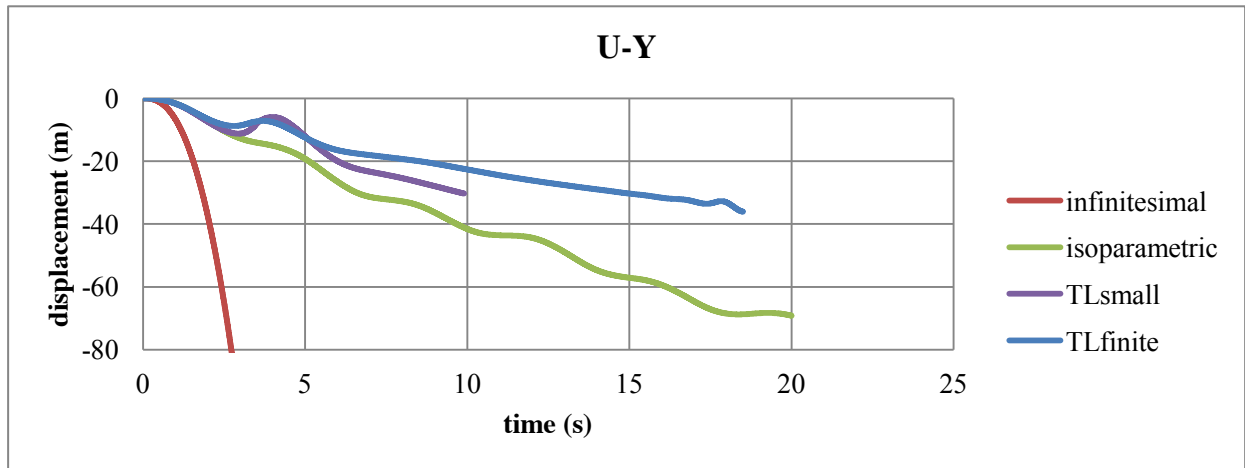
### 3.4.1 Displacements

Resulting displacements are shown in Fig. 3.39, and it is possible to follow the evolution of these curves throughout time (and the corresponding loading conditions). This allows the analyst to see exactly when each formulation loses its validity. For example, in the case of infinitesimal formulation: its rotation angle roughly follows the curve for TLfinite up to approximately five seconds into the simulation, but that only happens for the x-displacement after fifteen seconds.

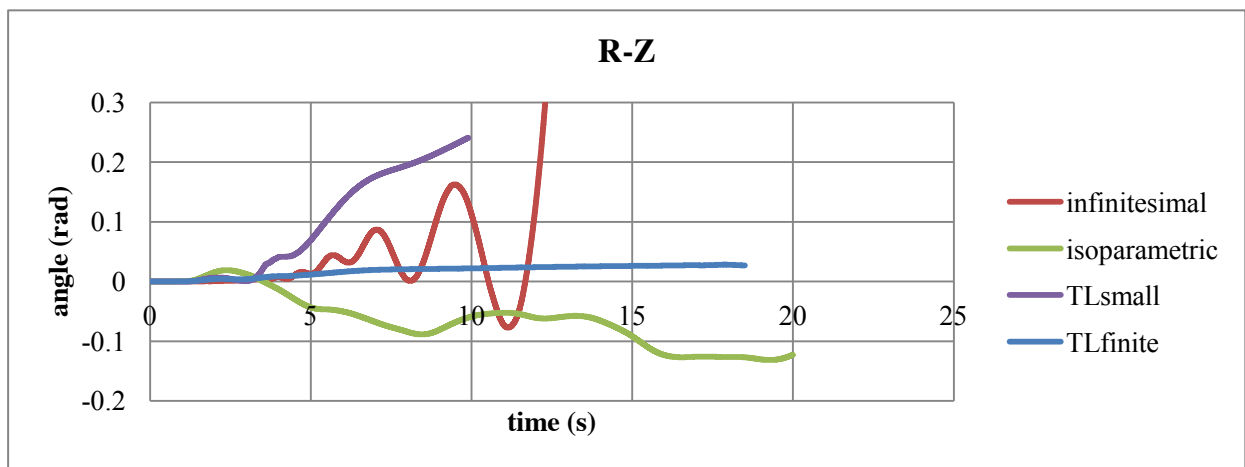
Also noteworthy, the patterns of oscillation seen in Fig. 3.39c are distinct between formulations, and might be an important factor to help understand the inner workings of finite element formulations.



(a)



(b)



(c)

Fig. 3.39 - Comparison of displacements for formulations for node 23 in clamped-hinged arch analysis.

### 3.5 Tentative conclusions

The proposed formulations show a robust behavior, and can be relied on to accurately simulate large displacements. They are much more demanding of computational power due to the need to compute their tangent stiffness matrix at each step, and they are much less stable numerically than their infinitesimal counterparts, as is to be expected. However, even when submitted to loads large enough to imply meaningless output from their infinitesimal counterparts, the proposed formulations behave nicely. Meaningless output as referred to here, simply means the output of results that are clearly impossible physically, such as seen in Fig. 3-28.

During the course of these analyses, it was apparent that elements with both proposed formulations suffered from divergence whenever they were rotated to about 90 degrees from their initial position. This issue is more prevalent in the formulation for small rotations, but it also occurred in the finite rotations formulation. In the small rotation formulation, this is certainly due to the adopted simplifications. In the finite rotation formulation, this can be attributed to the use of bare trigonometric functions in the underlying implementation, and must not be regarded as a formulation issue.

Some possible lines for future research are as follows:

- ✓ Exhaustive exploration and solution of the caveats presented by the direct use of trigonometric functions for rotation.
- ✓ Further inquiry as to what exactly the concept of reducing what in actuality is a full-blown tridimensional material in the physical universe into a linear domain that responds to no more than three simple types of stresses. More importantly, the insights obtained in such inquiry may aid the understanding of more complex elements, and this may yet prove invaluable to the analysis of highly complex materials, such as soil.

## 4 Buckling

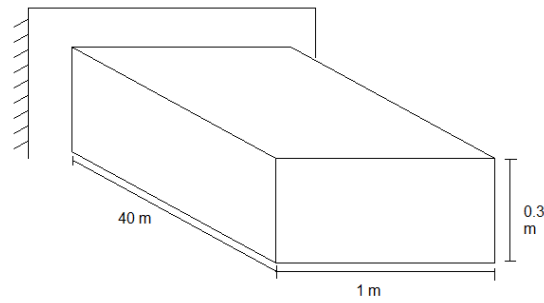


Fig. 4.1 - Geometry of cantilever beam used for initial buckling analysis.

The buckling of beams is a process that can be observed in slender beams, and it is characterized by a loss of stability beyond a certain critical load. Moreover, this loss of stability must be observed in loading conditions that would not be sufficient to cause the material to fail. In this section, the single most important problem is that of determining the critical buckling load for the idealized beam that was used for analysis and is shown in Fig. 4.1. Its material properties can be found on Tab. 4.1.

Tab. 4.1 - Geometric and material properties chosen for buckling analysis.

Property	Value
E (GPa)	2.09
$\nu$	0.3
G (MPa)	800
A (m <sup>2</sup> )	0.3
I (10 <sup>-4</sup> m <sup>4</sup> )	22.5

### 4.1 Overview of buckling methodology

First and foremost, a few analyses were run utilizing a mesh of plane elements formulated using the Total Lagrangian method (TL). These analyses had the goal of assessing the behavior of beams already implemented with the TL approach. This analysis sets the stage for an initial analysis of the proposed elements. The next step up from both these analyses consists of using the insights obtained up to here in order to concoct what is referred to later as a refined analysis.

### 4.2 Plane Elements Mesh

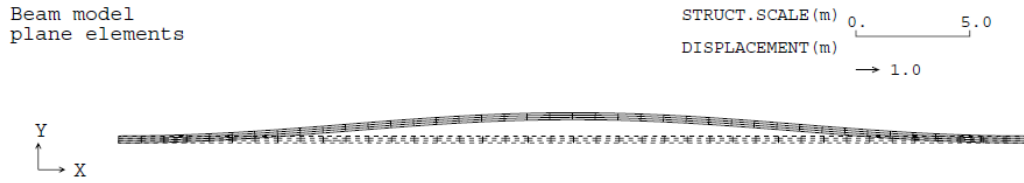


Fig. 4.2 - Deformed configuration of plane-TL beam after buckling.

Once again, a mesh of plane elements formulated using the Total Lagrangian approach was used for comparison purposes. Fig. 4.2 shows one among the many possible deformed configurations. The reason why these simulations lead to the beam buckling upwards or downwards are mostly arbitrary, and not directly related to parameters of the numerical simulation. With this particular mesh, the parameter used to cause it to change the direction of buckling was the seemingly unrelated convergence tolerance factor  $\varepsilon_2$ . For this particular analysis,  $\varepsilon_2 = 10^{-3}$  lead to upwards buckling, whereas  $\varepsilon_2 = 10^{-4}$  lead to downwards buckling.

Note that the analysis of this mesh is handy because of the insight that can be obtained out of its strain and stress curves.

#### 4.2.1 Indicators of buckling

The main objective of this section is to check the behavior of existing elements with Total Lagrangian formulations when submitted to buckling conditions. This is done in order to visualize the sharp change to be expected when they buckle.

#### 4.2.2 Strains

The beam is modeled as three lines of thin elements. The lower line contains elements 1 through 40, the middle line contain elements 41 through 80, and the upper line contains elements 81 through 120. The strain curves for the tip elements (numbered 40, 80, 120) in upwards and downwards buckling can be seen in Figs. 4.3 and 4.4. These curves show a sharp transition between regular stability and instability.

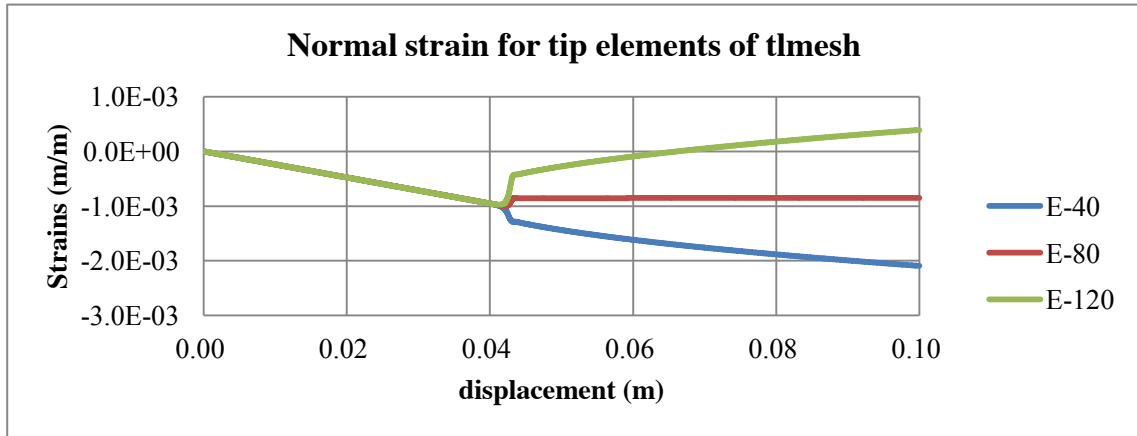


Fig. 4.3 - Normal strain curves for downward buckling of plane-TL model.

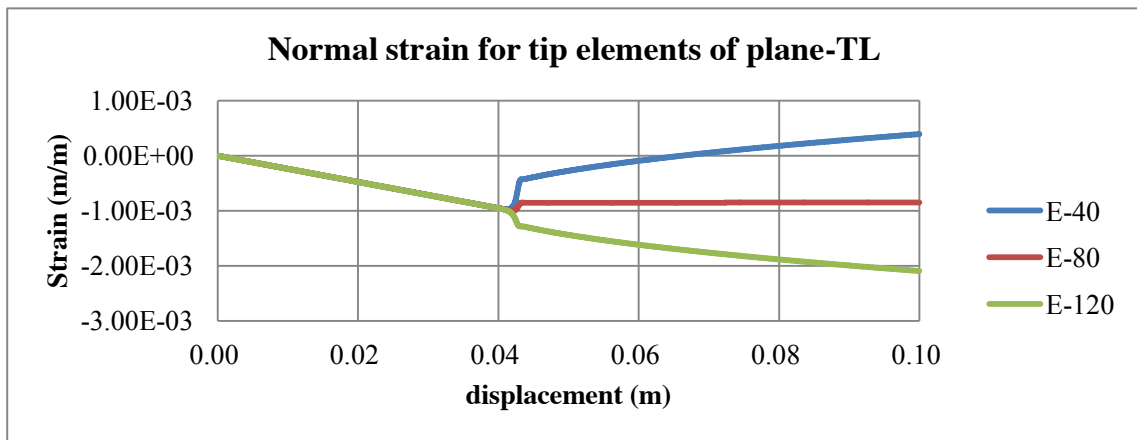


Fig. 4.4 - Normal strain curves for upward buckling of plane-TL model.

#### 4.2.3 Stresses

Stress curves show behavior similar to that of strain curves, as expected (Fig. 4.5).

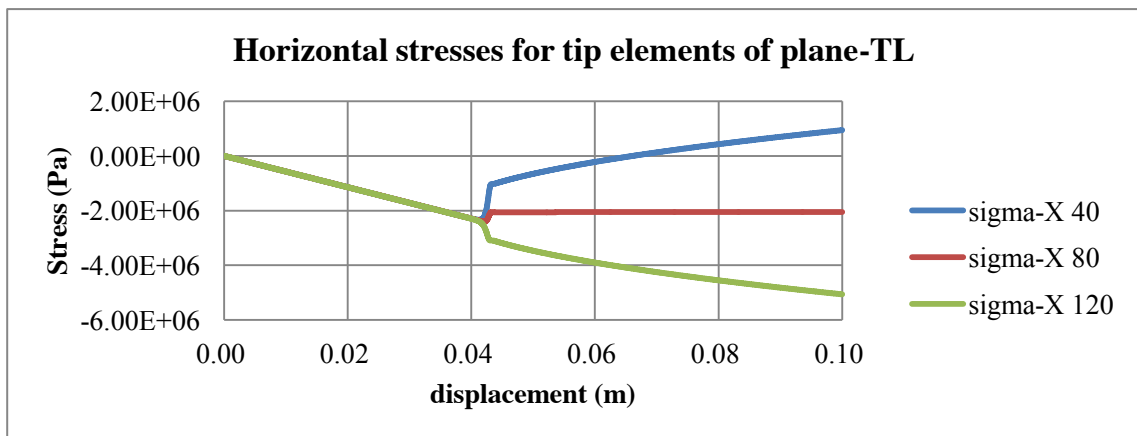


Fig. 4.5 - Normal strain curves for upward buckling of plane-TL model.



#### 4.2.4 Reaction

In order to obtain the critical buckling load, the curves portraying the reaction against the displacement applied to the tip of the plane-TL beam, as seen in Fig. 4.6. The reaction curve shows a clear maximum value, and that can be taken to be the critical buckling load. The critical buckling load determined through this method, for this particular simulation was:

$$F_{\text{crit}} = 7.2106 \times 10^5 \text{ N} \quad \text{Eq. 4-1}$$

This value is reasonably close to the value obtained through Euler's formula:

$$F_{\text{crit}} = \frac{\pi^2 EI}{(KL)^2} = 1.1547 \times 10^5 \text{ N} \quad \text{Eq. 4-2}$$

where parameter  $K=2$ , because all four nodes in the tips of these meshes are constrained.

The data used to plot the graph in Fig. 4.5 can also be used in order to observe the sudden appearance of a moment on the tip of the beam. This appearance should coincide with buckling, and so the following formulae were used to calculate the tip reaction and moment:

$$R = \int \sigma_x dA = \sigma_{x,40} A_{40} + \sigma_{x,80} A_{80} + \sigma_{x,120} A_{120} = (\sigma_{x,40} + \sigma_{x,80} + \sigma_{x,120}) A \quad \text{Eq. 4-3}$$

$$M = \int \sigma_x y dA = \sigma_{40} A_{40} y_{40} + \sigma_{80} A_{80} y_{80} + \sigma_{120} A_{120} y_{120} = (\sigma_{x,40} y_{40} + \sigma_{x,120} y_{120}) A_{40} \quad \text{Eq. 4-4}$$

where  $A_{40} = A_{80} = A_{120} = \frac{A}{3}$ , and  $y_{80} = 0$  because  $y$  is measured from the center of the beam. The resulting curves can be found on Fig. 4.7.

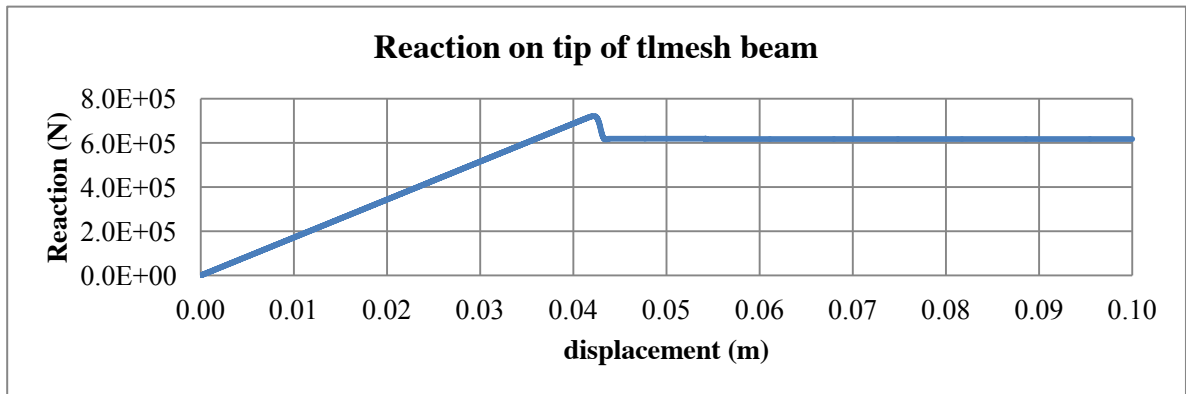


Fig. 4.6 - Force in the nodes making the tip of the plane-TL beam.

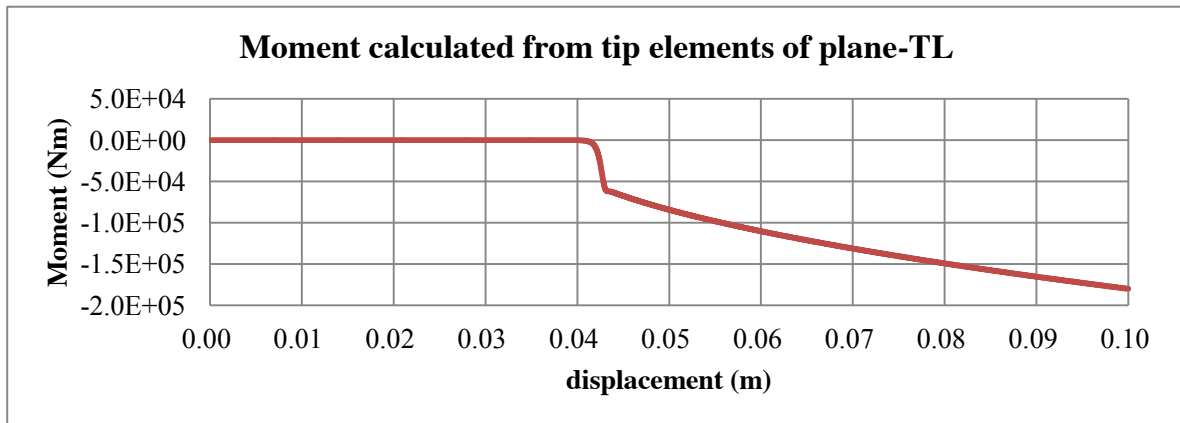


Fig. 4.7 - Calculated bending moment for the tip of the plane-TL beam.

This shows that the main indicator that buckling has occurred is the sudden appearance of bending moment. Tentatively, this can be used to detect the buckling of linear beam elements.

### 4.3 Initial Inspection

#### 4.3.1 Dynamic analysis and Symmetry

Initially, a buckling analysis that was similar to the previously presented analysis was performed. The mesh that was used for this analysis can be seen in Fig. 4.8. The beam is then loaded by means of a forced displacement  $d = 0.1\text{m}$  applied to node 1 (on the left). This beam is simply supported.

Also, note that this analysis is not symmetric, because the displacement is only applied to node 1.

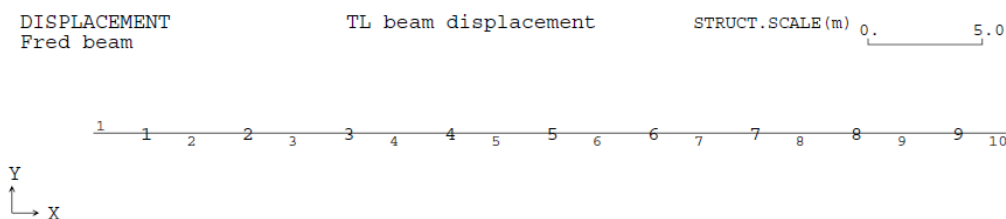


Fig. 4.8 - Mesh for initial inspection of buckling.

#### 4.3.2 Displacements

The resulting displacements can be seen in Figs. 4.9 and 4.10. Note that, as the analysis progresses, the lack of symmetry shows up more prominently in results.

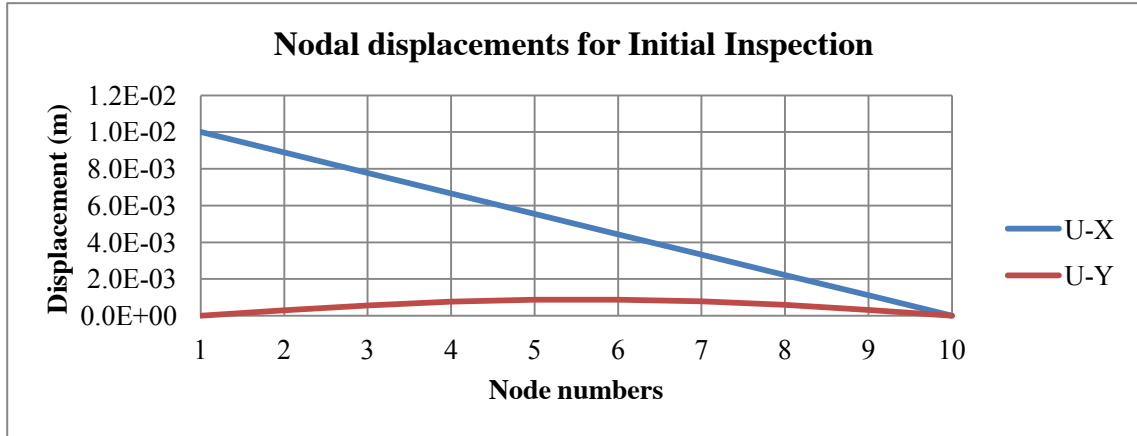


Fig. 4.9 - Nodal displacements for initial inspection of buckling for an applied displacement of  $d=0.01\text{m}$ .

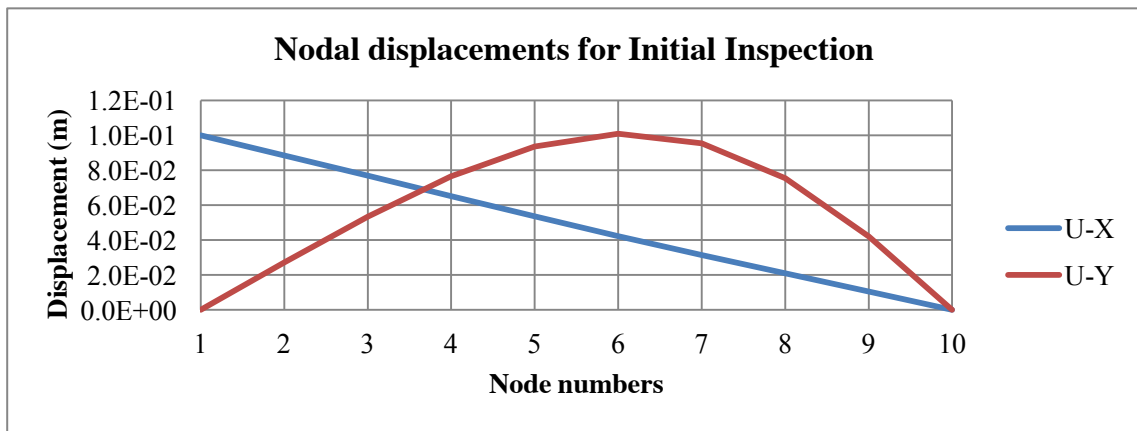


Fig. 4.10 - Nodal displacements for initial inspection of buckling for an applied displacement of  $d=0.1\text{m}$ .

#### 4.3.3 Strains

Representative strain distributions for this analysis can be found in Figs. 4.11 and 4.12. As for the variation of the normal strain, it is small enough to be attributed to the fact that this analysis was dynamic, and thus might be accounted for through considerations regarding the speed of propagation of elastic waves in solids, this, however, lies outside the scope of the present work.

A very interesting aspect of this analysis is shown in Fig. 4.13. This is that the shear strain distribution is not symmetric. The point in which it is zero doesn't coincide with the center of element 5, the central element. This asymmetry cannot be said to correspond to an expected behavior of the actual beam that's been simulated. Thus, it must be regarded as an error in the solution, introduced by the process of modeling and/or numerical simulation. As the simulation continues, this asymmetry becomes more and more pronounced, causing the results obtained by these means to be unusable.

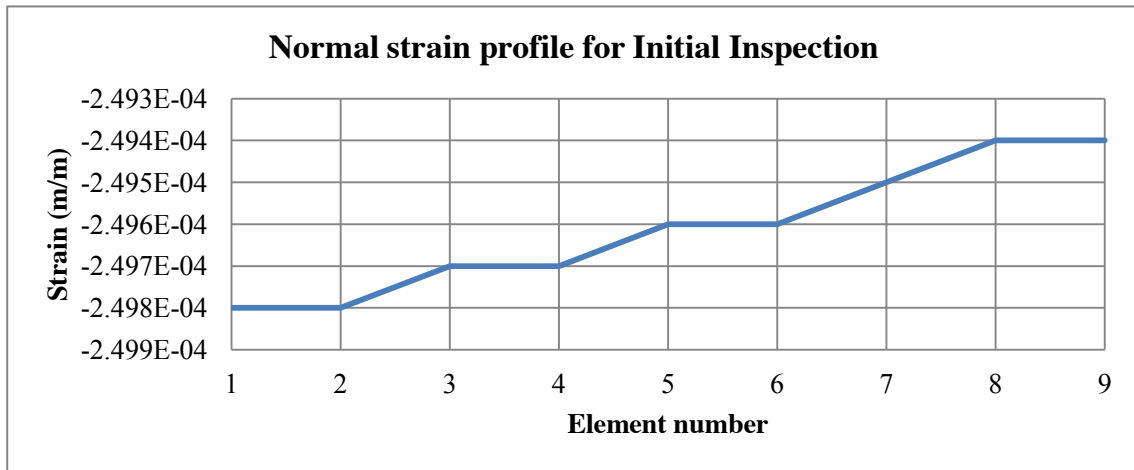


Fig. 4.11 - Normal strain distribution for beam in this analysis for displacement  $d = 0.01\text{m}$ .

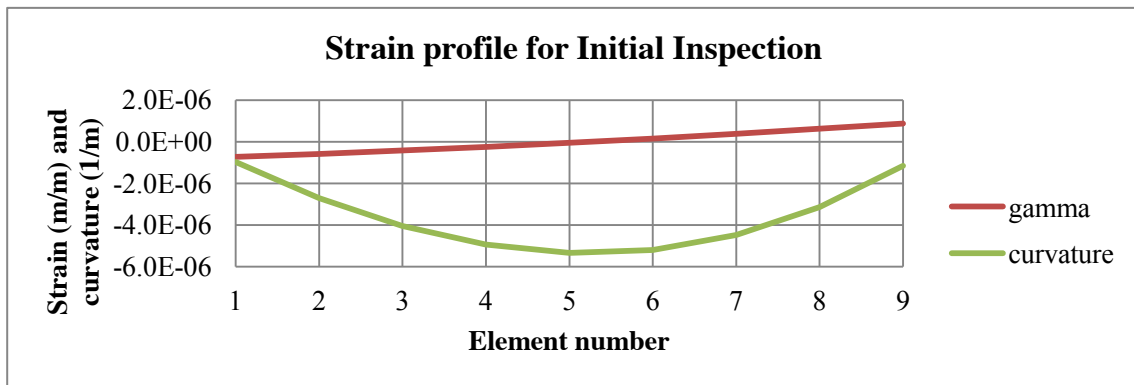


Fig. 4.12 - Shear strain and curvature distribution for beam in this analysis for displacement  $d = 0.01\text{m}$ .

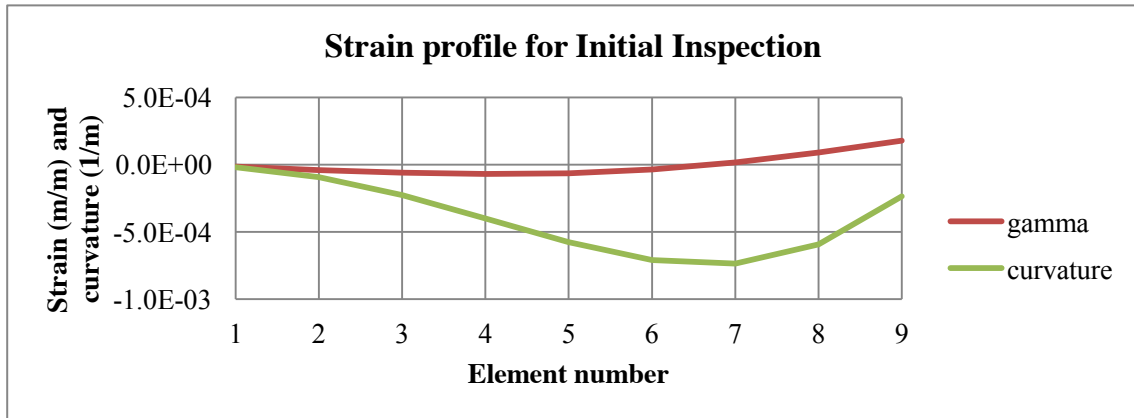


Fig. 4.13 - Shear strain and curvature distribution for beam in this analysis for displacement  $d = 0.1\text{m}$ .

#### 4.3.4 Stresses

Similar results in the stress distributions for this analysis can be observed in Figs. 4.14 through 4.16.

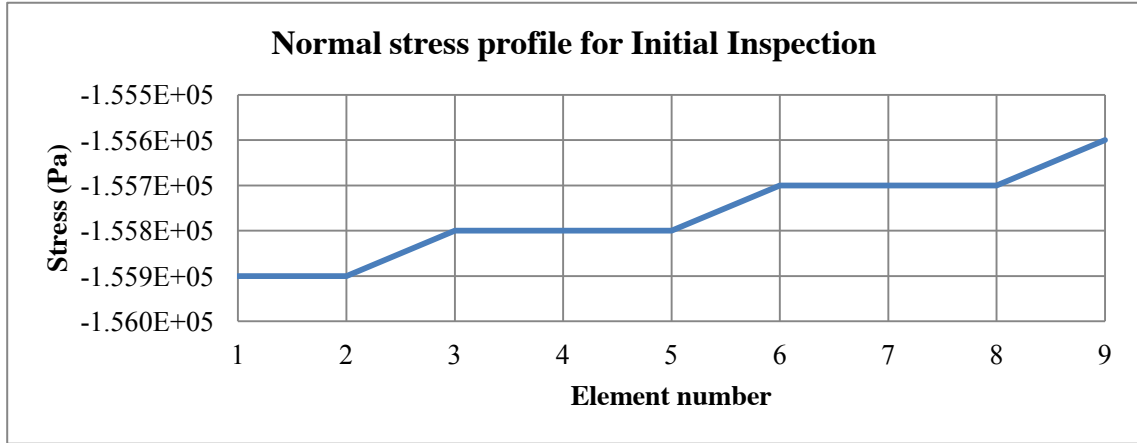


Fig. 4.14 - Stress distribution for beam in analysis 001 for applied displacement  $d = 0.01\text{m}$ .

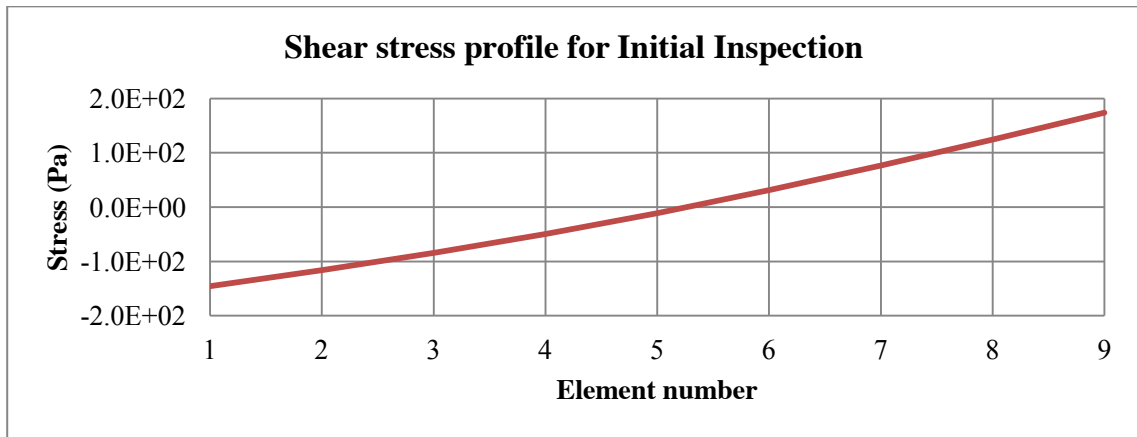


Fig. 4.15 - Stress distribution for beam in analysis 001 for applied displacement  $d = 0.01\text{m}$ .

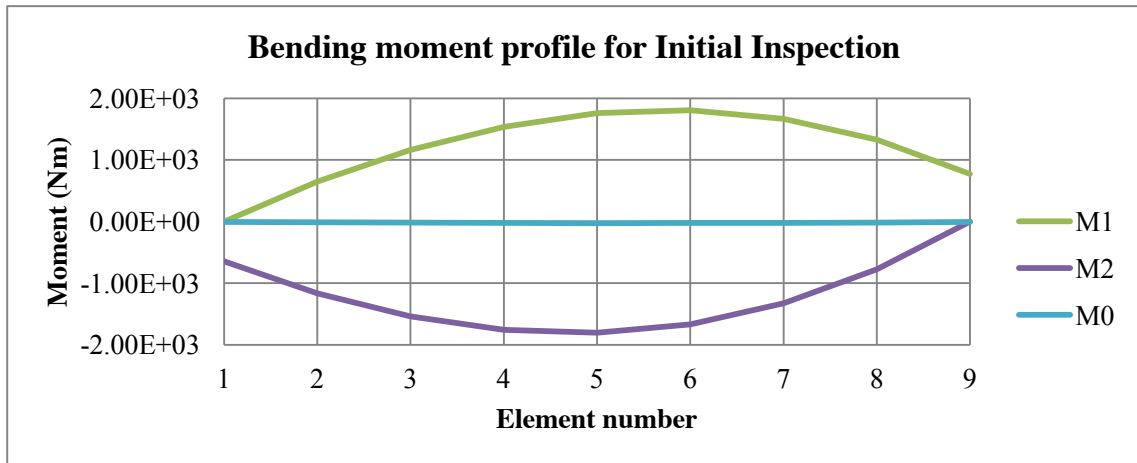


Fig. 4.16 - Stress distribution for beam in analysis 001 for applied displacement  $d = 0.01\text{m}$ .

In order to determine the critical buckling load from this analysis, Fig. 4.17. depicts the variation of the tip of element 9. Although it does reveal a clear point of instability around applied displacement  $d = 0.56\text{m}$ , buckling seem to have already occurred for smaller values of applied displacement.

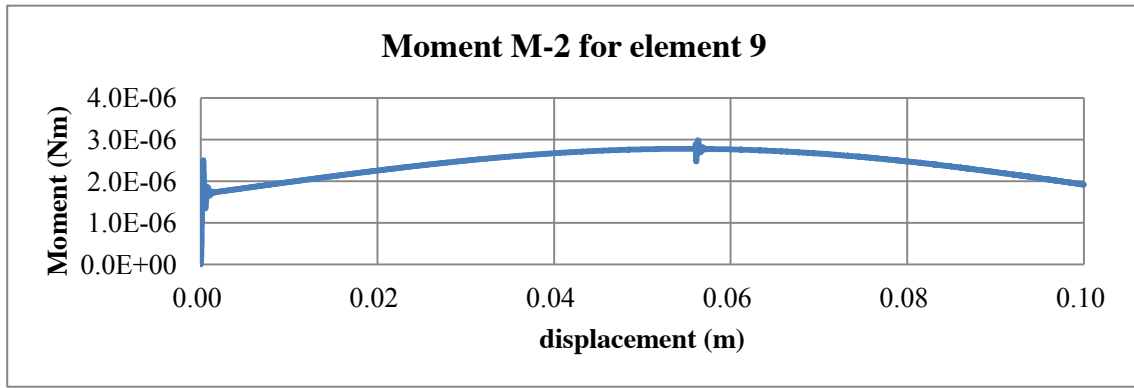


Fig. 4.17 - Time history for the moment at the tip of the beam for initial inspection.

#### 4.3.5 Buckling

Similar analyses are then performed in the same mesh, but this time the applied constraints are varied as shown in Tab. 4.2. In order to search for indicators of buckling, and thus determine buckling values, a sequence of graphs was plotted. These analyses are referred to through the aliases B1 through B4. All these analyses were run with beams with the Total Lagrangian formulation for small rotations (TLsmall).

Tab. 4.2 - Constraints for different analyses.

Analysis	Left tip	Right tip	Critical load (N)	Critical stress (Pa)
B1	Simply supported	Simply supported	2.89E4	9.62E4
B2	Cantilever	Simply supported	5.91E4	1.97E5
B3	Cantilever	Cantilever	1.15E5	3.85E5
B4	Cantilever	Free	7.22E3	2.41E4

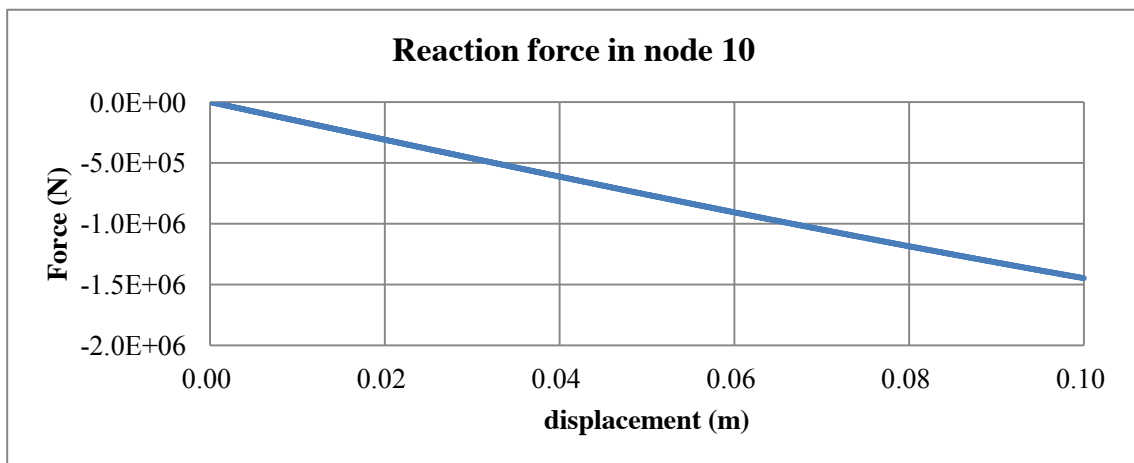


Fig. 4.18 - Reaction force time history for right tip in analysis B1.

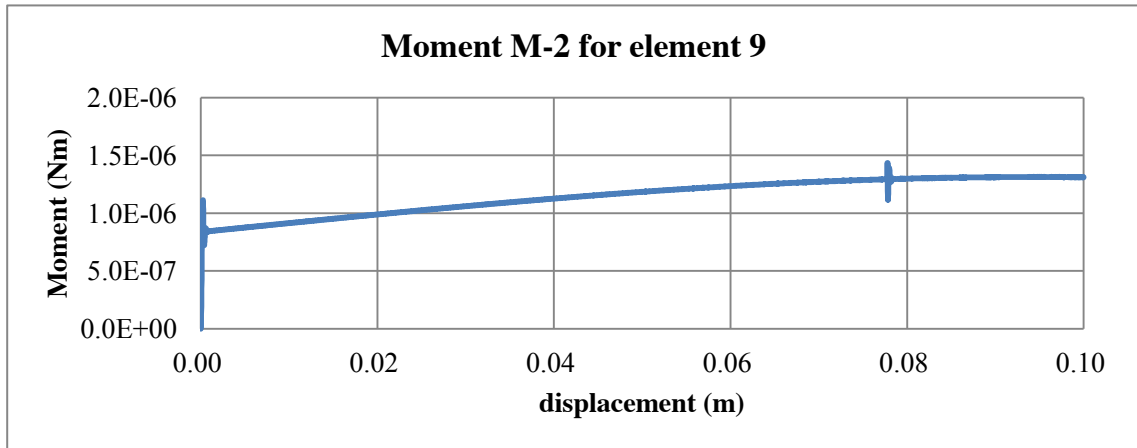


Fig. 4.19 - Bending moment time history for right tip in analysis B1.

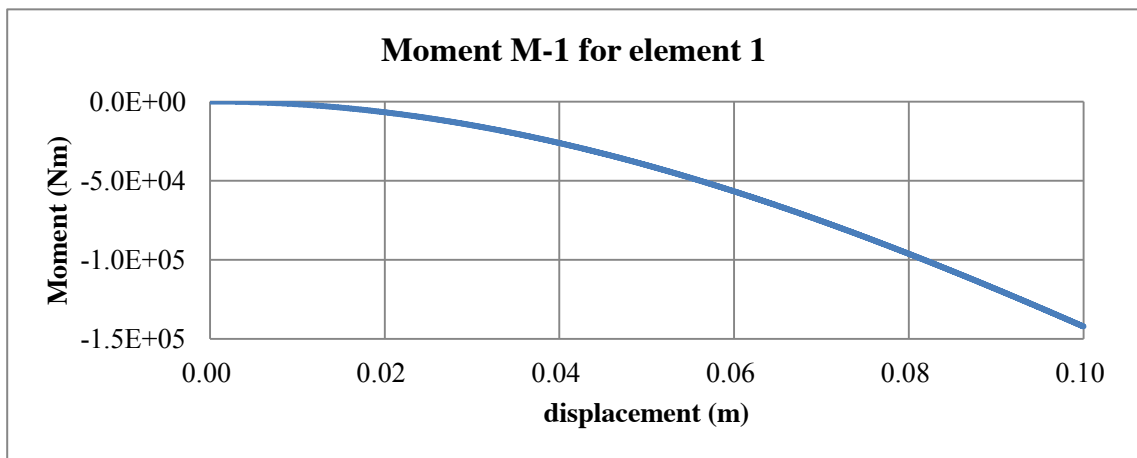


Fig. 4.20 - Bending moment time history for left tip in analysis B2.

The first curve, shown in Fig. 4.18, shows how it isn't possible to derive a buckling value from the nodal reaction force in analysis B1. However, Fig. 4.19 does show two visible instabilities: one around  $d=0.00\text{m}$  and another close to  $d=0.08\text{m}$ . The bending moment time history for the left tip of analysis B2 is shown in Fig. 4.20, and it shows no indicators of buckling.

Also, note that the curves shown in Figs. 4.21 through 4.24 do not show any sharp changes. Therefore, they can't be used to obtain the critical buckling load. As a quick aside, these analyses express a very meaningful preliminary result: the proposed formulations behave as they should under buckling conditions.

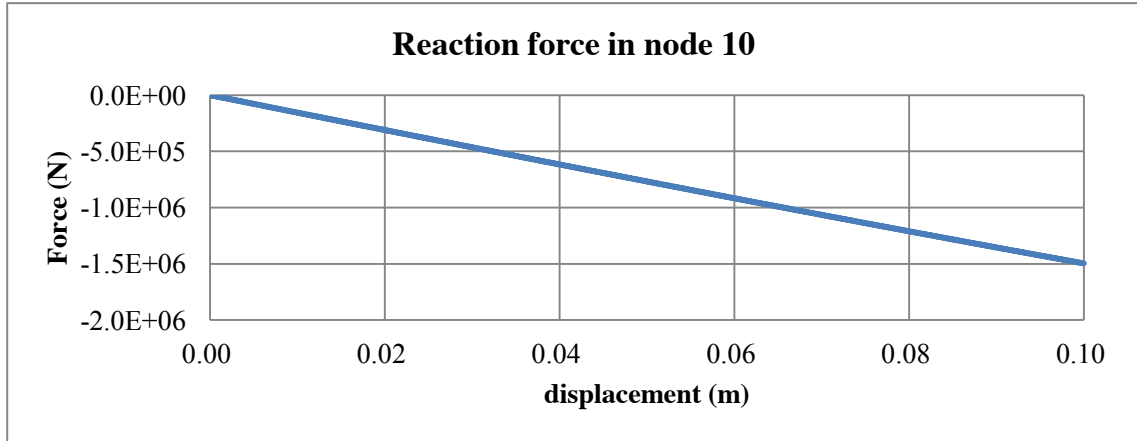


Fig. 4.21 - Reaction force time history for right tip in analysis B2.

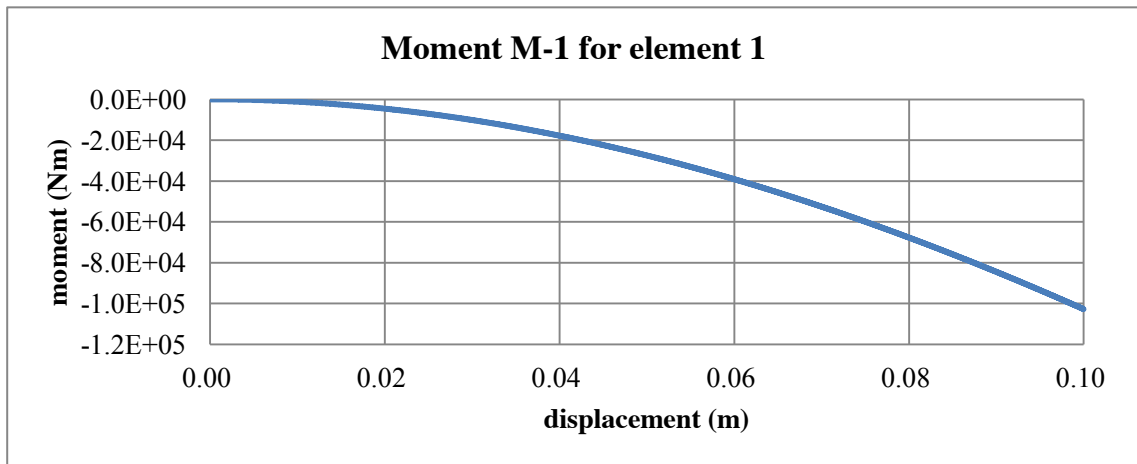


Fig. 4.22 - Bending moment time history for left tip in analysis B3.

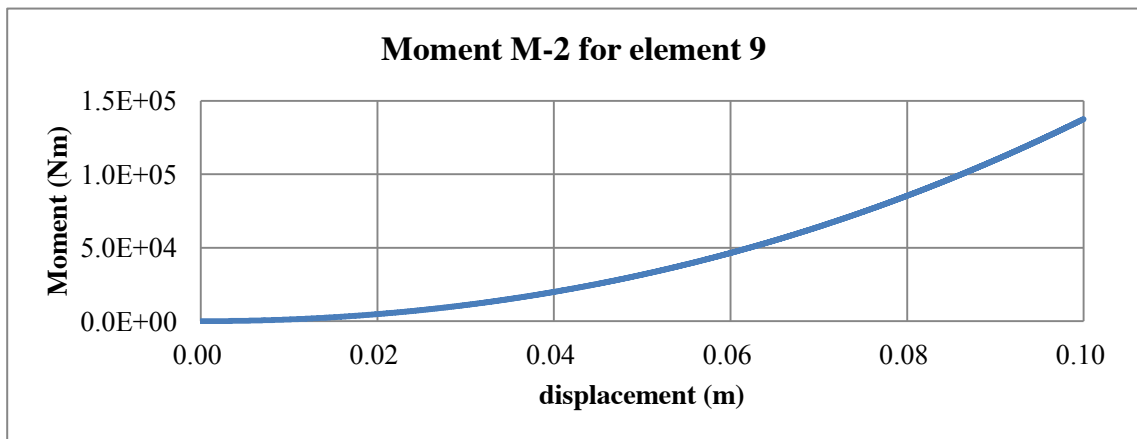


Fig. 4.23 - Bending moment time history for right tip in analysis B3.



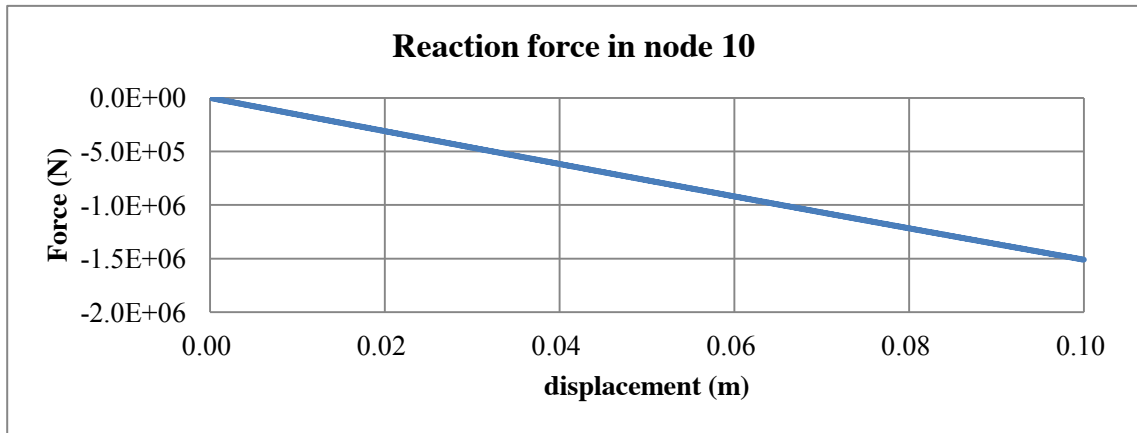


Fig. 4.24 - Reaction force time history for right tip in analysis B3.

Analysis B4 is of paramount importance because it solidifies an understanding that is merely hinted at by previous analyses. This is the understanding that, although the proposed formulations are well-behaved under buckling, clear critical buckling load values can't be obtained.

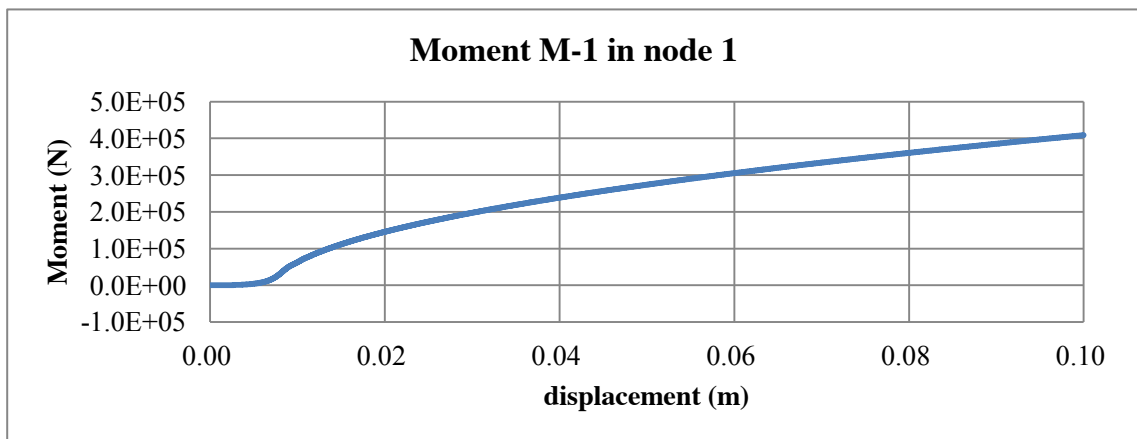


Fig. 4.25 - Bending moment time history for left tip in analysis B4.

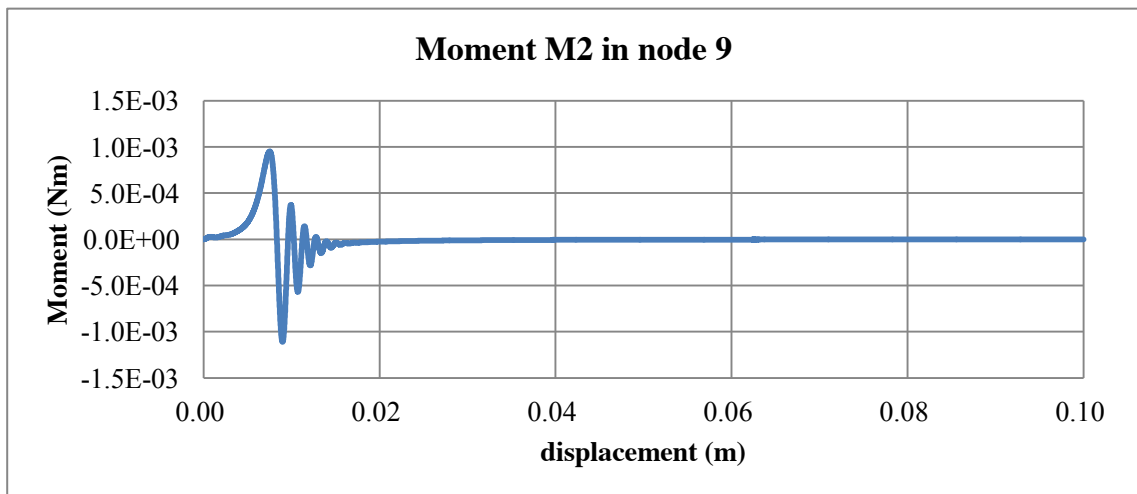


Fig. 4.26 - Bending moment time history for right tip in analysis B4.

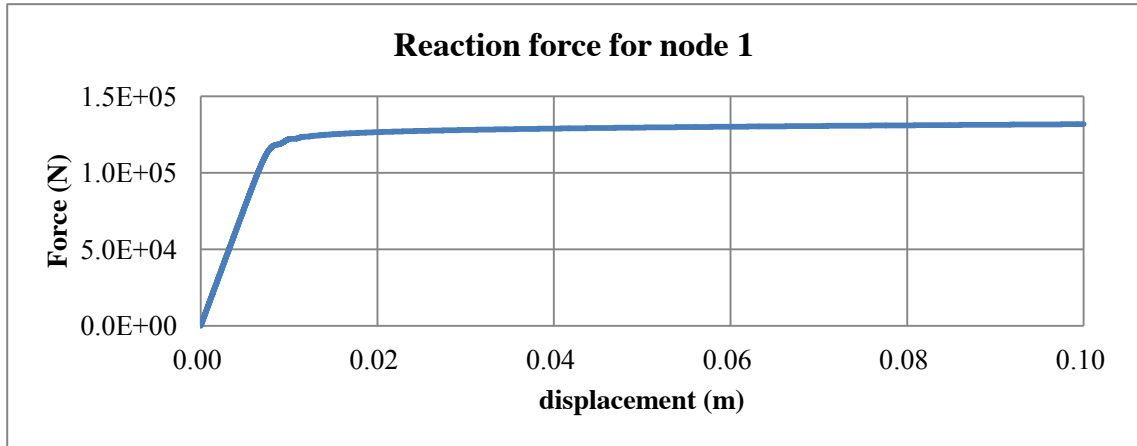


Fig. 4.27 - Reaction force time history for left tip in analysis B4.

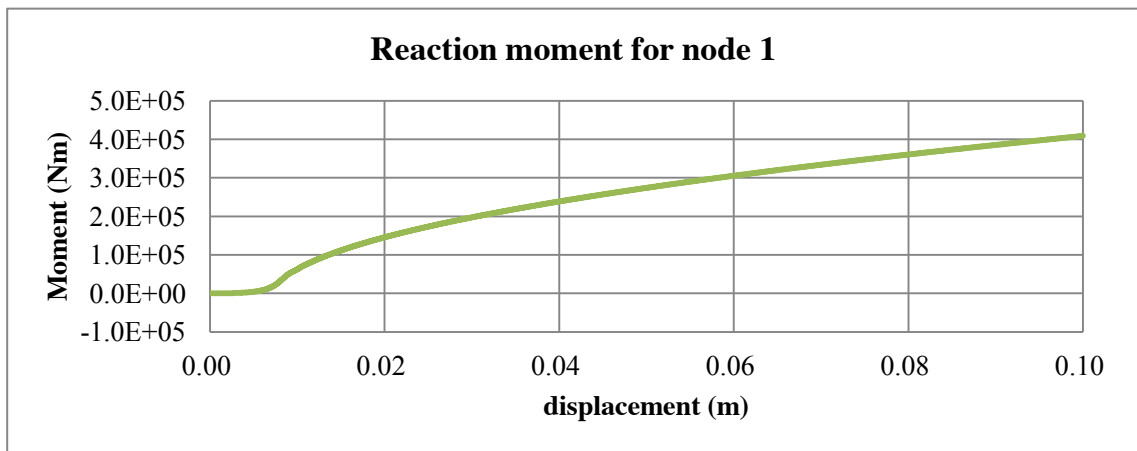


Fig. 4.28 - Reaction bending moment time history for left tip in analysis B4.

Note how Figs. 4.25 and 4.28 do present curves with somewhat sharp changes around  $d=0.01\text{m}$ . This instability is perceived from within an element as shown in Fig. 4.26, and the corresponding critical buckling load value of approximately  $1.25 \times 10^5\text{N}$  can be extracted visually from Fig. 4.27. This value is comparable to the analytical Euler buckling value of  $3.85 \times 10^5\text{N}$ .

#### 4.4 Refined Inspection

In this refined analysis, the insights obtained from the initial analysis are employed in order to fine-tune simulation parameters so that better results can be obtained. The timeframe in which the displacement applied to the tip of the beam is now stretched from 10s to 100s, in order to prevent dynamic effects from affecting results. A simple procedure to obtain the critical buckling load is described with the beam and mesh utilized in the initial analysis, and then applied to these analyses.

#### 4.4.1 Determination of critical load

The beam adopted for the initial simulation and its mesh were modified. The procedure to obtain the critical buckling load uses the beam whose properties are described in Fig. 4.29 and Tab. 4.3, and the chosen mesh is shown in Fig. 4.30. This beam is simply supported.

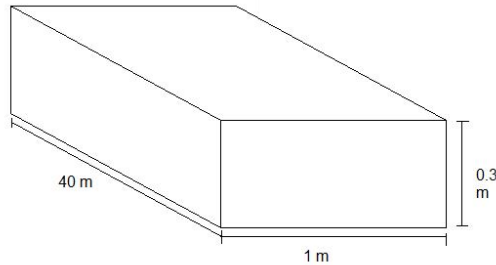


Fig. 4.29 - Geometry of simply supported beam used for procedure description.

Tab. 4.3 - Geometric and material properties chosen for procedure description.

Property	Value
E (GPa)	2.09
$\nu$	0.3
G (MPa)	800
A (m <sup>2</sup> )	0.3
I (10 <sup>-4</sup> m <sup>4</sup> )	22.5

The simulation then is executed by applying a displacement of  $d = 0.03\text{m}$  to the left tip of the mesh (node 1). Then, the plot of the curve between the moment at the tip of the beam and the stress in the adjacent element is as shown in Figs. 4.31 and 4.32. These two curves show each four areas in which instability is clearly occurring. Figs. 4.34 through 4.36 allow for a closer look at these instabilities. If displacement continues to be applied, all elements in the beam grow unstable and then the simulation usually diverges. This behavior can be observed in Fig. 4.33, which depicts a simulation for which the maximum applied displacement is  $d = 0.05\text{m}$ . Also, it is important to notice that Figs. 4.31 and 4.32 do not contain all points of data available, because even the simulation with a maximum displacement of  $d = 0.03\text{m}$  reaches the region of numerical instability depicted in Fig. 4.33. Figs. 4.31 and 4.32 were plotted so that the fourth area of instability corresponds to the instability observed in Fig. 4.33.

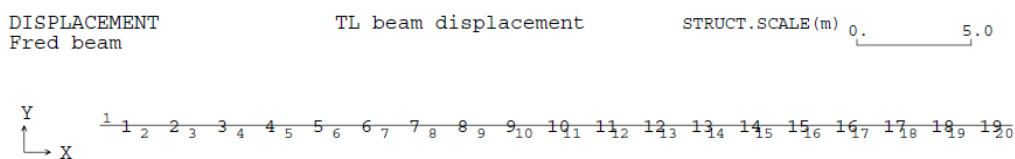


Fig. 4.30 - Mesh utilized for refined analyses.

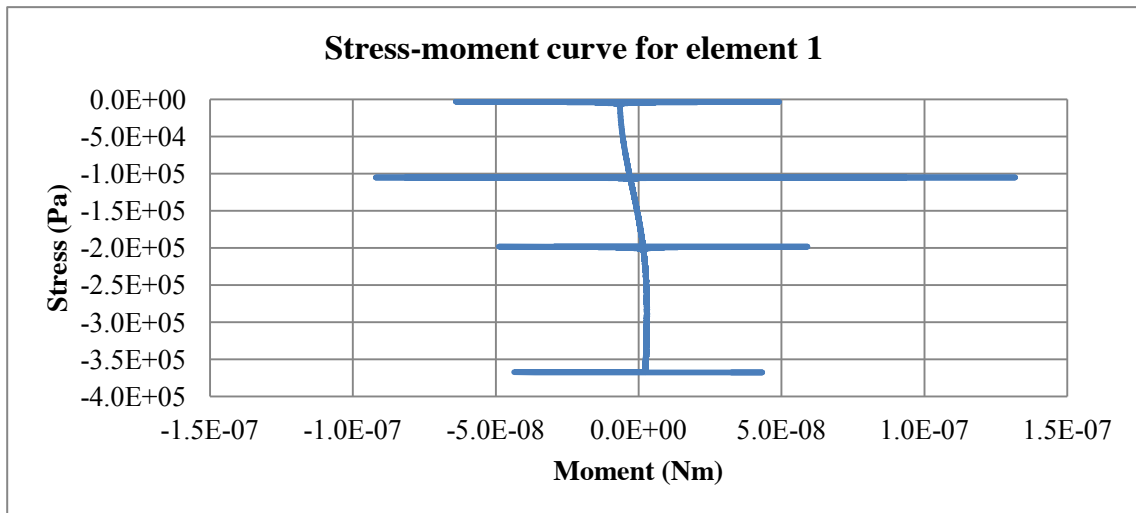


Fig. 4.31 - Stress-moment curve for element 1 in buckling refined analysis.

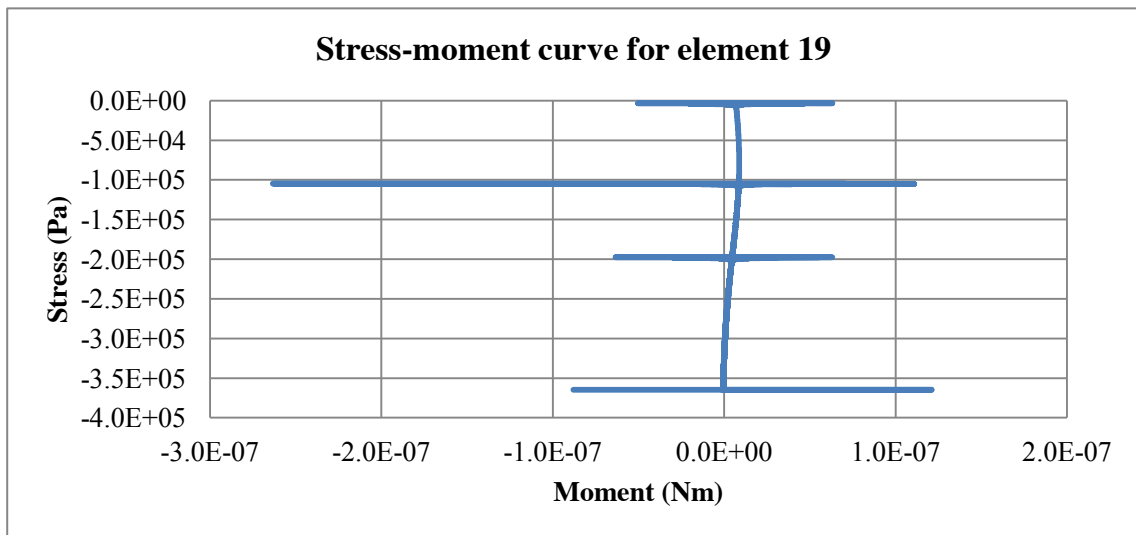


Fig. 4.32 - Stress-moment curve for element 19 in buckling refined analysis.

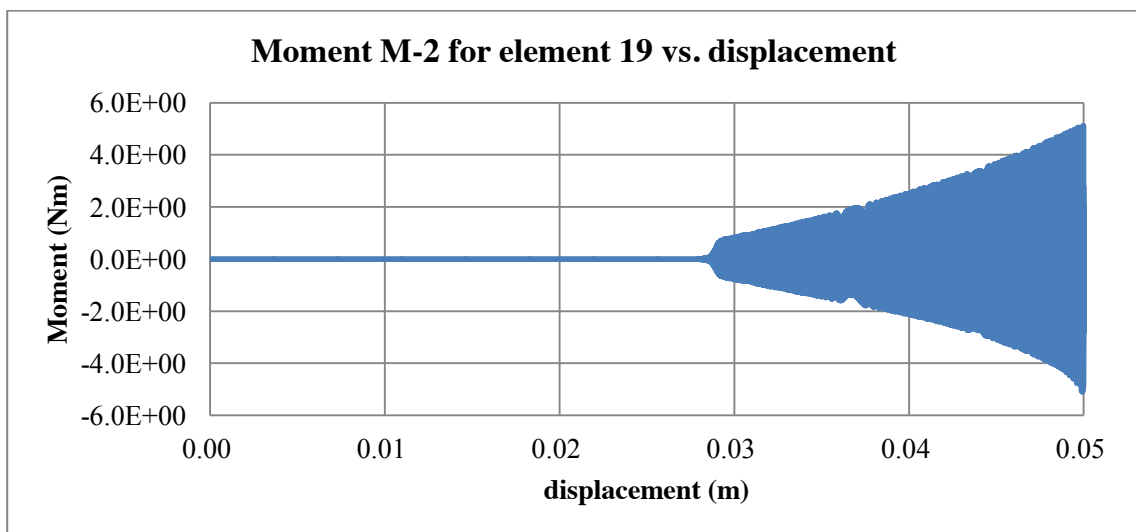


Fig. 4.33 - Bending moment time history for element 19 in buckling refined analysis.

These instabilities cannot be found in different beams whose tip rotation has been constrained. For this reason, all beams analyzed henceforth are simply supported.

Now, a closer look is taken at the first three instabilities found in Figs. 4.34 through 4.36. Note that the first instability was actually hiding another, smaller instability, which will be referred to as instability zero. From these curves, the critical load for each instability might be obtained by multiplying the stress right at the beginning of the instability by the area of the beam. The resulting values are presented in Tab. 4.4. Note that the second instability occurs very close to the value determined by Euler's analytical formula. This will be regarded as the critical buckling value determined by this procedure: the instability load which is closest to the analytical value.

Tab. 4.4 - Critical load values for each instability, and its correspondent stress.

Method	Critical stress (Pa)	Critical load (N)
Instability zero	-2.34E2	-7.02E1
First	-3.32E3	-9.96E2
Second	-1.05E5	-3.15E4
Third	-1.98E5	-5.94E4
Euler formula	9.62E4	2.89E4

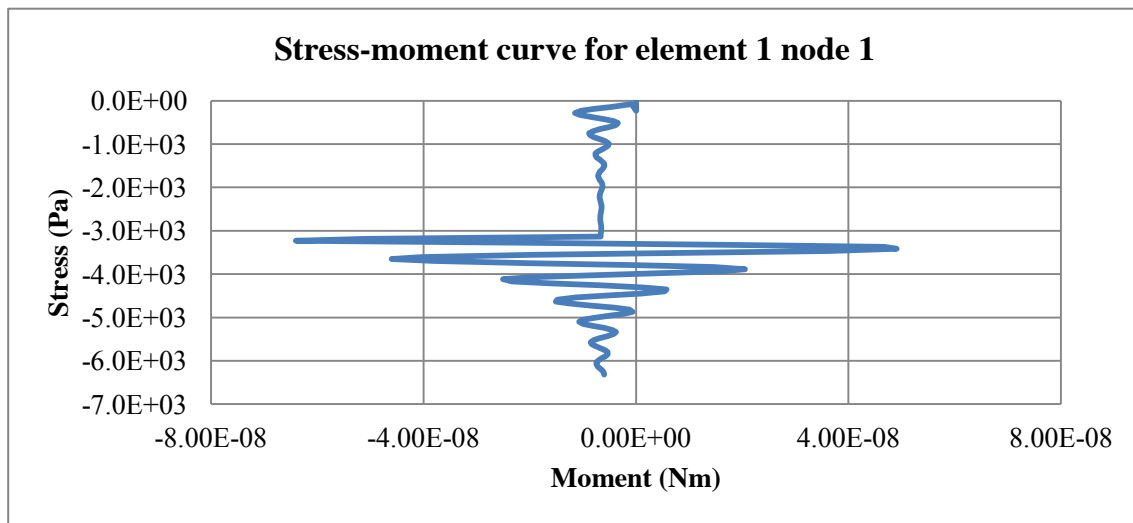


Fig. 4.34 - Stress-moment curve for element 1 in refined analysis.

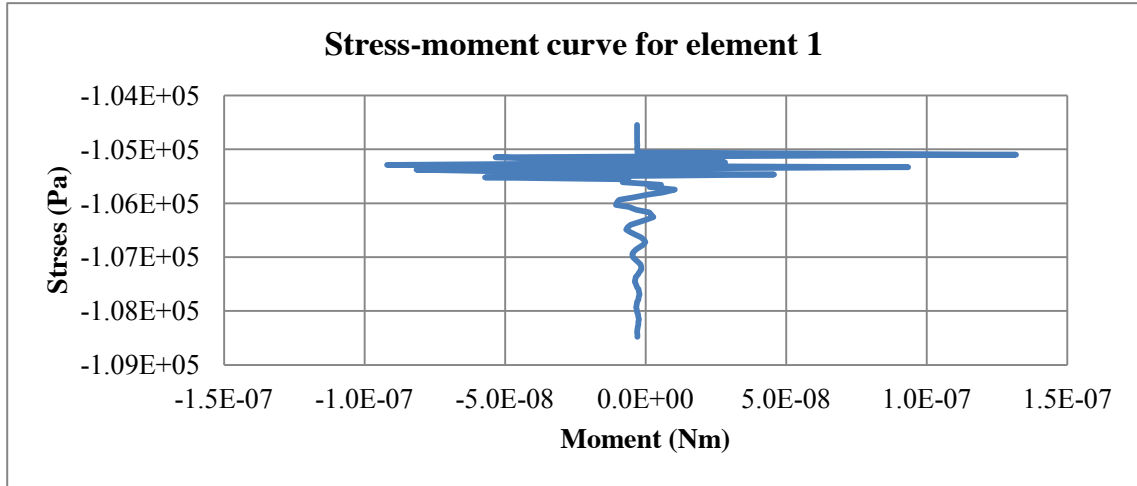


Fig. 4.35 - Stress-moment curve for element 1 in refined analysis.

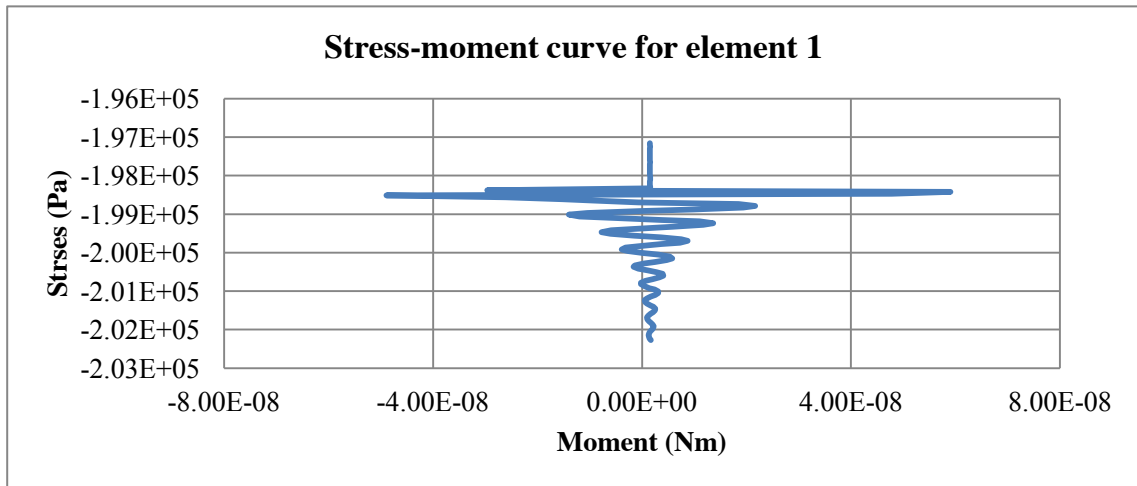


Fig. 4.36 - Stress-moment curve for element 1 in refined analysis.

#### 4.4.2 Batch of analyses

Next, several analyses were performed using the procedure previously outlined, in order to inspect how valid are the results it produces. The analyses differ from each other as shown in Tab. 4.5 and Fig. 4.37. For section S1, the moment of inertia is  $I_1 = 2.25 \times 10^{-3} \text{m}^4$  and the area is  $A_2 = 0.3 \text{m}^2$ , whereas the values for section S2 are  $I_2 = 8.333 \times 10^{-5} \text{m}^4$  and  $A_2 = 0.1 \text{m}^2$ . The obtained results were organized and are presented in the next section.

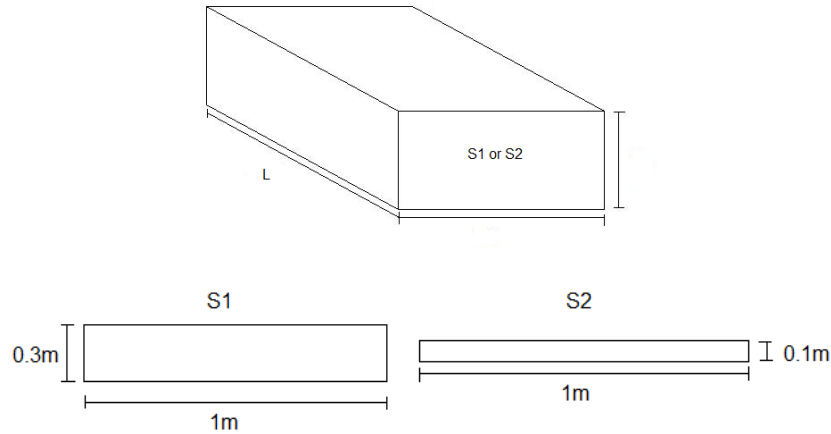


Fig. 4.37 - Geometry of beams used in refined analysis.

Tab. 4.5 - Description of batch of analyses ran within the context of this work's refined analysis.

Alias	L (m)	Section	Formulation
B01	40	S1	TLs
B02	40	S1	TLf
B03	40	S2	TLs
B04	40	S2	TLf
B05	80	S1	TLs
B06	80	S1	TLf
B07	80	S2	TLs
B08	80	S2	TLf

#### 4.4.3 Results and comparison

Figs. 4.38 through 4.45 exhibit the stress-moment curves obtained for each of the simulations described in the previous section, and Tab. 4.6 contains the value for each observed instability, the chosen critical load and Euler's analytical value for comparison purposes. Note that the analyses that use the Total Lagrangian for finite rotations present curves whose shape is qualitatively different, so that there is no "zero instability" for these analyses.

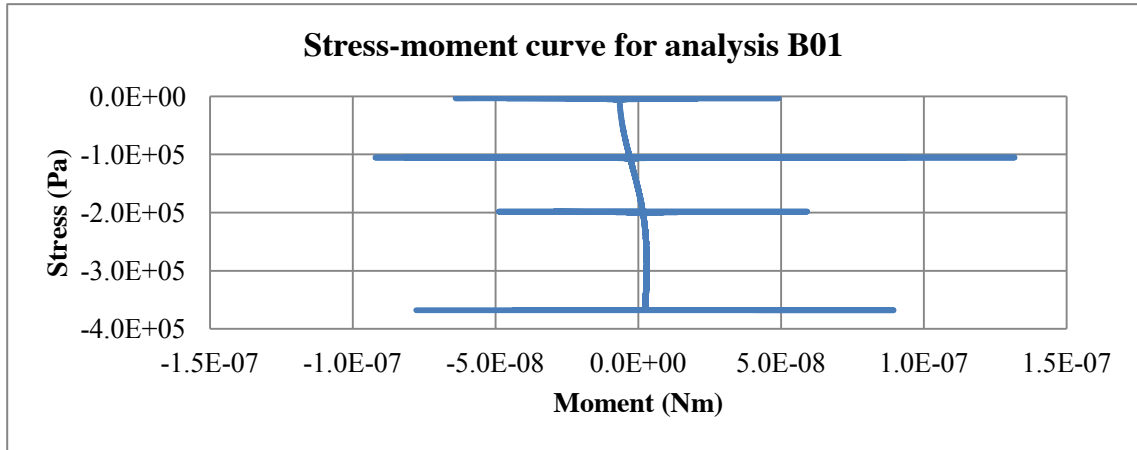


Fig. 4.38 - Stress-moment curve for B01 in refined analysis.

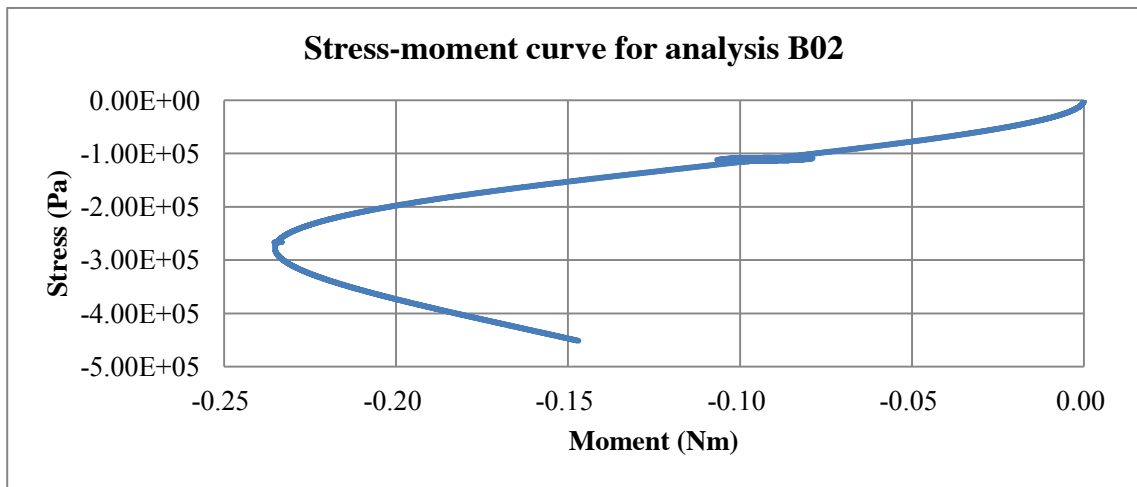


Fig. 4.39 - Stress-moment curve for B02 in refined analysis.

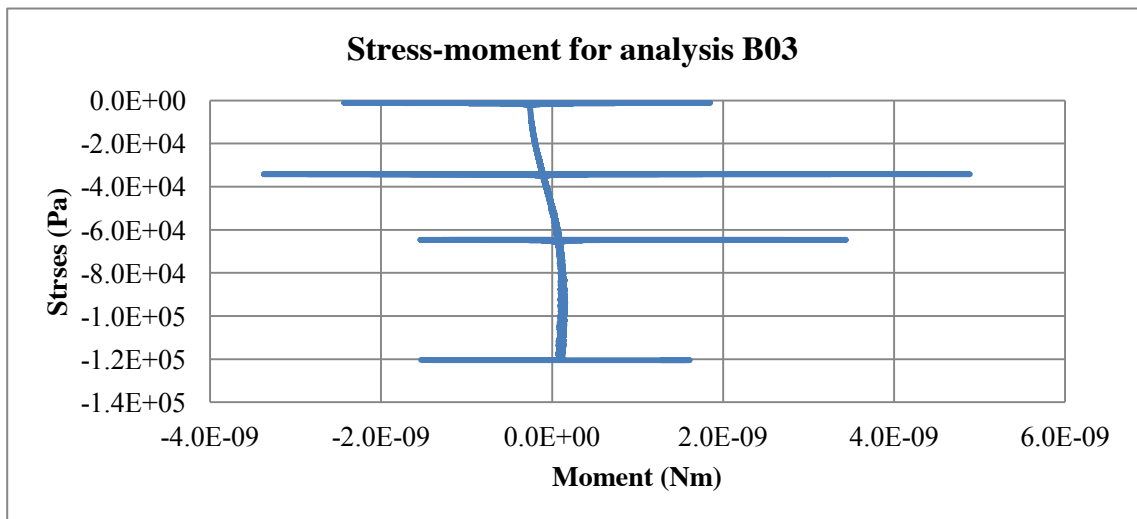


Fig. 4.40 - Stress-moment curve for B03 in refined analysis.



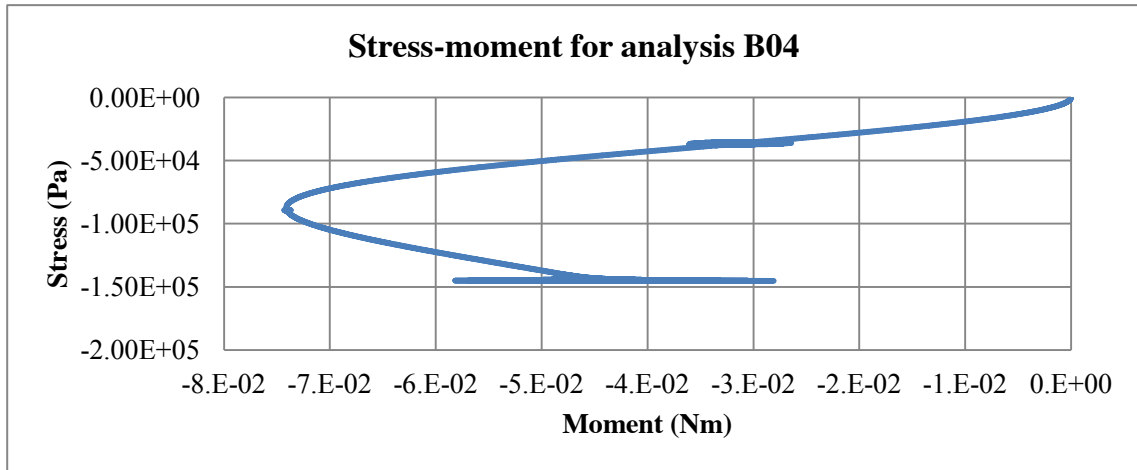


Fig. 4.41 - Stress-moment curve for B04 in refined analysis.

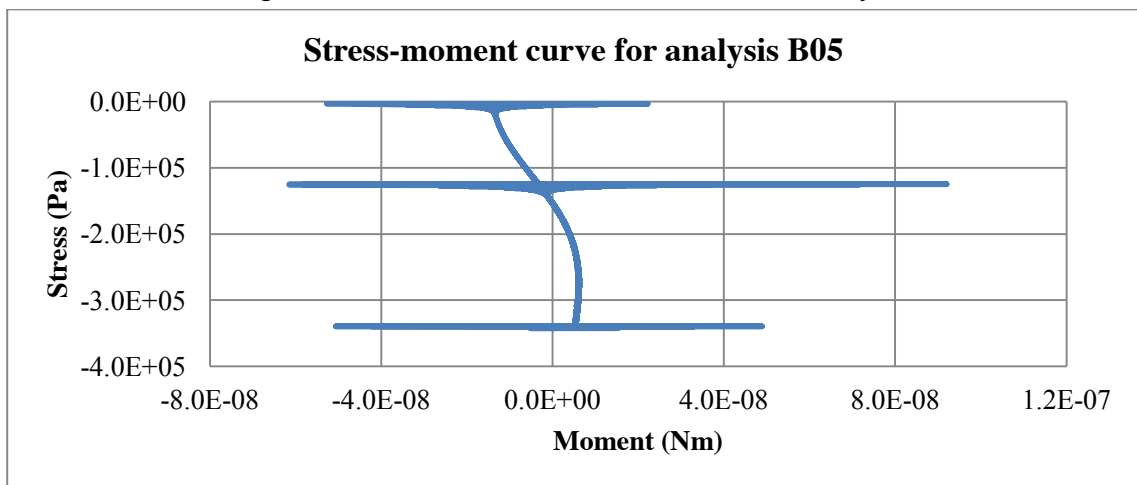


Fig. 4.42 - Stress-moment curve for B05 in refined analysis.

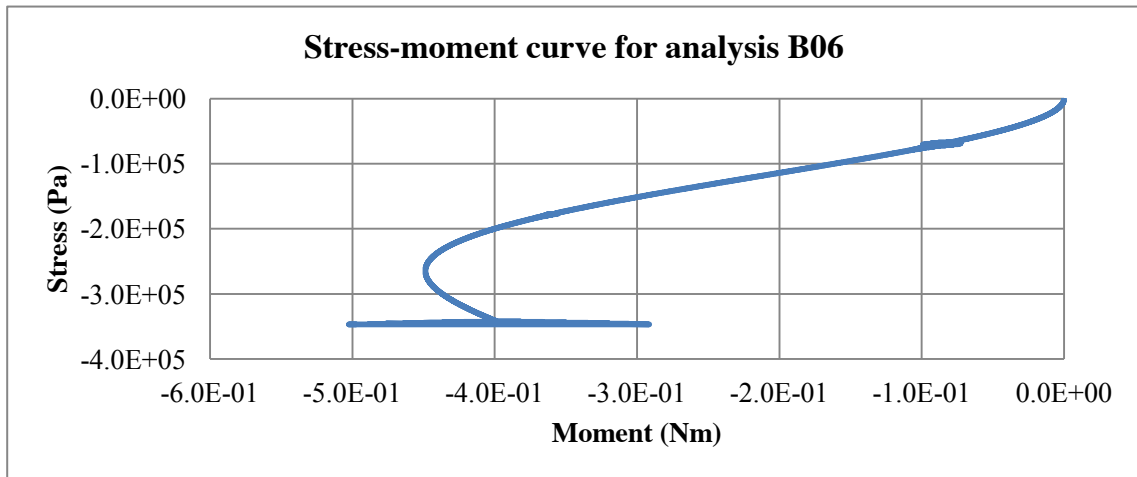


Fig. 4.43 - Stress-moment curve for B06 in refined analysis.

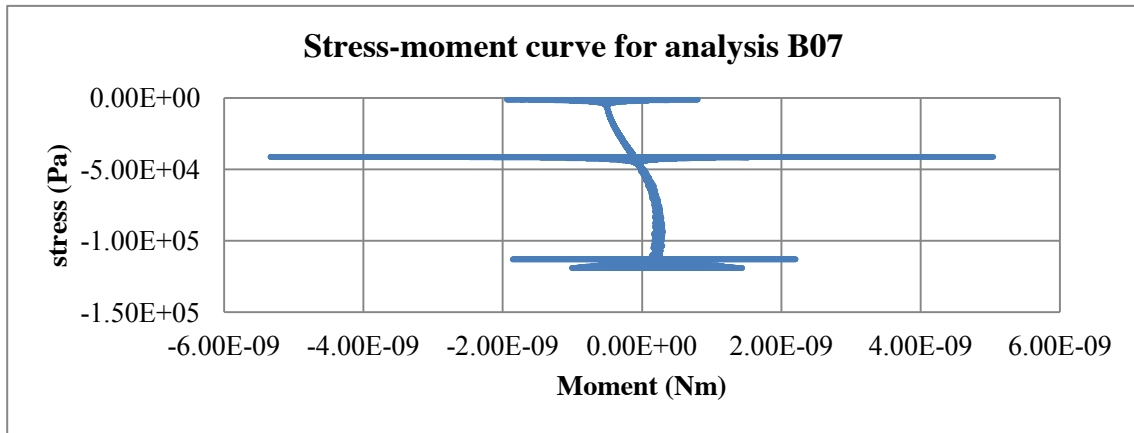


Fig. 4.44 - Stress-moment curve for B07 in refined analysis.

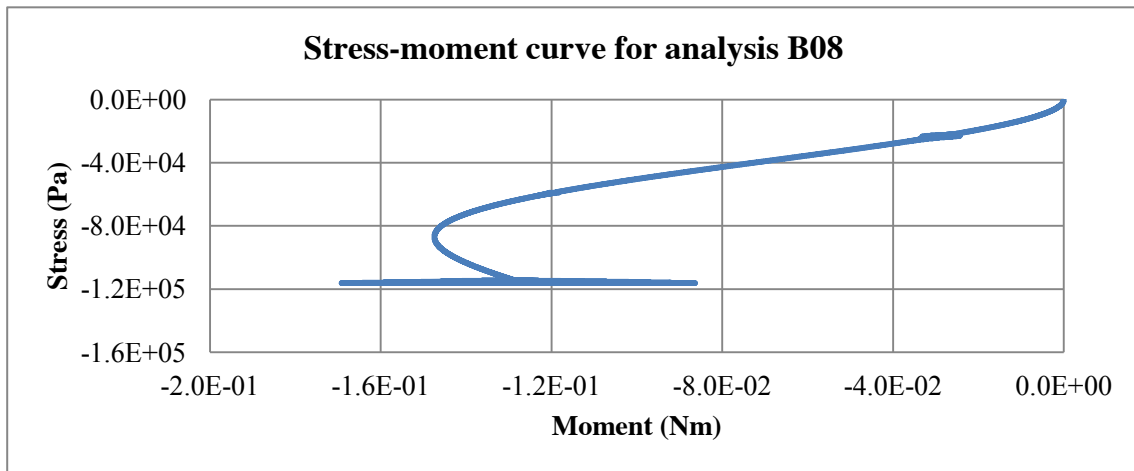


Fig. 4.45 - Stress-moment curve for B08 in refined analysis.

Tab. 4.6 - Critical buckling load for refined analyses.

Alias	Instabilities (Pa)	Euler stress (Pa)	Chosen value (Pa)
B01	1	-3.14E3	9.62E4
	2	-1.05E5	1.05E5
	3	-1.98E5	
B02	1	-1.08E5	9.62E4
	2	-2.66E5	1.08E5
B03	1	-1.05E3	1.07E4
	2	-3.41E4	3.41E4
	3	-6.46E4	
B04	1	-3.54E4	1.07E4
	2	-8.90E4	3.54E4
B05		-1.25E5	2.41E4
B06		-6.64E4	2.41E4
B07		-4.13E4	2.67E3
B08		-2.20E4	2.67E3

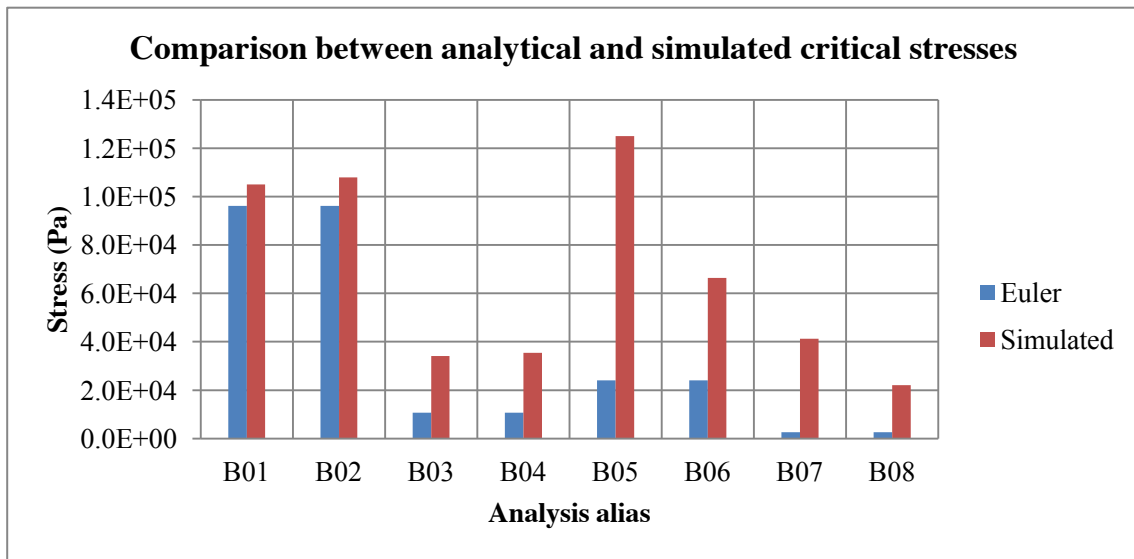


Fig. 4.46 - Visual comparison of values presented in Tab. 4.6.

The results from Tab. 4.6 were compared visually using Fig. 4.46.

#### 4.5 Tentative conclusions and critique

The initial analysis indicates that the utilization of plane elements to construe a beam is possible, and numerically stable. That analysis exhibits a clear bifurcation, that can be detected on a element-by-element basis as well as by inspecting the properties of elements as a group. The critical load found through this method is in the same order of magnitude as the values obtained using Euler's analytical formula.

The initial beam buckling analysis that adopts the proposed formulations yields various insights into their behavior. Linear beam elements that use the Total Lagrangian (either TLsmall or TLfinite) formulation are more prone to numerical instability than its linear isoparametric (linear-isoparametric) simpler counterparts. This is to be expected, since a new tangent stiffness matrix has to be calculated for every new iteration. Therefore, simulations that do not require large displacements and/or finite rotations in their beams might suffer unnecessary convergence difficulties by adopting the herein proposed formulations. For cases where it is possible, the simplest formulation must be utilized as long as it does not sacrifice precision in the results.

## 5 Assumptions

As an aside, this work presented the unexpected opportunity to evaluate one of the premises that is brought up during the formulation of geometrically linear beam elements: namely, that *its cross-sections do not warp*.

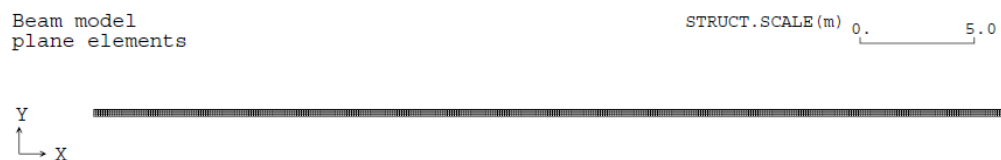
Material properties used in all of this chapter's analyses are shown in Tab. 5.1.

Tab. 5.1 - Geometric and material properties chosen for buckling analysis.

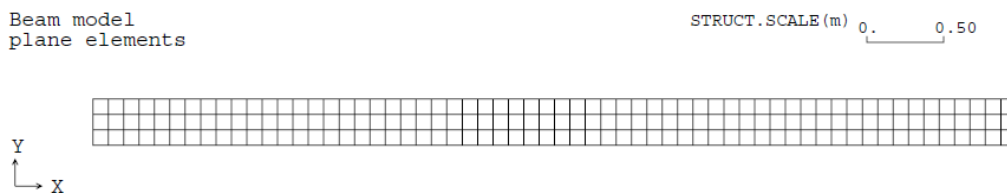
Property	Value
E (GPa)	2.09
$\nu$	0.3
G (MPa)	800
A (m <sup>2</sup> )	0.3
I (10 <sup>-4</sup> m <sup>4</sup> )	22.5

### 5.1 Coarse analysis

In order to assess this assumption, it is desirable that the subjective notion of "warping" be translated into a quantifiable value that can be measured. To do that, a mesh of square plane elements was created and its material properties were made to match that of the beam (previously used in chapter 3). These elements were formulated using the Total Lagrangian approach, and thus are appropriate for large displacement simulations. The created mesh can be seen in Fig. 5.1, and the analysis of this mesh is referred to as W-1.



(a)



(b)

Fig. 5.1 - Fig. - Undeformed mesh (a) and mesh detail (b) for W-1 analysis.

As before, this mesh had its left side constrained and its right side submitted to a moment. This force was

applied linearly with time for better convergence. The maximum value for the moment was  $M = 9 \times 10^7 \text{ Nm}$ . The resulting deformed configuration for analysis W-1 is shown in Figs. 5.2.

A reasonable, quantifiable measure of the linearity of the four points which comprise each cross-section of this numerical analysis can be obtained by the average of the areas formed by the two triangles whose vertices are the bottom and top three points of any given cross-section. This arrangement is shown in Fig. 5.3. This way of calculating an index value has the advantage that it can be expanded to accommodate a variable number nodes or elements in each cross-section, a feature that will come in handy later in this chapter.

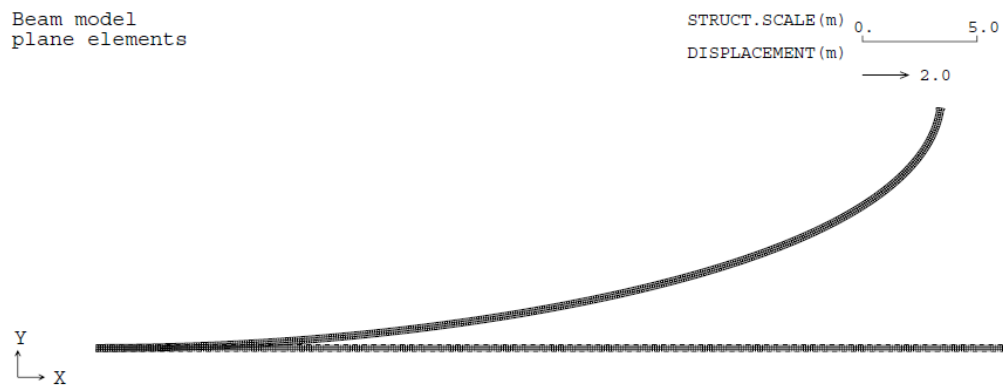


Fig. 5.2 - Deformed mesh for analysis W-1

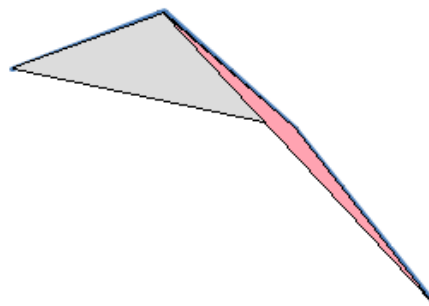


Fig. 5.3 - Calculation of index representing "warping" through areas of adjacent three-node groups.

Note that the areas may overlap, and they usually do. This points to the fact that the value obtained for this index should not be thought of as an absolute value, but rather as an indicator of the degree of "warping" of any given cross-section. Thus, the sum of the area of these two triangles will be referred to as a-index in this section. The resulting area for the two triangles and the a-index for each cross-section is presented in Figs. 5.4 and 5.5.

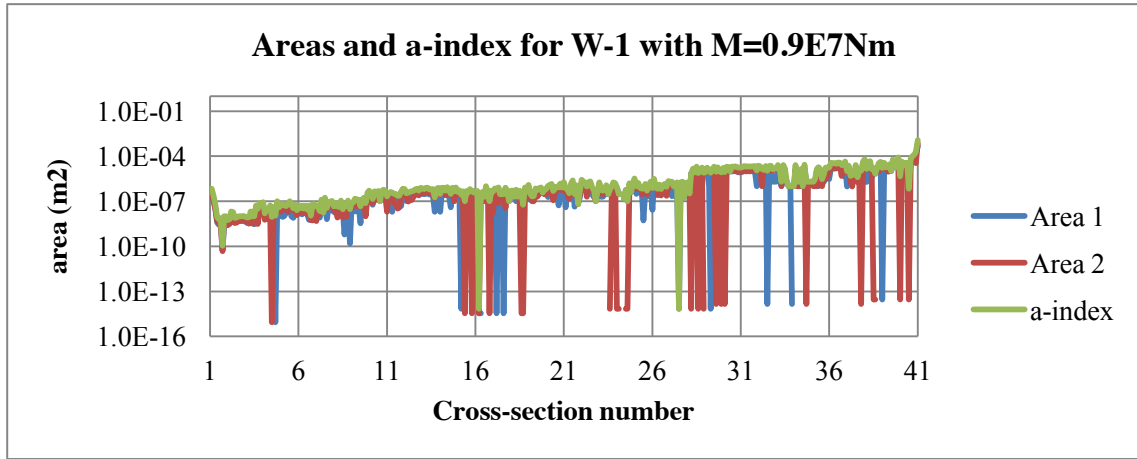


Fig. 5.4 - Profile of a-index at each cross-section for analysis W-1.

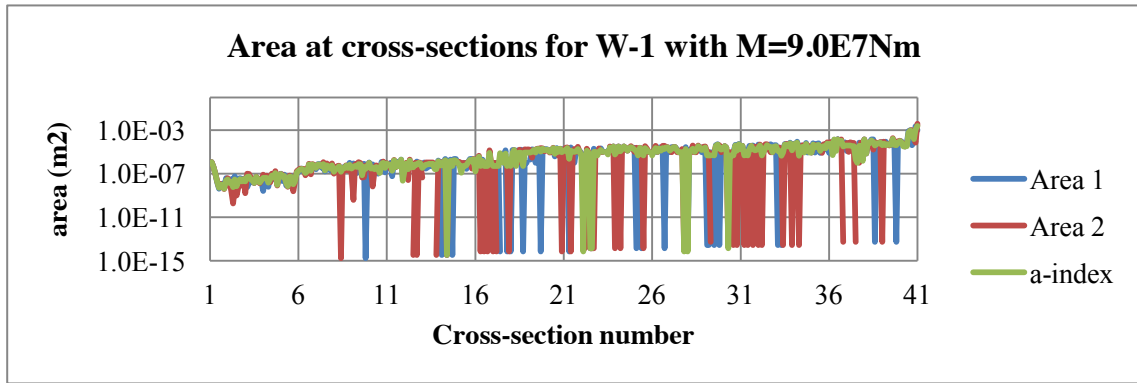


Fig. 5.5 - Profile of a-index at each cross-section for analysis W-1.

Figs. 5.4 and 5.5 clarify that, for this particular analysis, the cross-section that suffers the effects of warping more intensely is the one in which the moment is applied: the tip of this beam. The cross-sections for the tip cross-section (number 41) corresponding to the previously shown profiles are shown in Figs. 5.6 and 5.7.

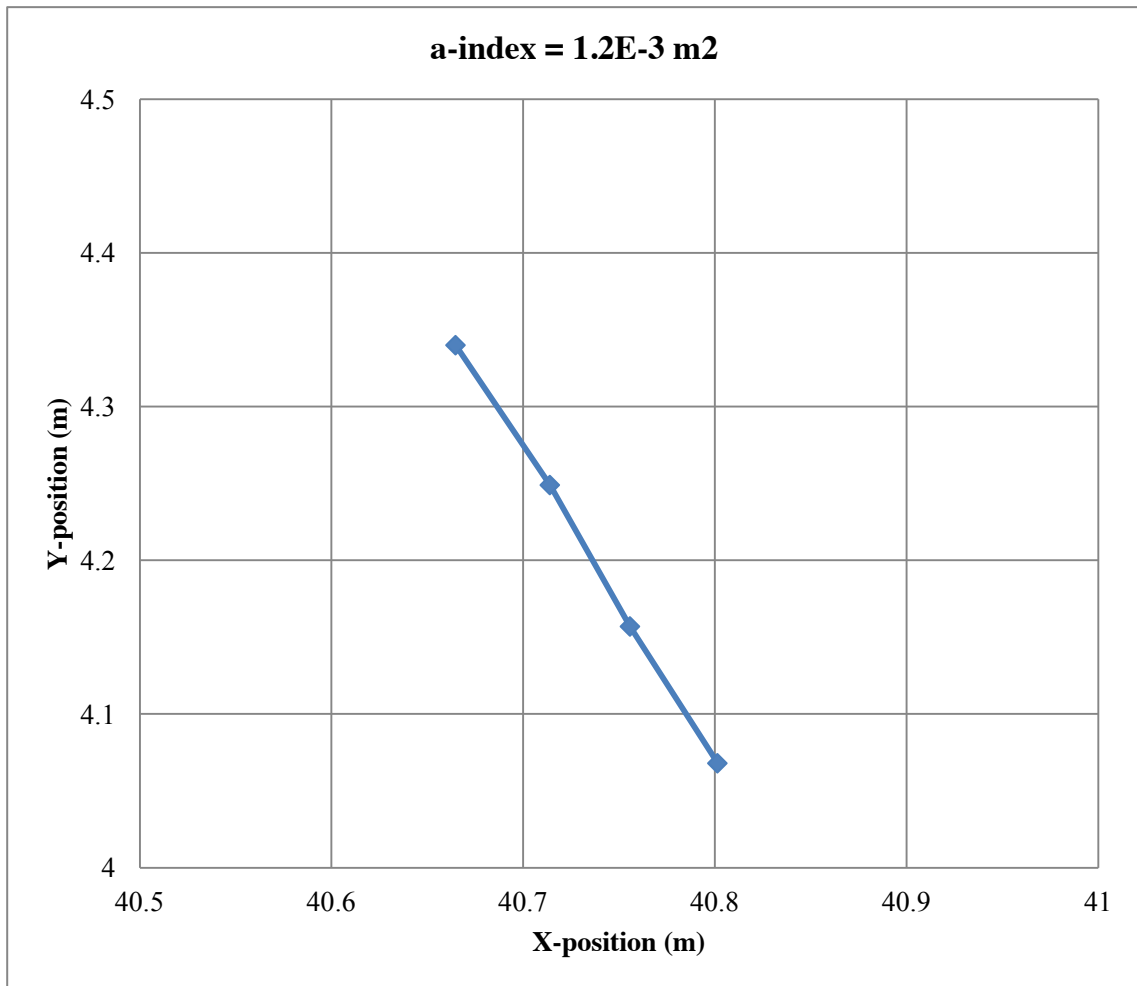


Fig. 5.6 - Visualization of tip cross-section 41 for  $M = 0.9 \times 10^7 \text{Nm}$  in analysis W-1.

Interestingly enough, visual inspection of these two figures seem to indicate that even the large values of a-index - larger than  $2.0\text{e-}3\text{m}^2$  - do not correspond to a lot of warping in the cross-section (see Fig. 5.7).

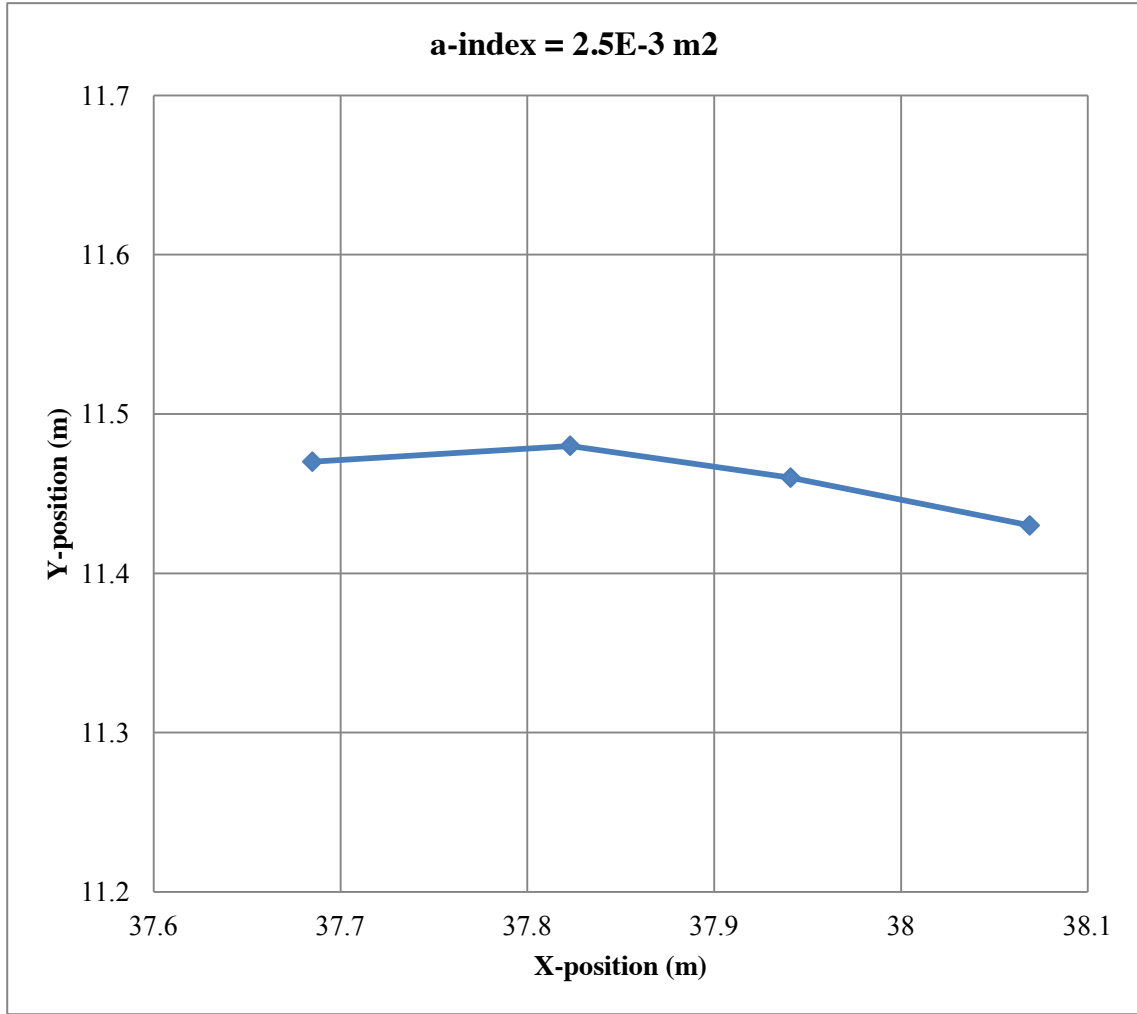


Fig. 5.7 - Visualization of tip cross-section 41 for  $M = 9.0 \times 10^7 \text{Nm}$  in analysis W-1.

## 5.2 Refined analysis

In order to deepen this analysis, two more meshes were composed. These two meshes do not resemble the mesh previously used in this chapter, and thus cannot be directly compared. Also, note that a-index is not *a priori* comparable between analysis as it is now. These two meshes were assigned the same material properties utilized in this chapter up to now, but they are thicker and shorter, being thus more stiff. These meshes are shown in Fig. 5.8 and 5.9, and a detailed view of these meshes is shown in Fig. 5.10.



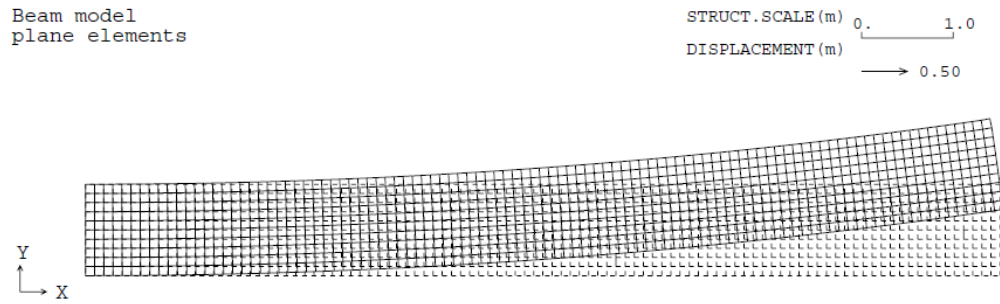


Fig. 5.8 - Deformed mesh for analysis W-2

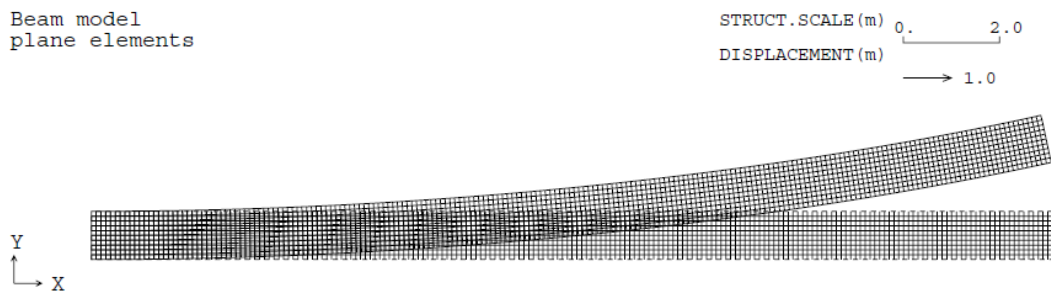


Fig. 5.9 - Deformed mesh for analysis W-3

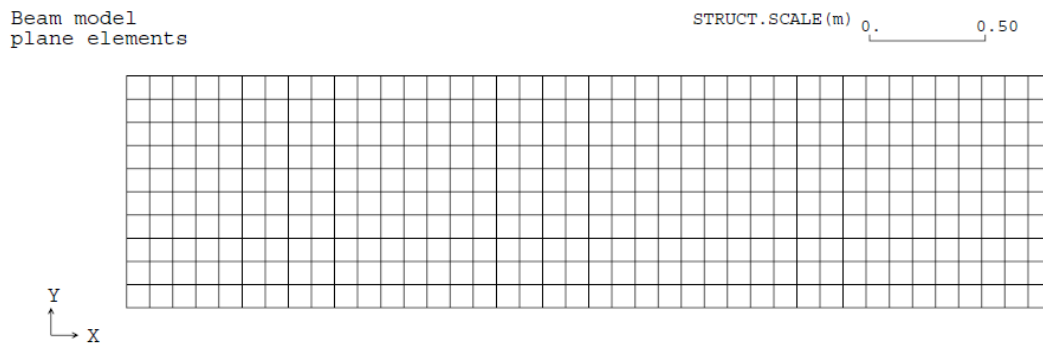


Fig. 5.10 - Mesh tip detail for analysis W-2 and W-3.

The results of analysis W-2 and W-3 were then processed so as to obtain the a-index of each cross-section located in-between elements. The a-index curves for analysis W-2 and W-3 are shown in Fig. 5.11 and 5.12. The cross-sections of analysis W-2 and W-3 possess the exact same number of nodes. Thus, it is safe to assume that a-index values can be compared.

With this in mind, it is possible to choose an arbitrary *limit value* for a-indexes for the class of beams simulated in W-2 and W-3. A tentative definition of this class of beams would be: "all cantilever beams with square

meshes of plane elements formulated through the Total Lagrangian method whose cross-sections are comprised of 11 nodes connected by 10 elements that utilize material properties shown in Tab. 5.1". This class definition may later be expanded to allow for more flexible manipulation and comparison of a-indexes. For now, the purpose of this definition is to assess *qualitatively* the assumption that cross-sections do not warp in a beam.

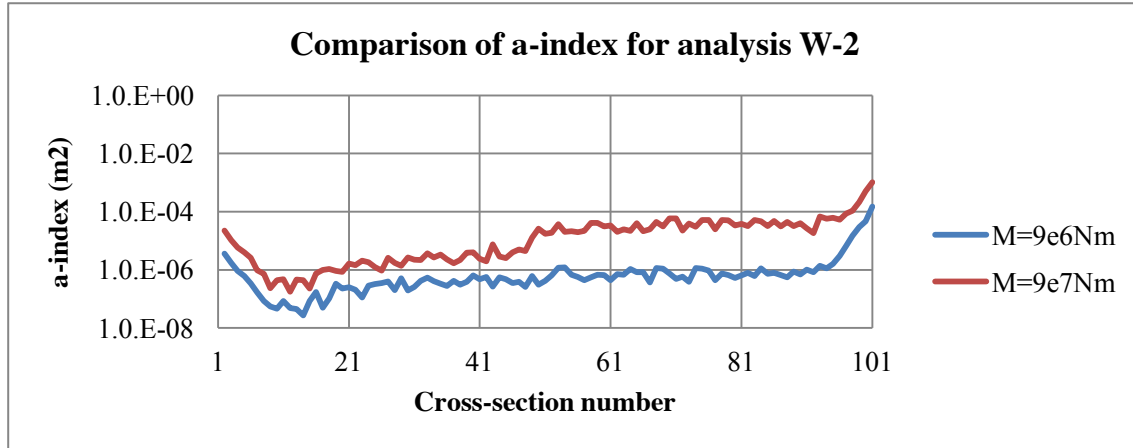


Fig. 5.11 - Comparison of a-index values for analysis W-2 at each cross-section for two arbitrarily chosen values of applied moment.

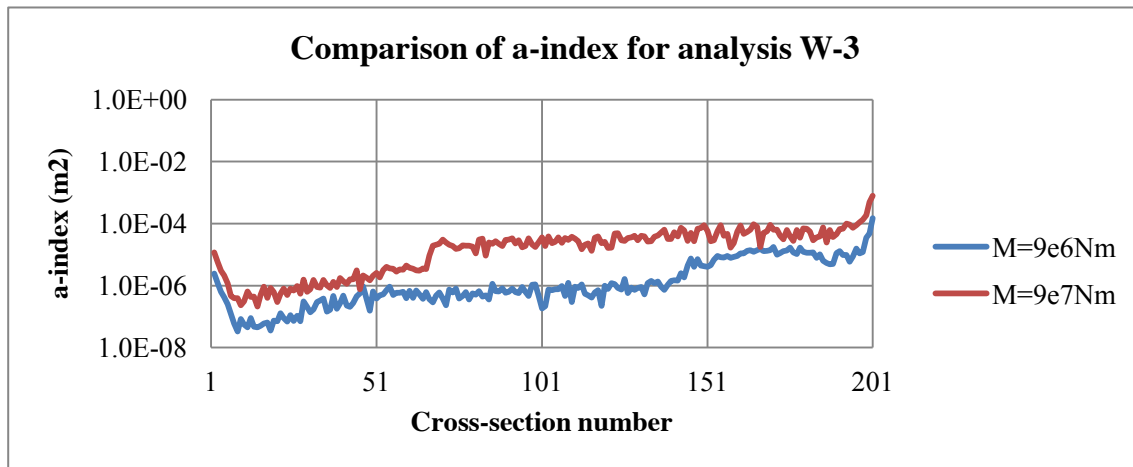


Fig. 5.12 - Comparison of a-index values for analysis W-3 at each cross-section for two arbitrarily chosen values of applied moment.

In analysis W-3, visual inspection of cross-section 201 (the tip of the beam), indicates that warping does occur, especially in the extremities where load or constraints were applied, as seen in Figs. 5.13. Note that the lower extremity suffers less warping than the top extremity, in other words, warping seems to occur more strongly in the extremity that points in the direction towards which bending occurs. In this case, warping clearly does occur, but the main question is: how much warping can be considered acceptable?

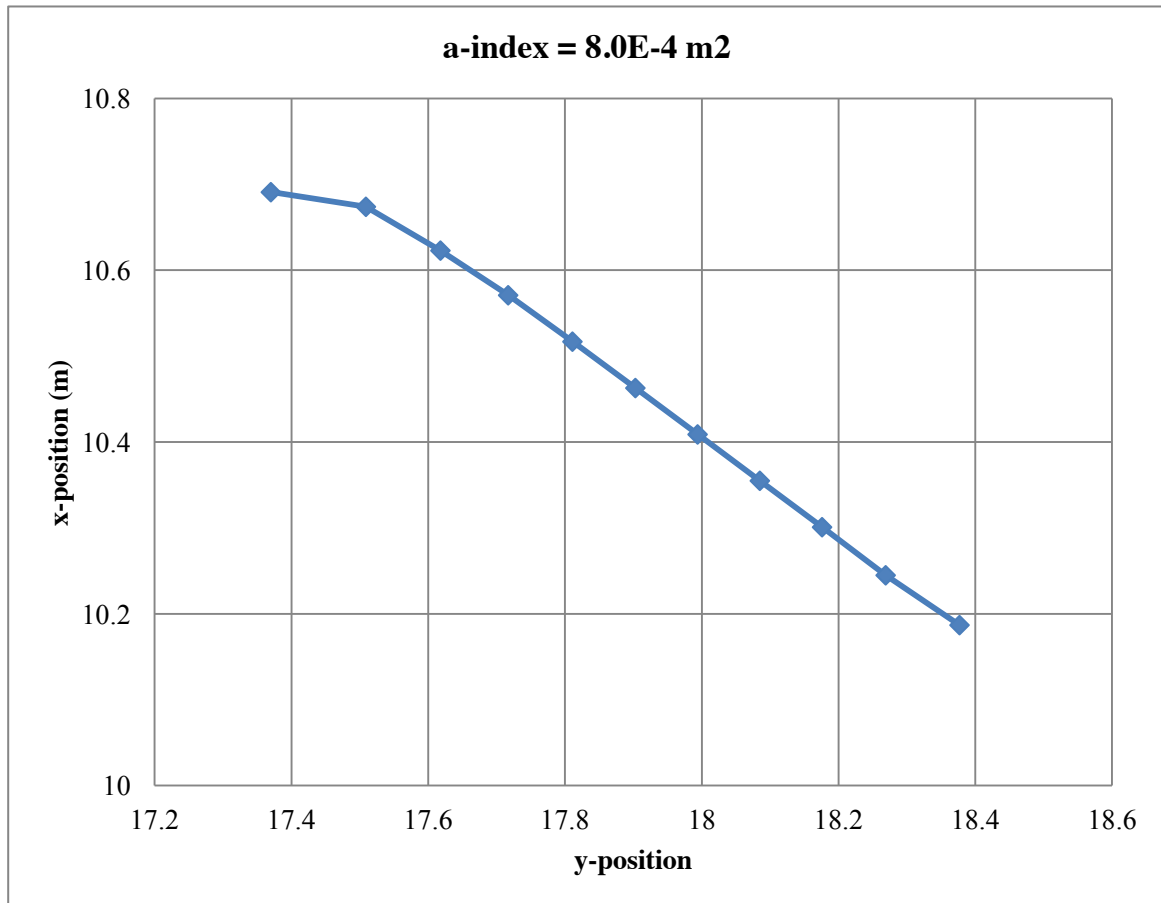


Fig. 5.13 - Visualization of cross-section 201 for analysis W-3.

For the purpose of answering this question, an arbitrary value of a-index - namely,  $1.0\text{E-}4$  - was chosen, and a deeper analysis was conducted in the two cross-sections of W-3 whose a-index had this value. These two cross-sections were the ones numbered 193 and 197. This value can be thought of as a tentative threshold between cross-sections whose warping is acceptable and those with unacceptable values. "Unacceptable" means, here, warping that is large enough as to effect the behavior of beam elements and of their stresses and strains.

Visual inspection of cross-section 197, for example, seems to indicate that the tentative threshold a-index of  $1.0 \times 10^{-4}\text{m}^2$  can be thought of as being associated with cross-sections whose warping is "acceptable". From this observation, most cross-sections of analysis W-2 and W-3 can be said "not to warp", or to warp within "acceptable" limits if one chooses to remain consistent with previously adopted expressions.

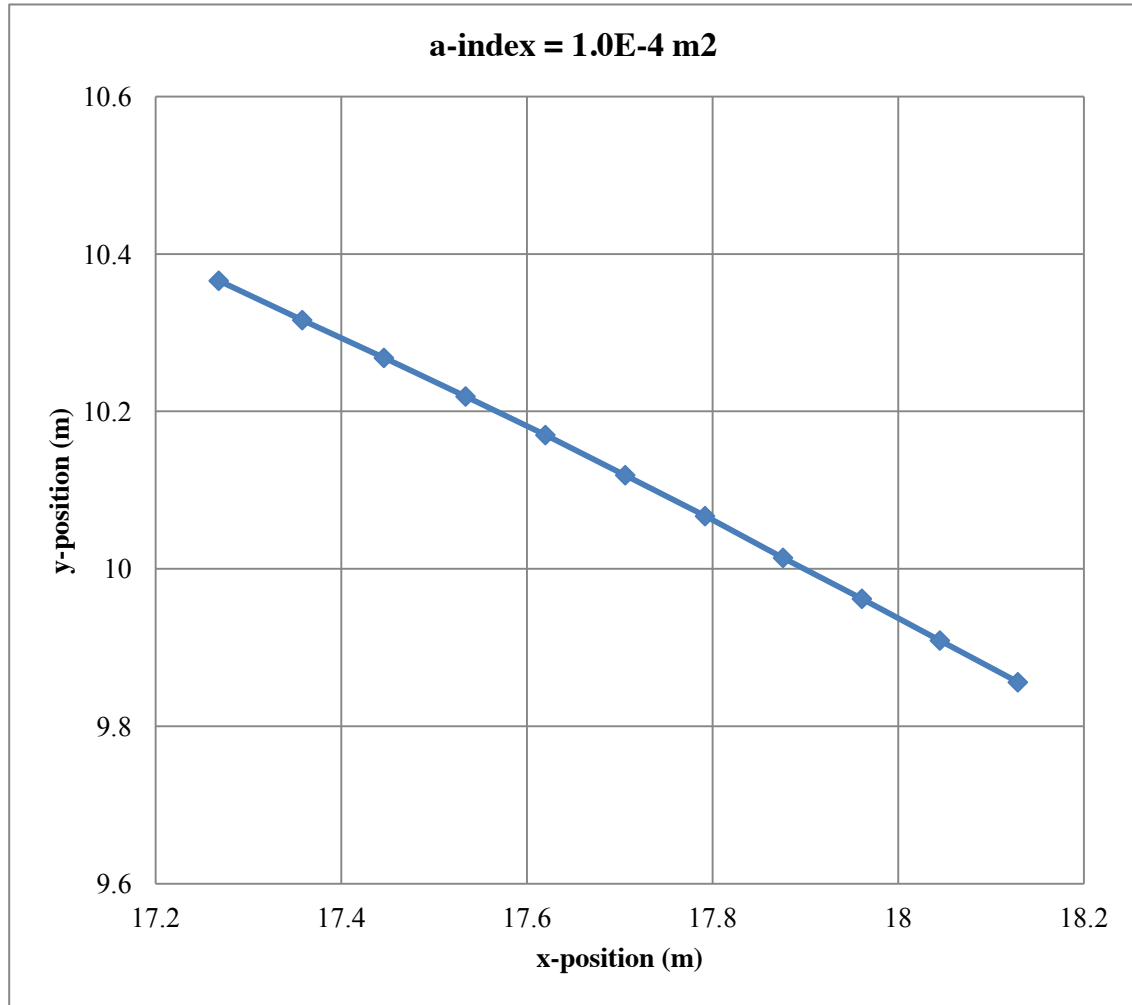


Fig. 5.14 - Visualization of cross-section 197 for analysis W-3.

### 5.2.1 Curvature

The local curvature for cross-sections 193 and 197 was then calculated by use of the parametric formula shown in Eq. 5-1.

$$\kappa = \frac{|x'y'' - y'x''|}{(x'^2 + y'^2)^{3/2}} \quad \text{Eq. 5-1}$$

And the corresponding radius is shown calculated from Eq. 5-2.

$$R = 1/\kappa \quad \text{Eq. 5-2}$$

An analytical parametric function describing these cross-sections is unavailable, but values can be obtained through the finite differences method. Resulting curves were plotted, and can be seen in Fig. 5.15 and 5.16. Note that all values of curvature are below  $0.20\text{m}^{-1}$ , and imply that no radius smaller than 5m can be locally associated with the nodes in this cross-section.

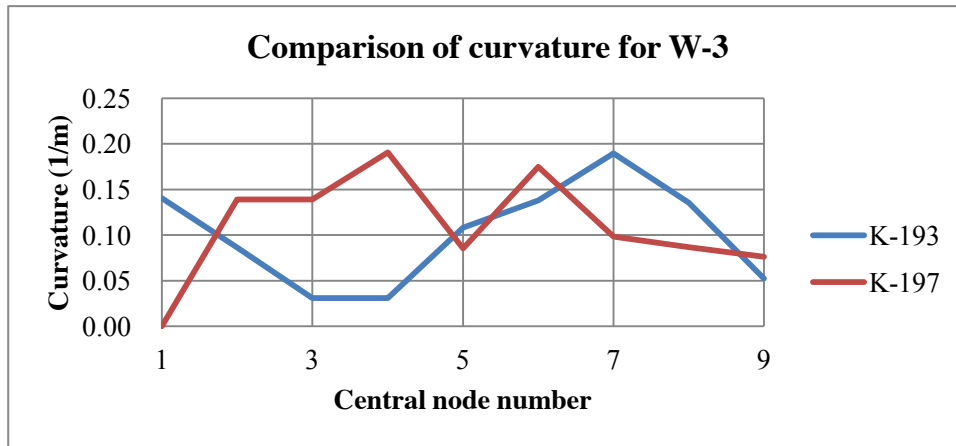


Fig. 5.15 - Comparison of curvature profile of cross-sections 193 and 197 in analysis W-3.

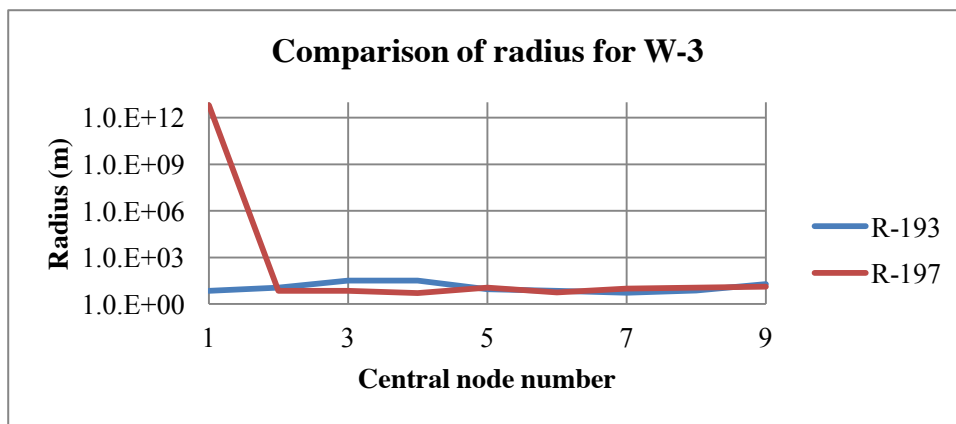


Fig. 5.16 - Comparison of radius profile of cross-sections 193 and 197 in analysis W-3.

### 5.3 Conclusions

Further exploration of this subject is outside the scope of the present work. Suggested lines of questioning would assess the loss of similarity between strains and stresses in function of a value that quantifies the "non-straightness" or "warping" of different cross-sections, and possibly establish boundaries within which the simplification into a linear element yields acceptable simulations.

However, certain conclusions can be drawn from this work. The preliminary results presented herein indicate that, for most practical purposes, the assumption of non-warping cross-sections is valid indeed.

## 6 SSI analysis

In this chapter, the applicability of the proposed large displacement beam elements was assessed within the context of soil-structure interaction (SSI) analysis. In other words, the same analysis was evaluated again and again having distinct formulations ascribed to its beam elements, and then the results of said analysis were inspected for differences. The impact of these differences was then discussed qualitatively.

### 6.1 Sheetpile Permeability analysis (P-analysis)

This analysis is a modified version of example 05a, a simple dynamic drained permeability analysis of FLIP, and its modified version is referred to herein as P-analysis. It is comprised of a fully drained sheet-pile three-phase analysis: self-weight, free-field and then seismic excitation. The material properties and the general scheme of P-analysis can be seen in Fig. 6.1, also, the mesh for this example is shown in Fig. 6.2. The seismic wave utilized in P-analysis was extracted from data collected during the Great Hanshin earthquake that occurred in Kobe, Japan, in January 17 of 1995, and can be seen in Fig 6.3.

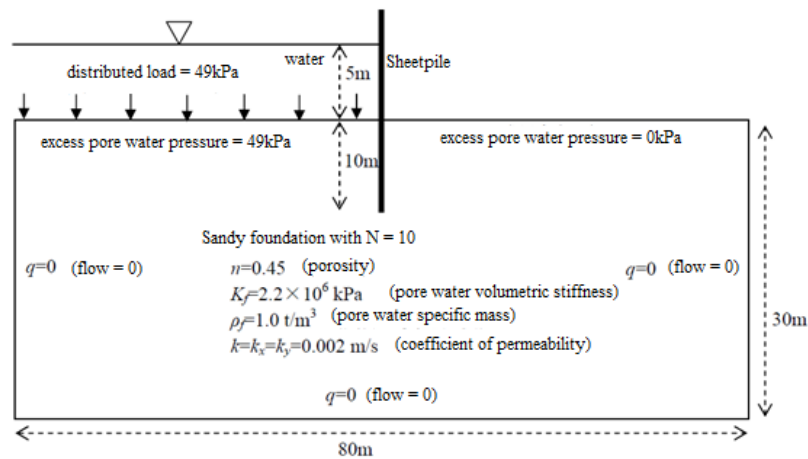


Fig. 6.1 - General scheme of P-analysis.

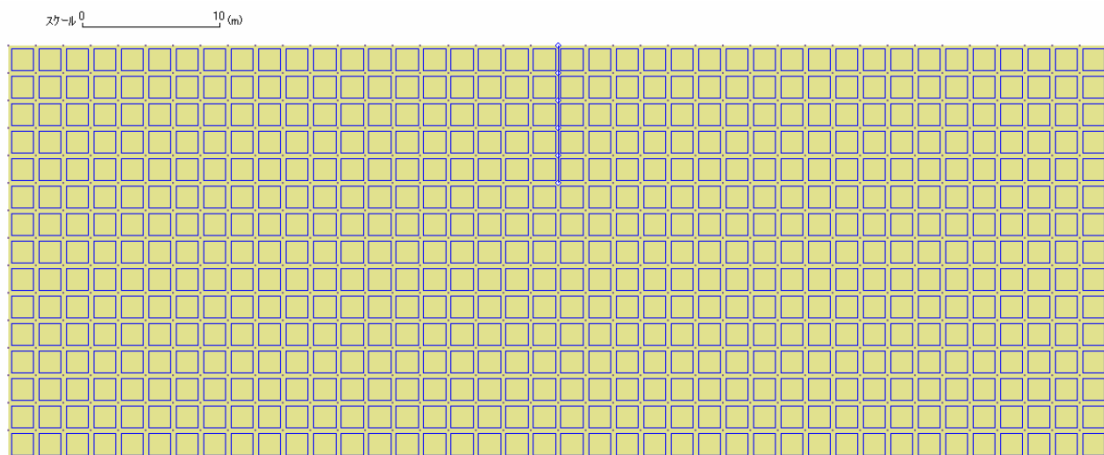
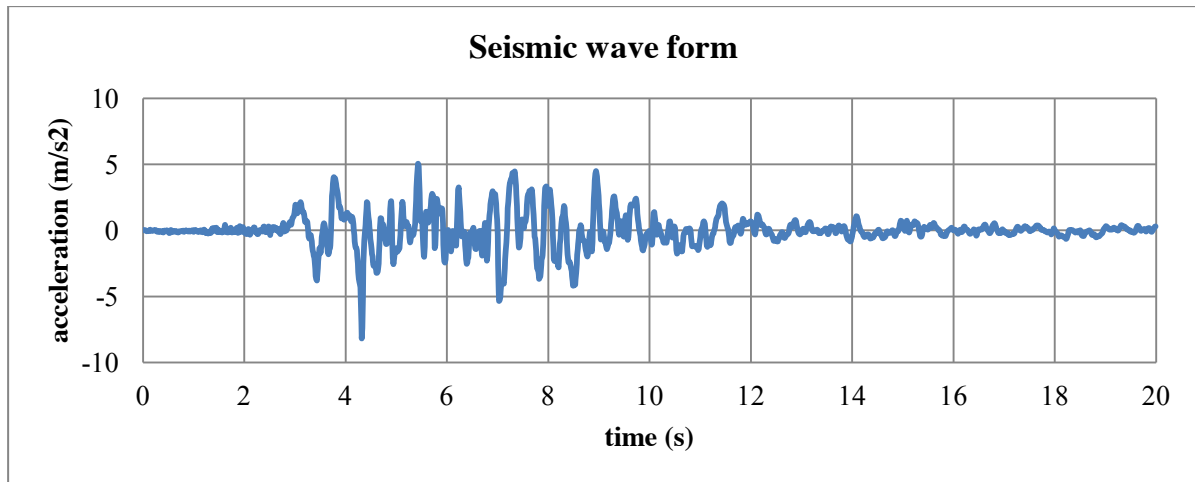
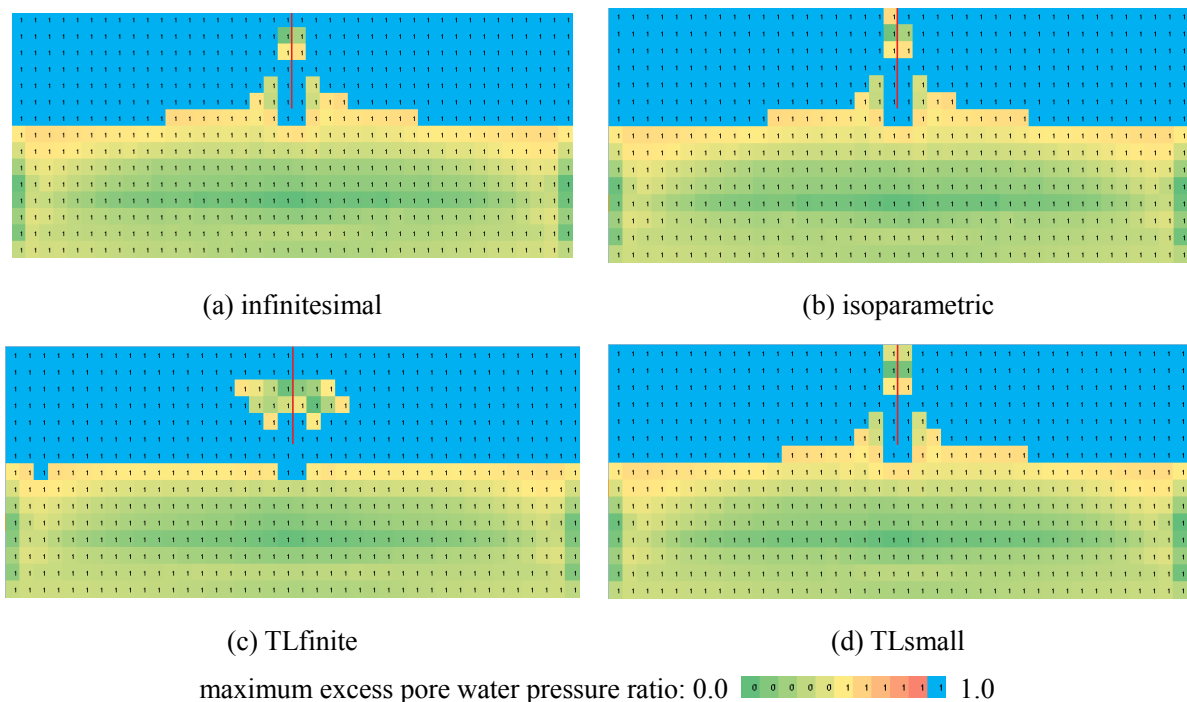


Fig. 6.2 - Mesh for P-analysis.



### 6.1.1 Liquefaction modes

Although this particular analysis would be theoretically within the boundaries of small displacement analysis, results show clearly that the utilization of different formulations in this analysis deeply effects the output. These effects are hinted at by the liquefaction plots shown in Fig. 6.4, where different formulations lead to the liquefaction of a different set of soil elements.



A superficial understanding of the appearance of these different liquefaction modes can be loosely related to

previous analysis wherein the beam behavior differences were ascertained. The same superficial understanding can be related to the displacement time history of the top node of this beam, as shown in Figs. 6.5 through 6.7.

### 6.1.2 Displacements

At first glance, the displacement time histories (Figs. 6.5 through 6.7) seem to be mostly grouped together, indicating certain tendencies, which can be safely thought of as the baseline from which other formulations may differ. In cases where all but one formulations group around certain values, the outlier (in Fig. 6.5 the outlier is TLfinite) will be referred to as the "stray dog". A deeper understanding of these results would have to take into account the fact that the "stray dog" is not always the same when comparing the curves obtained for X-displacements, Y-displacements and B-rotations.

This hints at the insight that, ultimately, the difference between these formulations is how the elements "transfer" stresses and strains between the three custom stress-strain pairs: normal stress-normal strain, shear stress-shear strain, moment-curvature. For example, what was normal stress in a given element may need to be transferred to an adjacent element as a combination of normal stress, shear stress and bending moment due to displacement or rotation. Therefore, another major difference between formulations is how they deal with this interplay of stress-strain pairs, and this is expressed mathematically in the extra terms present in large displacement formulations.

A deeper understanding of why liquefaction modes differ will most likely require a thorough, exhaustive analysis of the way seismic waves reflect and refract when traversing a beam. For example, an intuitive explanation as to why the TLfinite beam seemingly "prevents" liquefaction around itself might be because, since it is more "flexible" than the others, it absorbs more seismic energy than its counterparts.

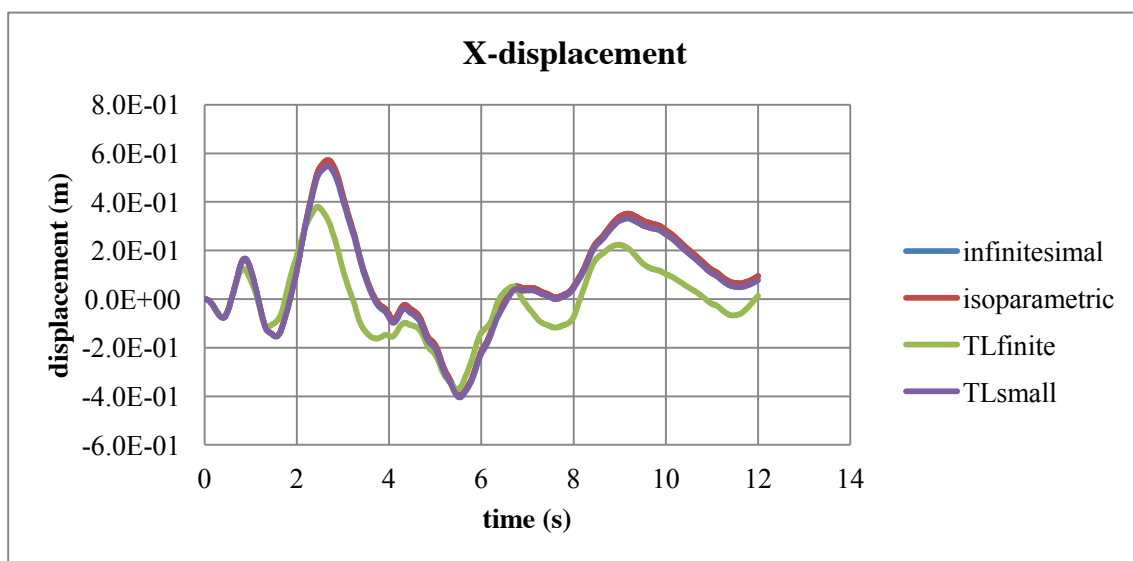


Fig. 6.5 - Beam tip x-displacement time history comparison for Sheetpile P-analysis.



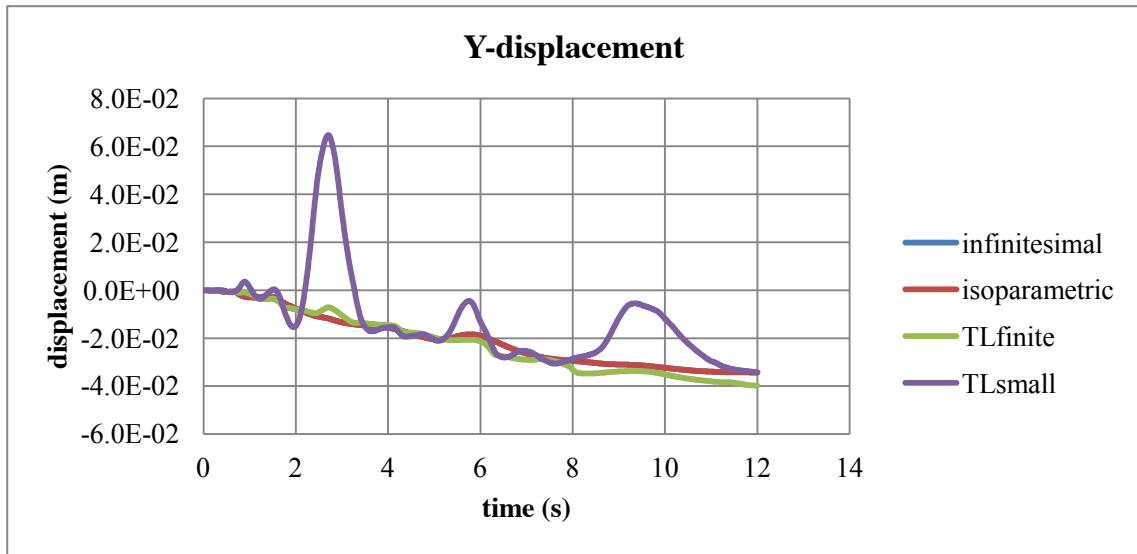


Fig. 6.6 - Beam tip y-displacement time history for Sheetpile P-analysis.

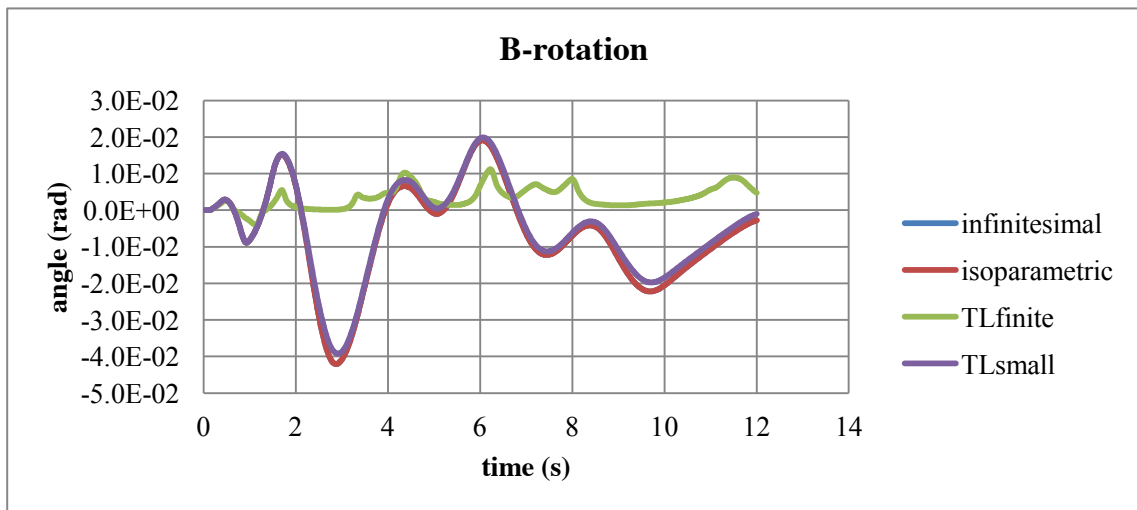


Fig. 6.7 - Beam tip B-rotation time history for Sheetpile P-analysis.

### 6.1.3 Strains

The final strain profiles are shown in Figs. 6.8 through 6.10. A curious trend can be seen for this particular analysis, all final normal strain profiles follow a similar trend, no matter which formulation is used. However, the final shear strain and curvature results show that the TLfinite elements present curves whose values are not even in the same order of magnitude as other elements, as seen in Fig. 6.10, for instance.

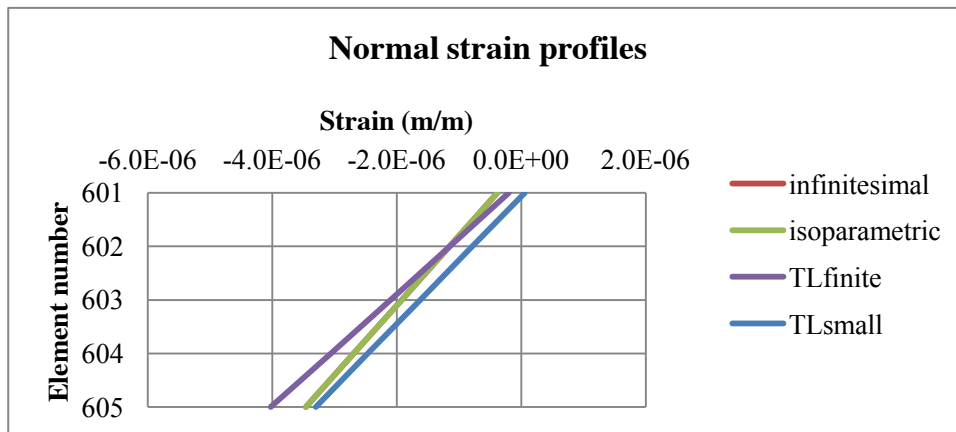


Fig. 6.8 - Normal strain profile comparison for final time step in Sheetpile P-analysis. The infinitesimal curve is hidden beneath the isoparametric curve

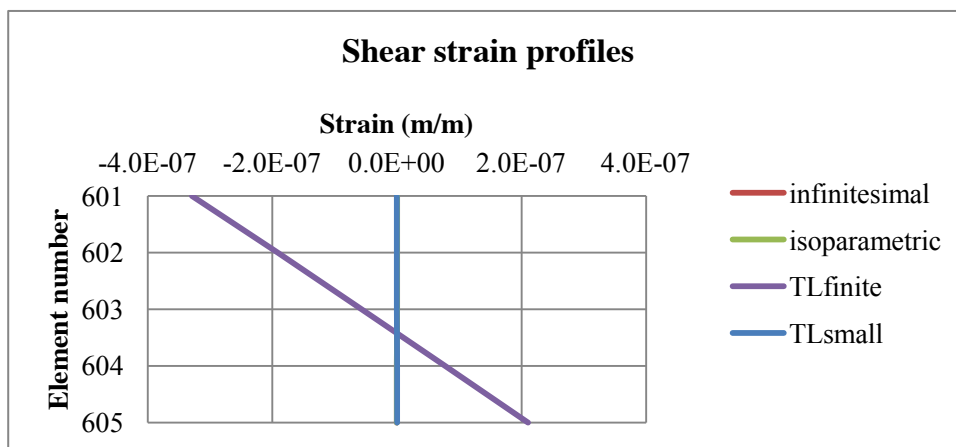


Fig. 6.9 - Shear strain profile comparison for final time step in Sheetpile P-analysis. The infinitesimal and isoparametric curves are hidden beneath the TLsmall curve.

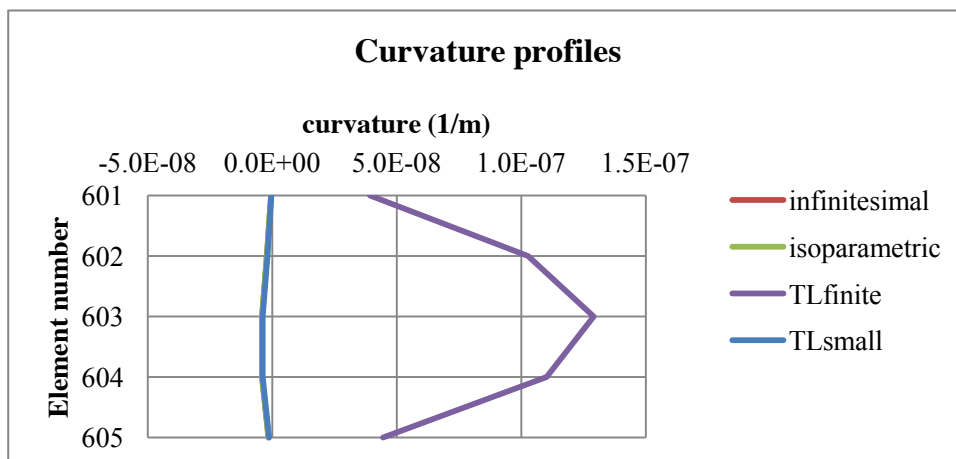


Fig. 6.10 - Curvature profile comparison for final time step in Sheetpile P-analysis. The infinitesimal and isoparametric curves are hidden beneath the TLsmall curve.

#### 6.1.4 Stress

The stress profiles for the various formulations are shown in Figs. 6.11 and 6.12. A trend similar to that of strain profiles can be noticed: TLfinite strays from other formulations, except for its normal stress profile.

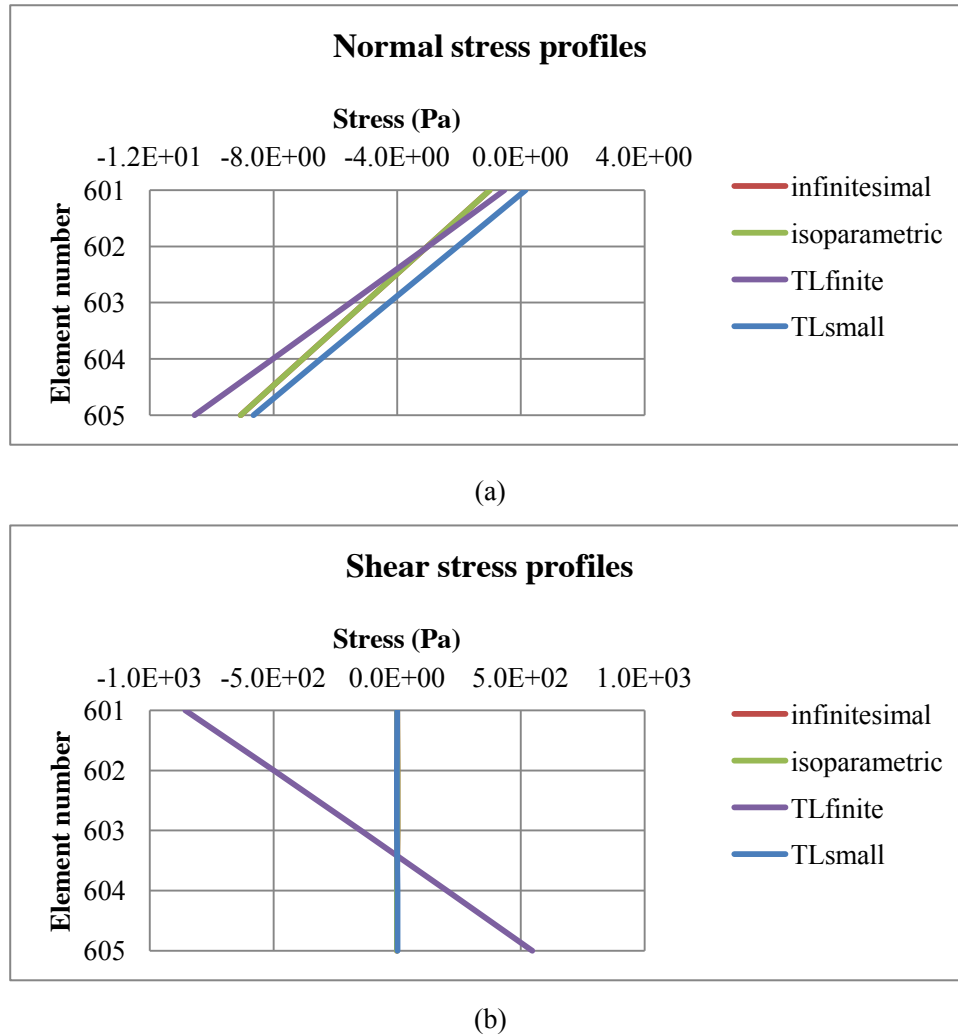
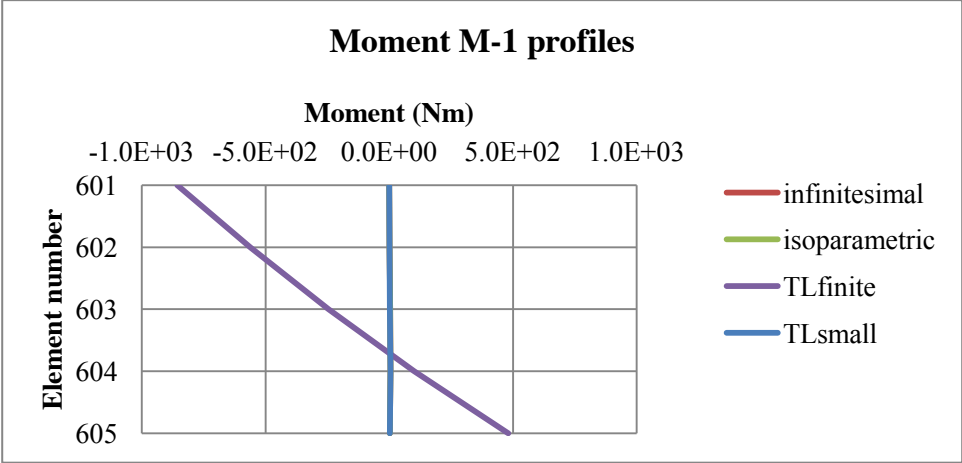
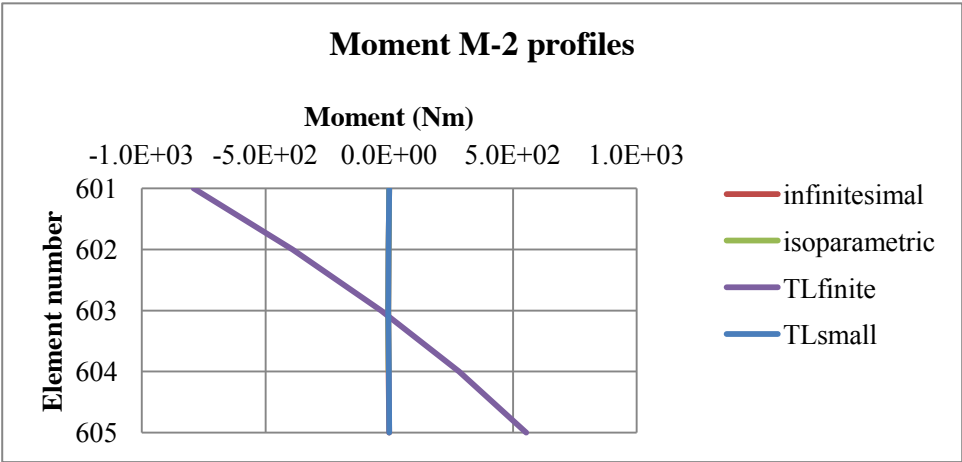


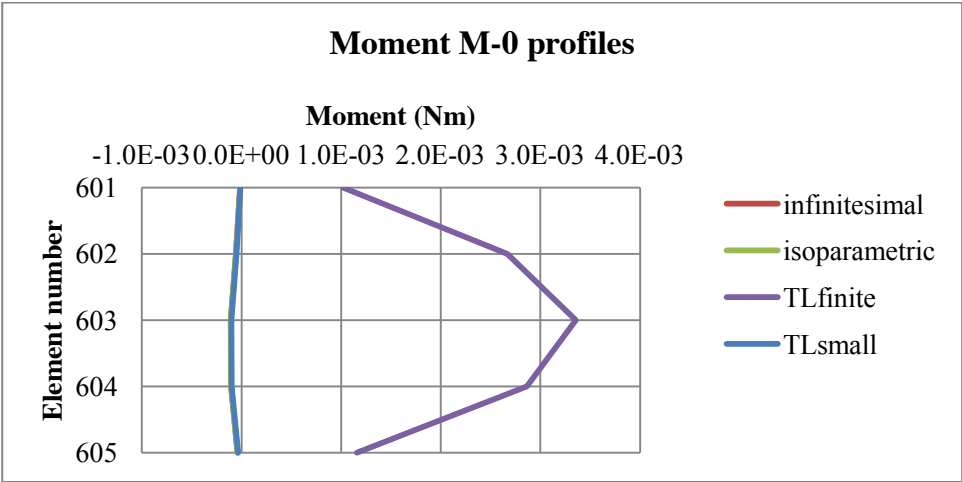
Fig. 6.11 - (a) Normal stress (b) shear stress profile comparison for final time step in Sheetpile P-analysis.



(a) M1



(b) M2



(c) M0

Fig. 6.12 - Moment profile comparison for final time step in Sheetpile P-analysis.

### 6.1.5 Moment-curvature diagrams

The moment-curvature ( $M - \emptyset$ ) curves were then obtained, and the tip moment for the top element and its central moment were plotted and are shown in Figs. 6.13 through 6.16, for different formulations. More specifically, the difference between maximum values of the curves for infinitesimal formulations and for TLfinite formulation is of more than one order of magnitude (see Figs. 6.11 and 6.13).

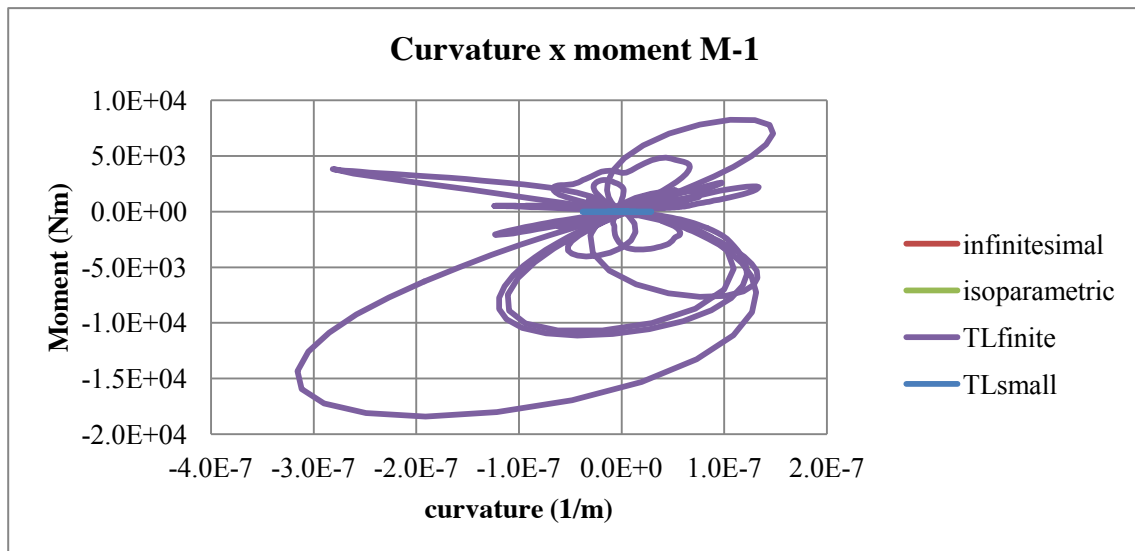


Fig. 6.13 -  $M - \emptyset$  diagram for the top element of the beam in Sheetpile P-analysis.

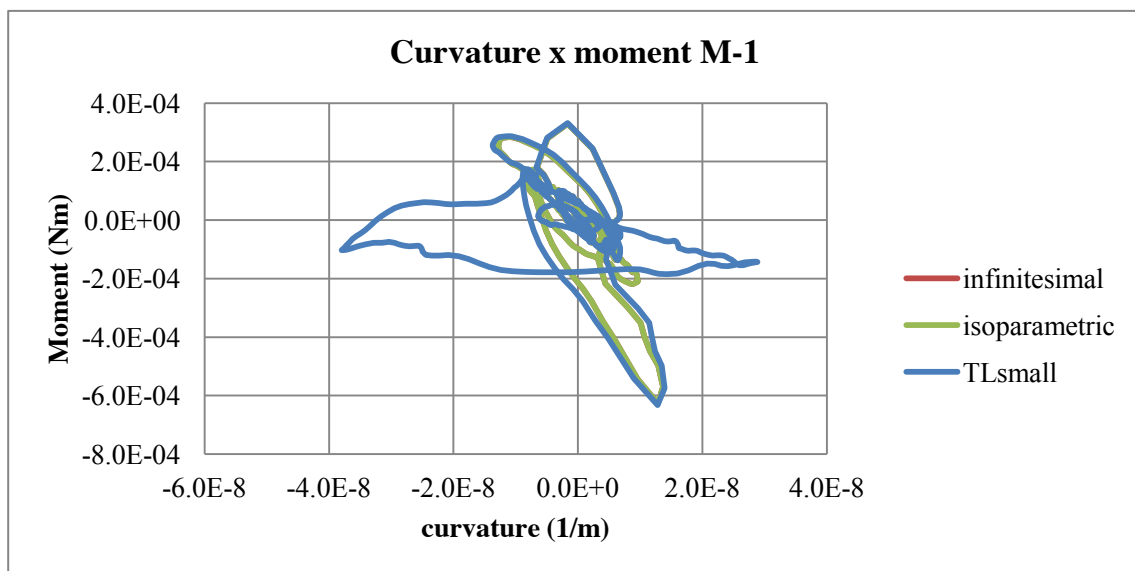


Fig. 6.14 -  $M - \emptyset$  diagram for the top element of the beam in Sheetpile P-analysis.

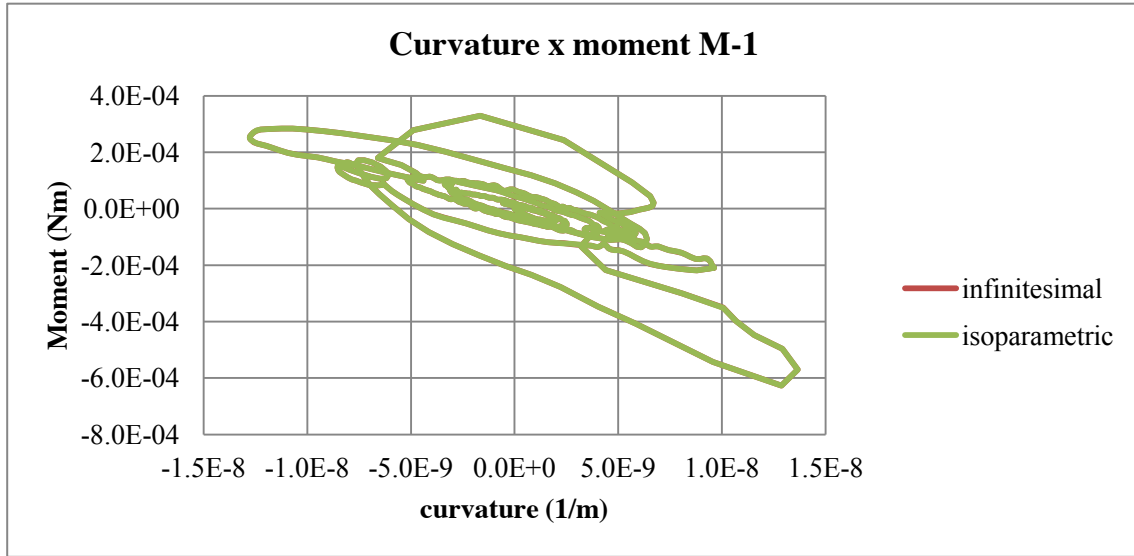


Fig. 6.15 -  $M - \phi$  diagram for the top element of the beam in Sheetpile P-analysis.

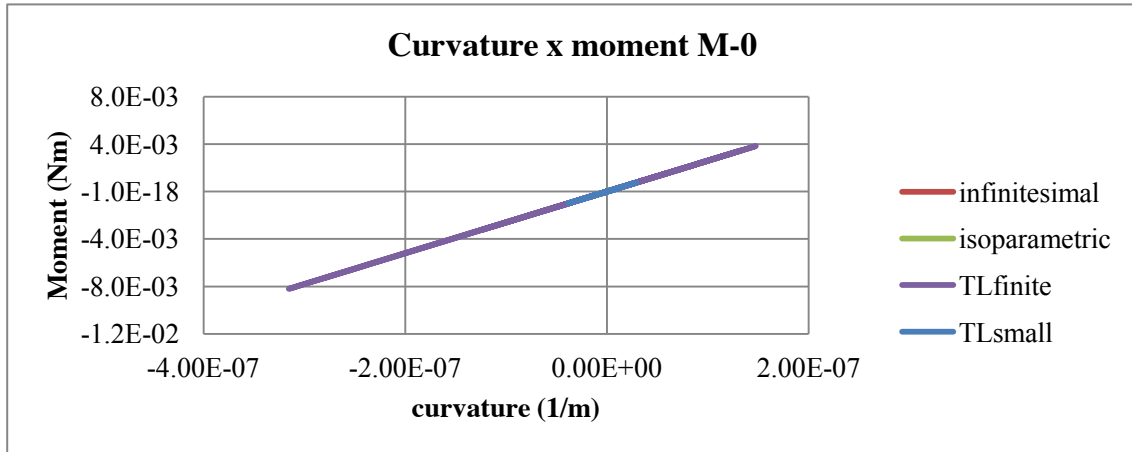
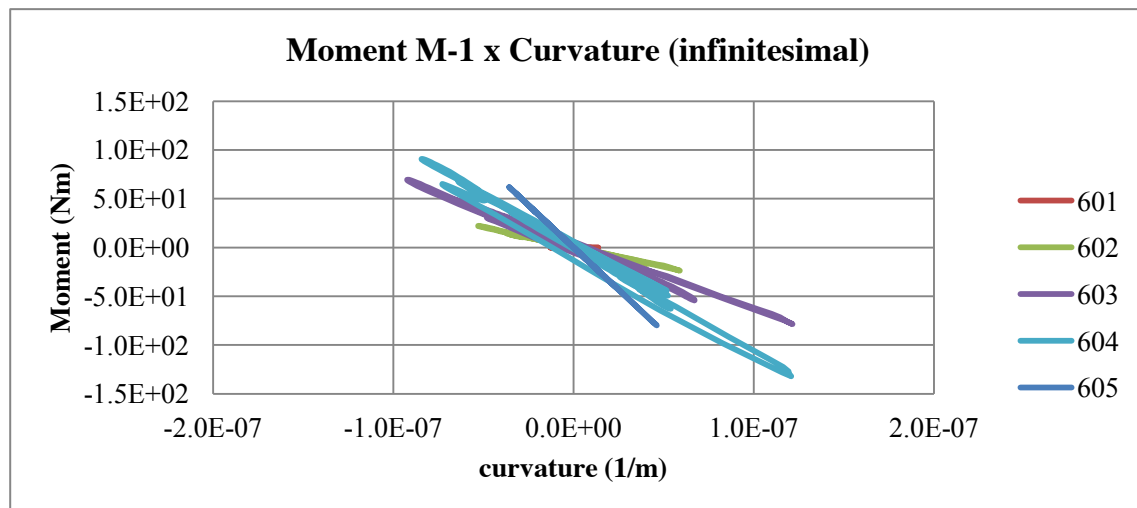
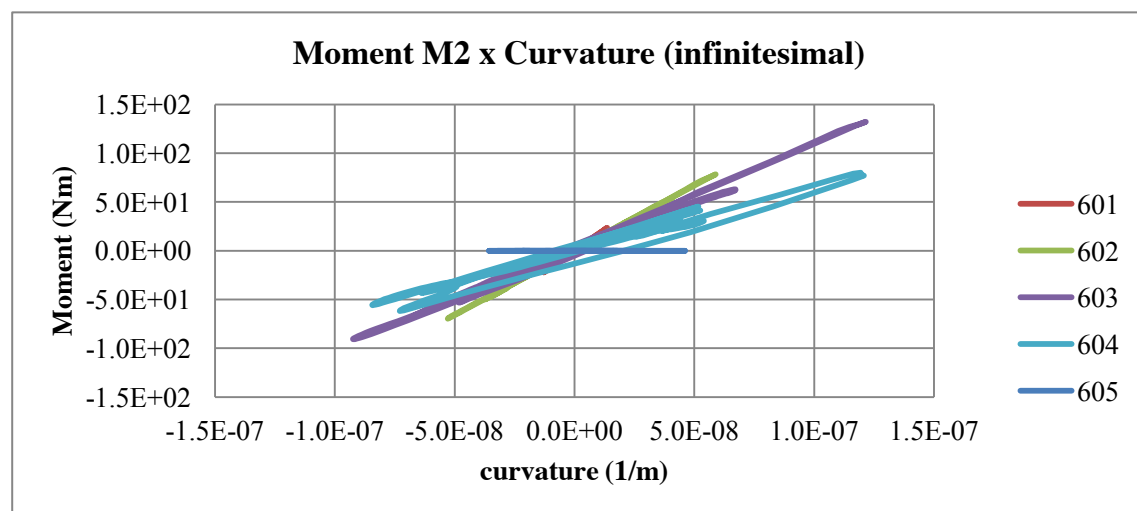


Fig. 6.16 -  $M - \phi$  diagram for the top element of the beam in Sheetpile P-analysis.

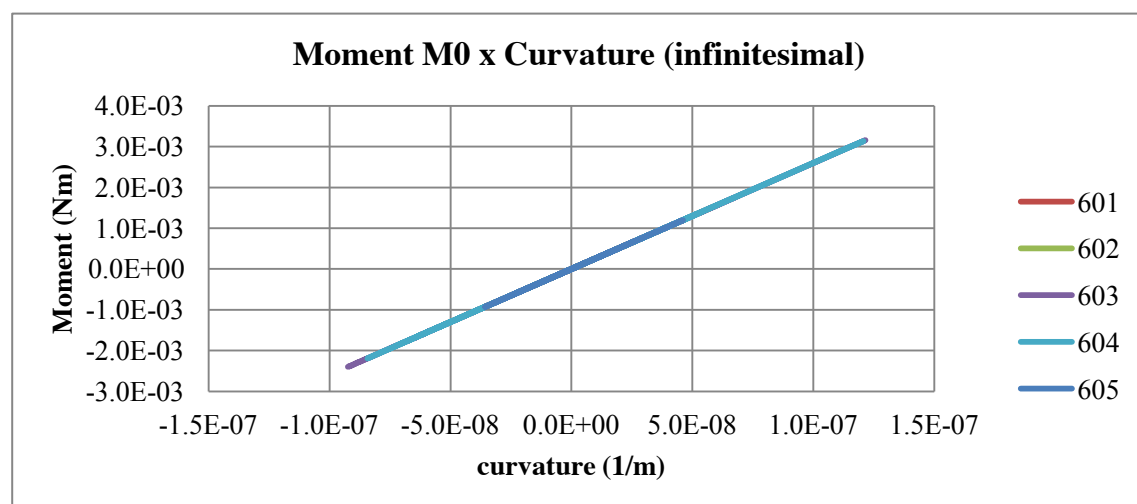
Also, note that Fig. 6.16 is representative the basic elastic behavior expected in a beam. To further understand these results, Figs. 6.17 through 6.20 were plotted. These figures are comprised of the moment-curvature curve for all four formulations. For each formulation, the central moment ( $M-0$ ) curve is invariably representative of how these formulations are materially elastic. The tip moment curves, i.e.  $M-1$  and  $M-2$ , can be thought of as representative of how the seismic waves propagate through beams. These curves, especially the curve shown in Fig. 6.13, are of paramount importance. The reason for this is that the moment represented in this curve is the moment that will be transmitted to the super-structure above.



(a)

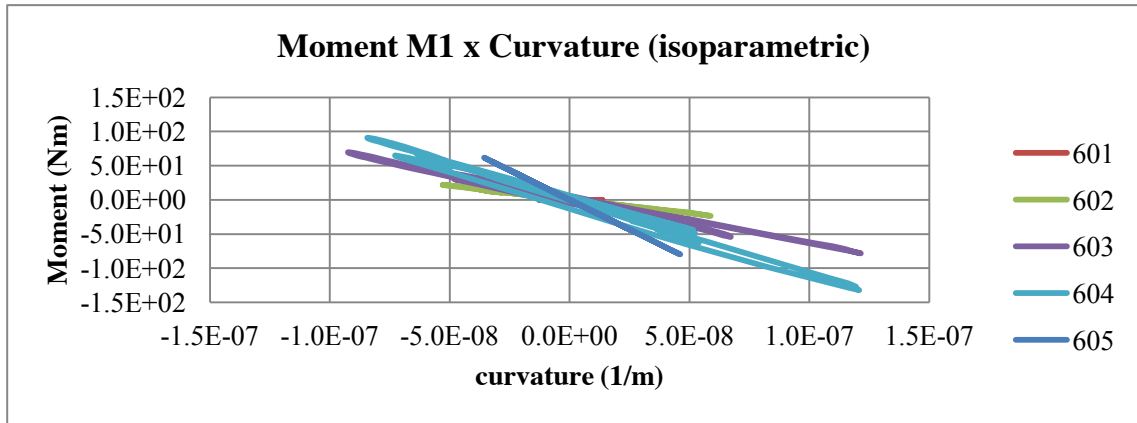


(b)

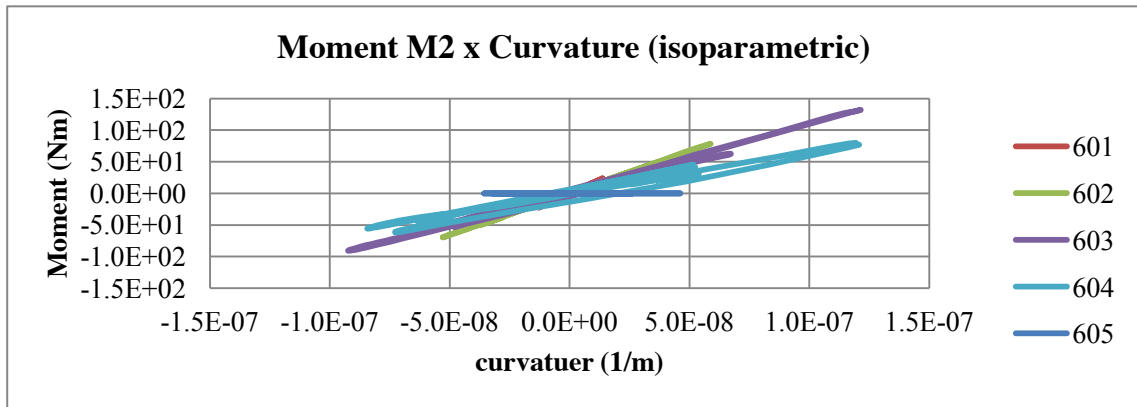


(c)

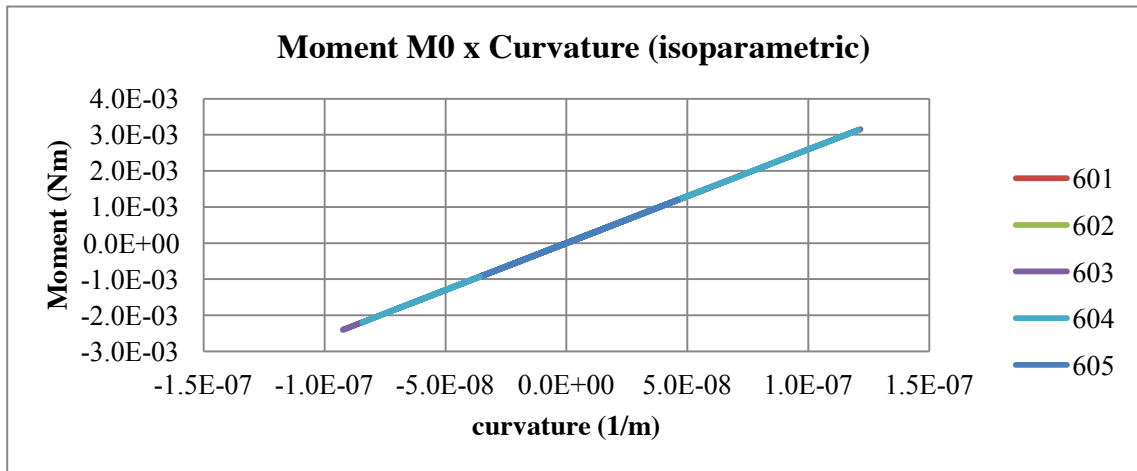
Fig. 6.17 - M –  $\phi$  diagrams for infinitesimal formulation in Sheetpile analysis.



(a)



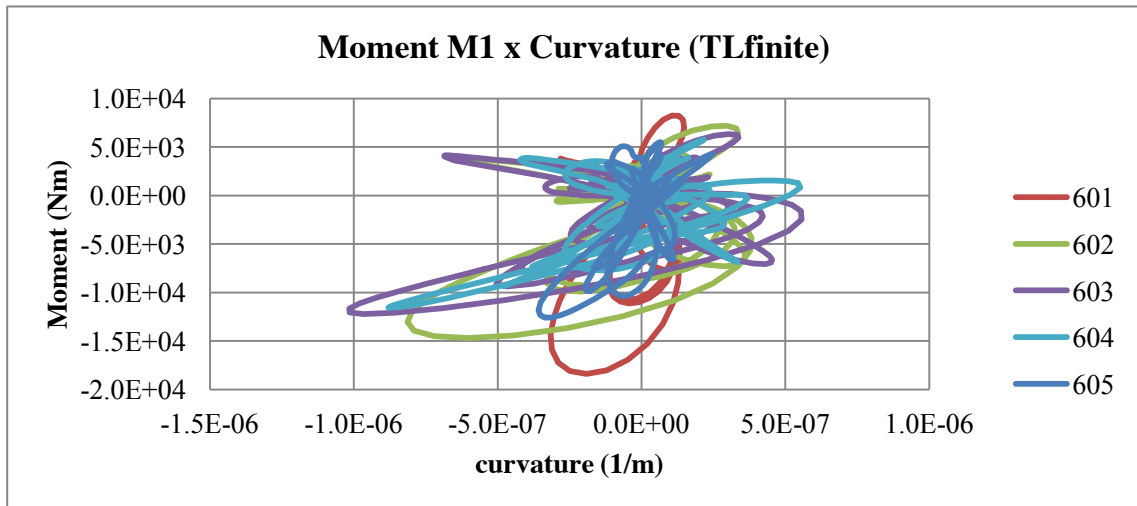
(b)



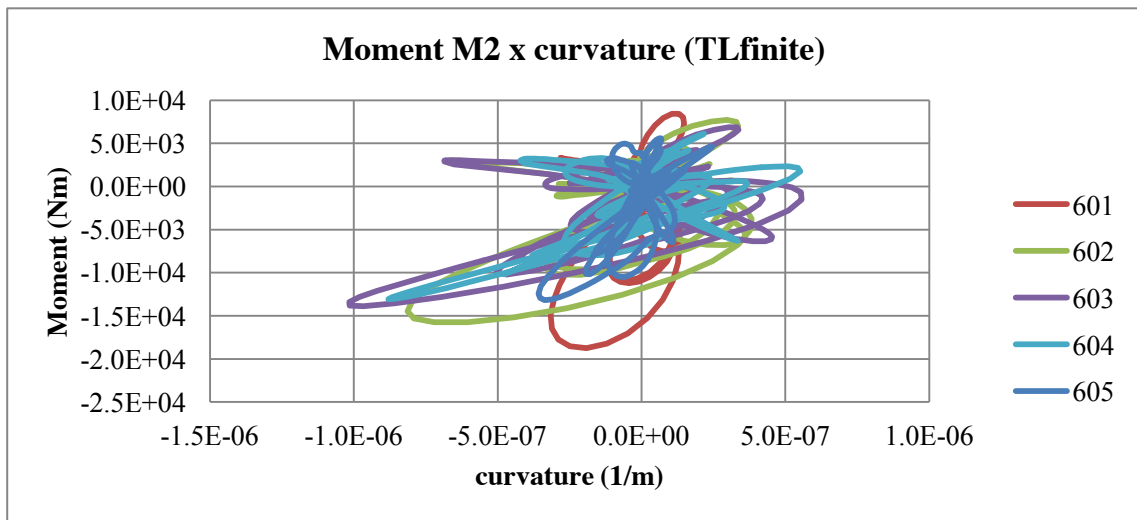
(c)

Fig. 6.18 - M –  $\emptyset$  diagrams for isoparametric formulation in Sheetpile analysis.

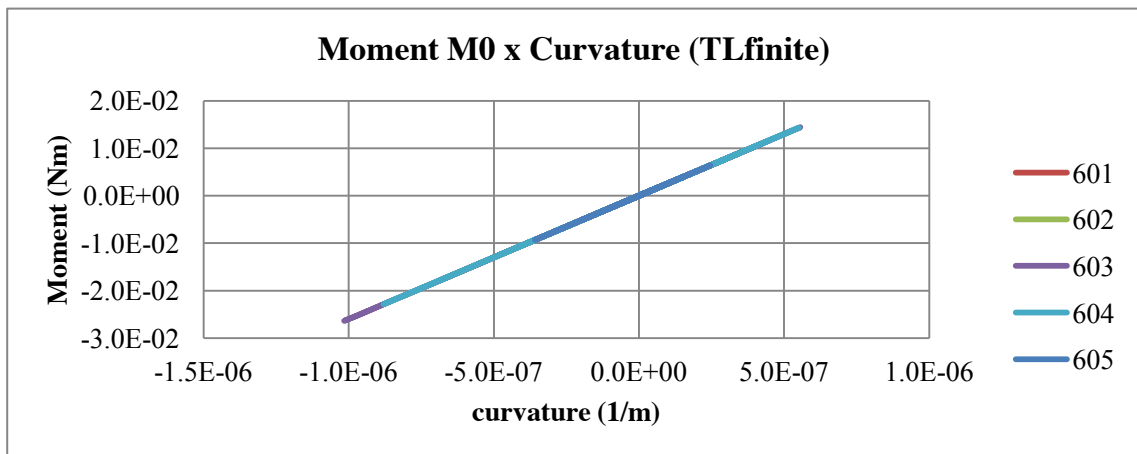




(a)

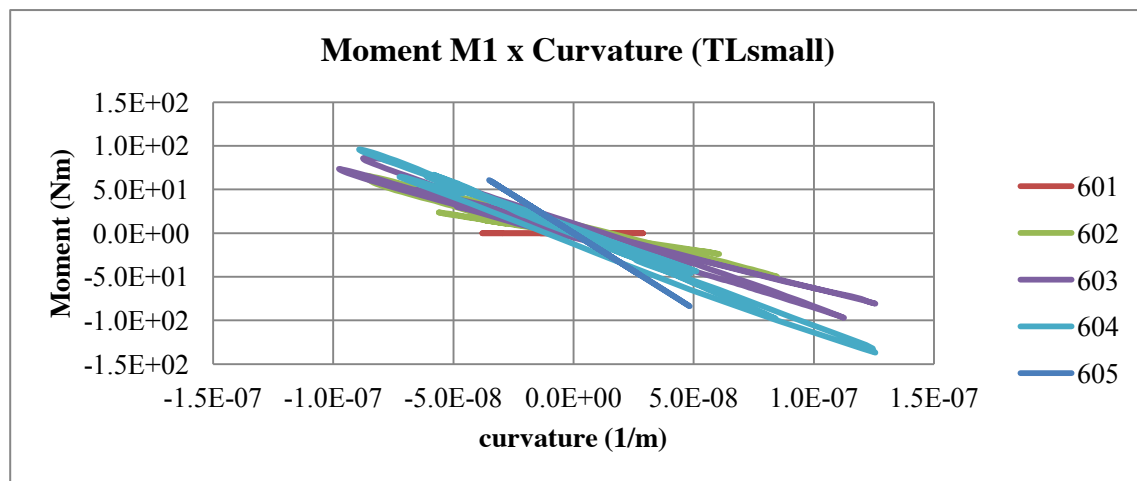


(b)

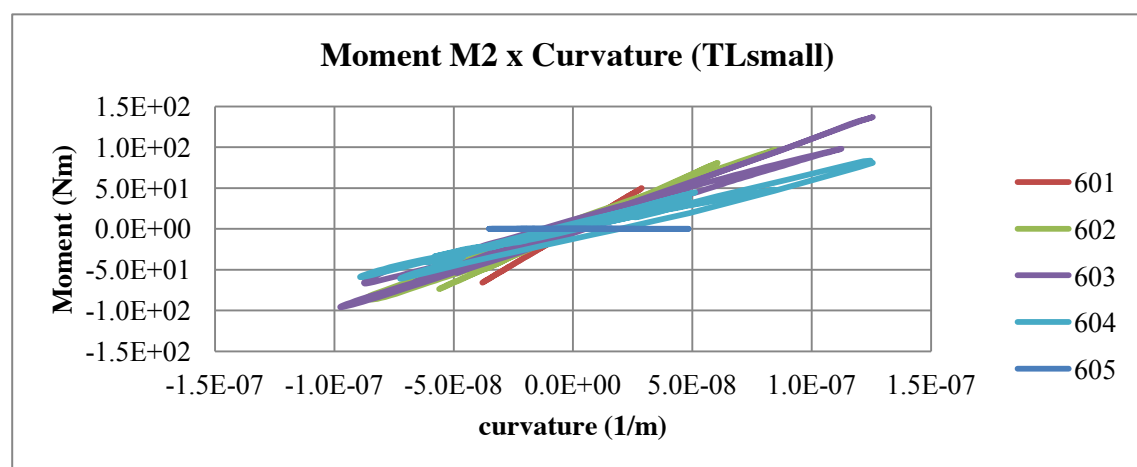


(c)

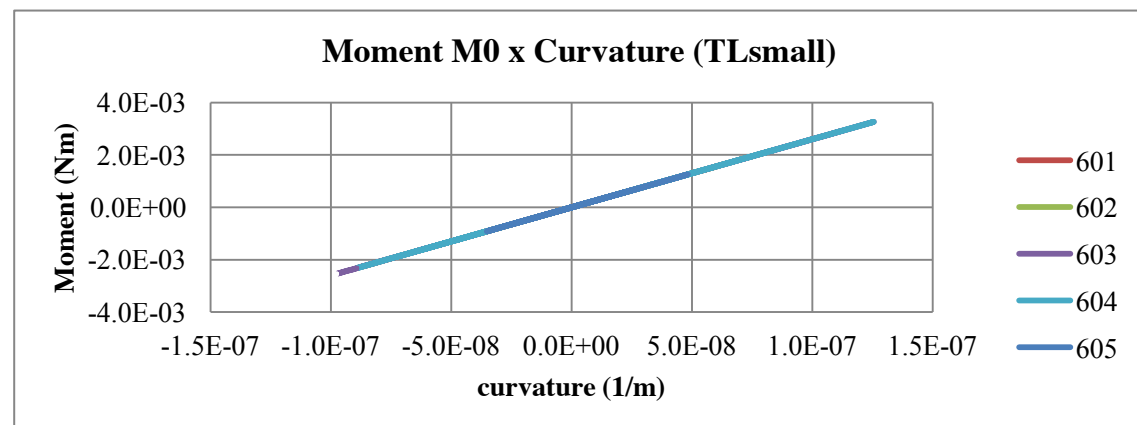
Fig. 6.19 - M –  $\phi$  diagrams for TLfinite formulation in Sheetpile analysis.



(a)



(b)



(c)

Fig. 6.20 - M –  $\phi$  diagrams for TLsmall formulation in Sheetpile analysis.

### 6.1.6 Conclusions

From these results, initial interpretations are not very soothing, because they seem to indicate that formulations currently used do not fully express the forces (particularly the bending moment) to which the super-structure will be subjected. In the model used for the Sheetpile P-analysis, the super-structure is not particularly important. However, a super-structure such as a skyscraper could be gravely affected by the underestimation of transmitted stresses. This observation may, if confirmed, lead to more conservative design principles for this type of structure. A revision of design principles that are based on  $M - \emptyset$  diagrams may be desirable.

### 6.1.7 Suggested lines for further inquiry

A thorough examination of the results presented in section 6.1.5 implies that the next step in this line of research must be to evaluate each formulation within certain contexts of SSI analysis. One possibility is to concoct SSI experiments that allow for a visualization of the parameters that differentiate between formulations. For example, Sheetpile P-analysis exhibits small differences between formulations in many domains, but the most important distinction between formulations may be the  $M - \emptyset$  diagrams. This is so not only because they show sharper differences between formulations, but also because they are used in the design of new structures.

Another possible line of inquiry would be to search for cases where failure modes change from formulation to formulation. This is hinted at in Fig. 6.4, where the set of elements that liquefy changes with each formulation. An analysis similar to this one is not the most desirable, however, due to the fact that the difference between failure modes isn't clear and explicit, that is, it can't be easily perceived and accounted for in an experimental setting.

## 6.2 Sheetpile Large Displacement analysis (LD-analysis)

Another SSI analysis was simulated and implemented according to the schematic shown in Fig. 6.21, in order to further explore the application of the herein proposed large displacement beam elements. This analysis will be referred to herein as SheetPile LD-analysis, but this time under undrained conditions.

This analysis was implemented through a two-step self-weight static analysis, followed by the undrained dynamic phase. In the first step of the self-weight analysis, the top node of the SheetPile was constrained in the X direction. The wave that was used for seismic excitation in the dynamic phase is shown in Fig. 6.22.

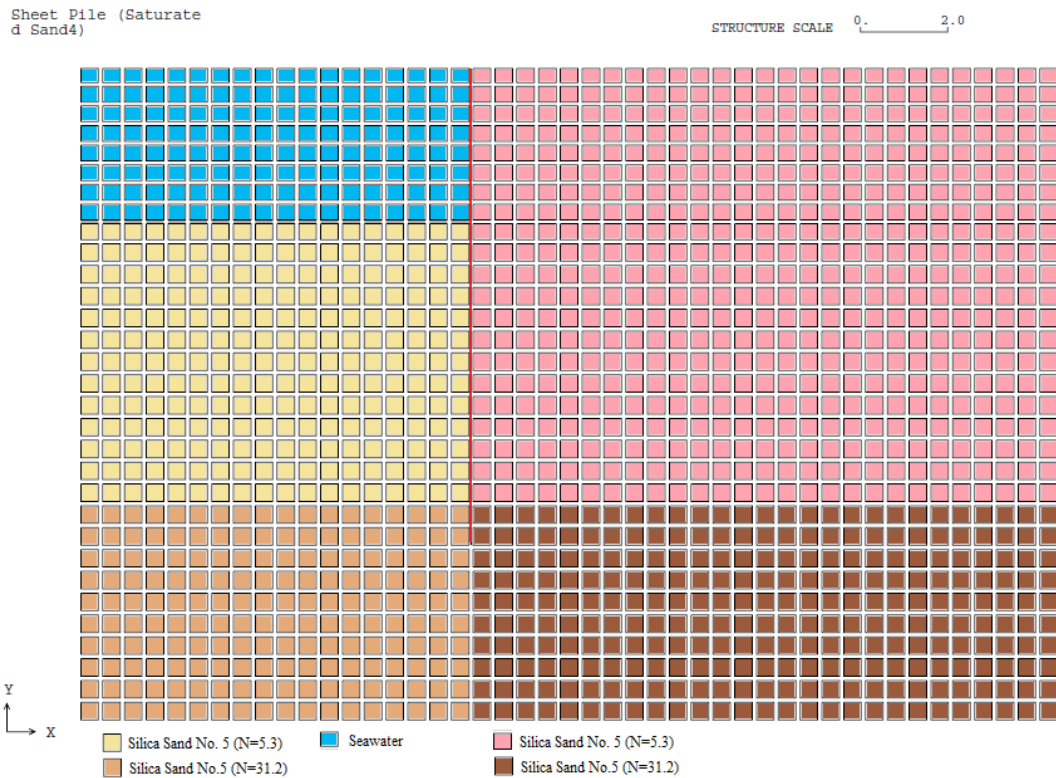


Fig. 6.21 - General scheme of SheetPile LD-analysis.

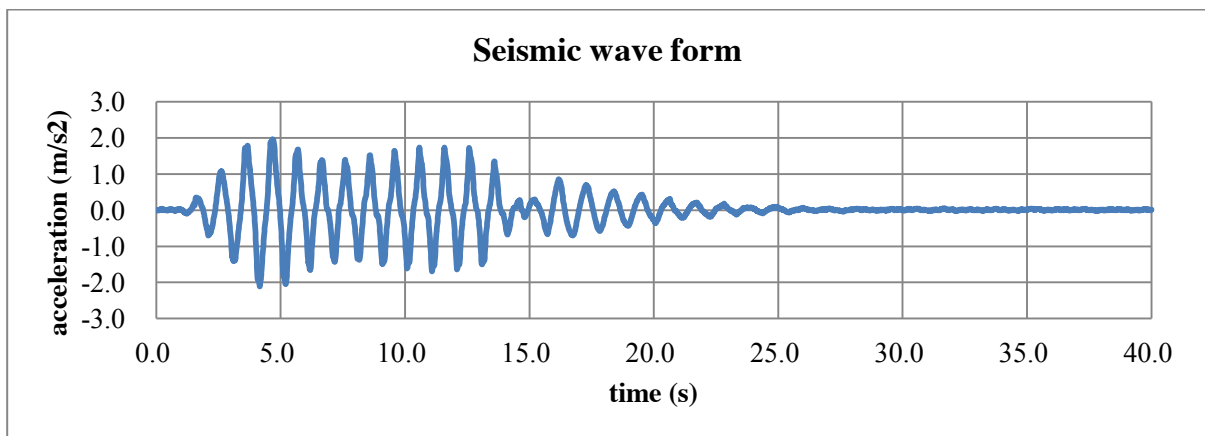


Fig. 6.22 - Wave form input for the dynamic phase of SheetPile LD-analysis.

### 6.2.1 Initial LD-analysis

The SheetPile LD-analysis was then run several times by adopting different beam formulations for the beam elements that make the SheetPile, and various results were obtained in each case. The final resulting displacements for the linear isoparametric beam are shown in Fig. 6.23, and exemplify the order magnitude of final displacements. An initial comparison of the tip displacements is shown in Fig. 6.24. Note that the results presented under TLsmall are not acceptable, because they show a positive displacement in the Y direction, which would mean that the SheetPile went upwards, but this is not observed in reality. This was

shown to be related to the MPC connection in the Y-direction that is utilized in small displacement analyses between the bottom node of the SheetPile and adjacent soil elements.

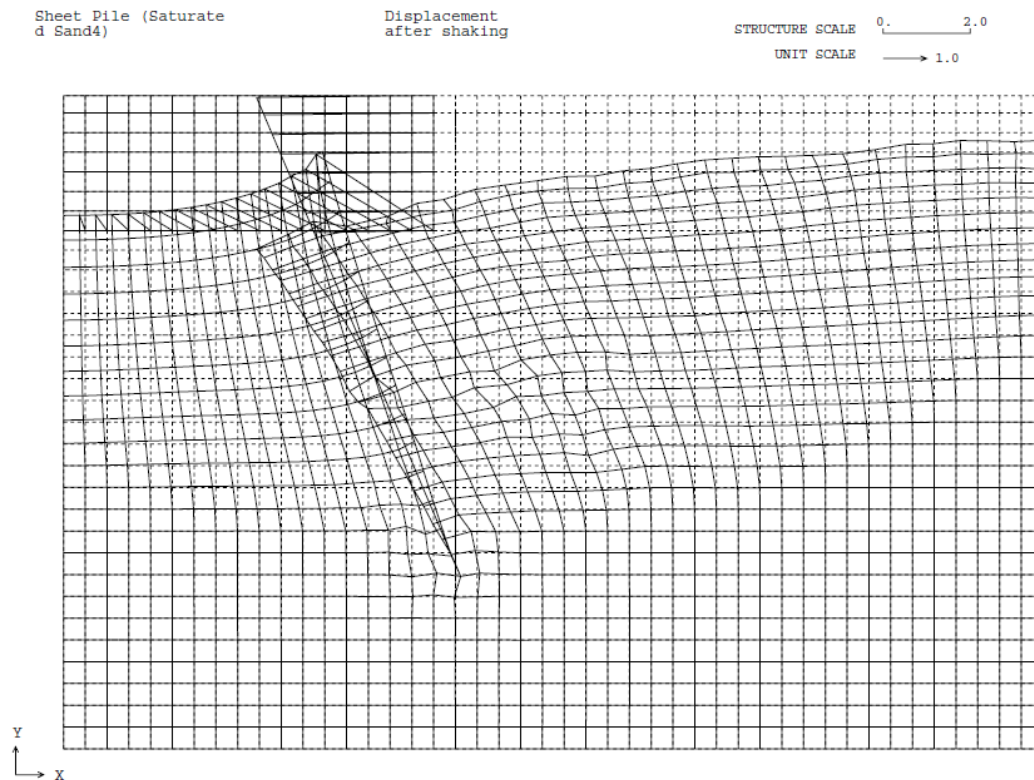
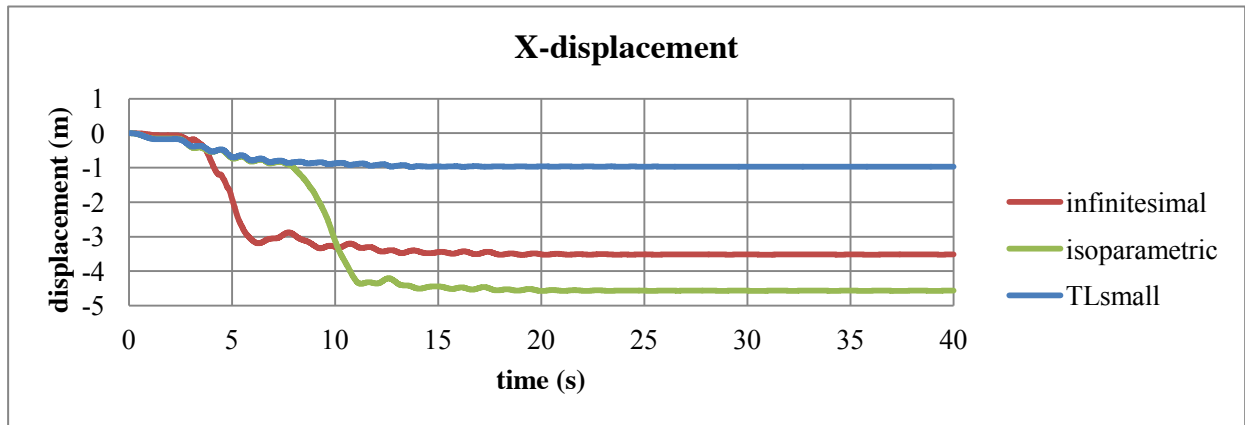


Fig. 6.23 - Final displacements for SheetPile with isoparametric formulation.

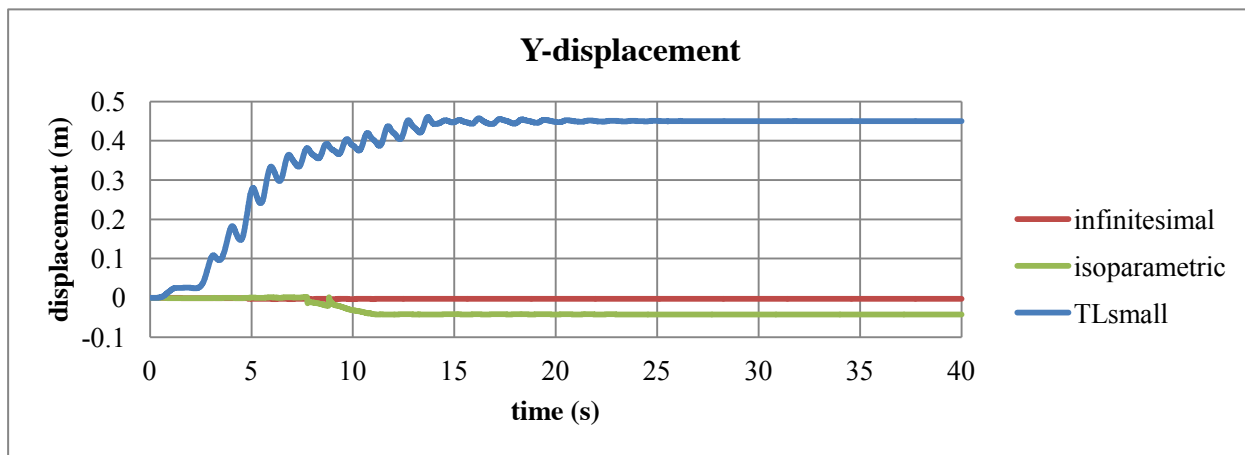
In Fig. 6.25c, note how the extra malleability of the large displacement beam causes liquefaction to be much less prevalent than in small displacement formulations. In Figs. 6.24a and 6.24c, the effects of this fact can be clearly appreciated.

In the SheetPile LD-analysis, there is no nodal force contribution from the soil in the vertical direction towards the Y-displacement of the beam, and the observed vertical displacements occur due to the vertical attachment of the bottom node of the beam to surrounding soil elements. However, the proposed large displacement beam element does account for the effect of horizontal nodal forces applied to an inclined beam, as is shown in Fig. 6.23. The effect of this can be seen in Fig. 6.24b.

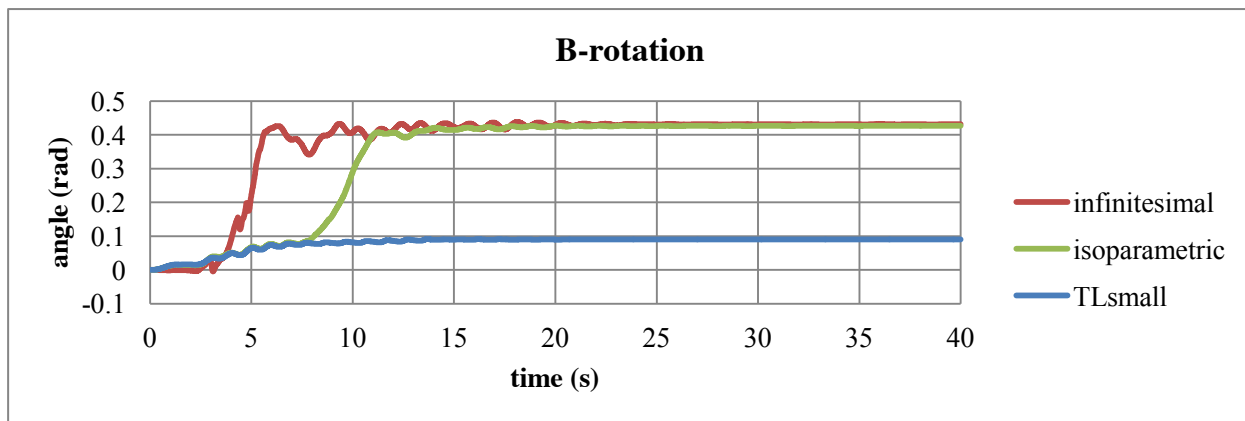
One of the proposed solutions to the vertical displacement issue is to simply release vertical displacement for the large displacement beams. This is appropriate, because horizontal effects are being adequately transferred to the vertical direction. Also, convergence with the TLfinite formulation showed a plethora of issues, and that is why no results are shown. The need to address and remedy these issues lead to the idealization of another series of analyses that, referred to as Refined SheetPile LD-analysis.



(a)



(b)



(c)

Fig. 6.24 - Comparison of displacements for the top node of the beam for initial SheetPile LD-analysis.

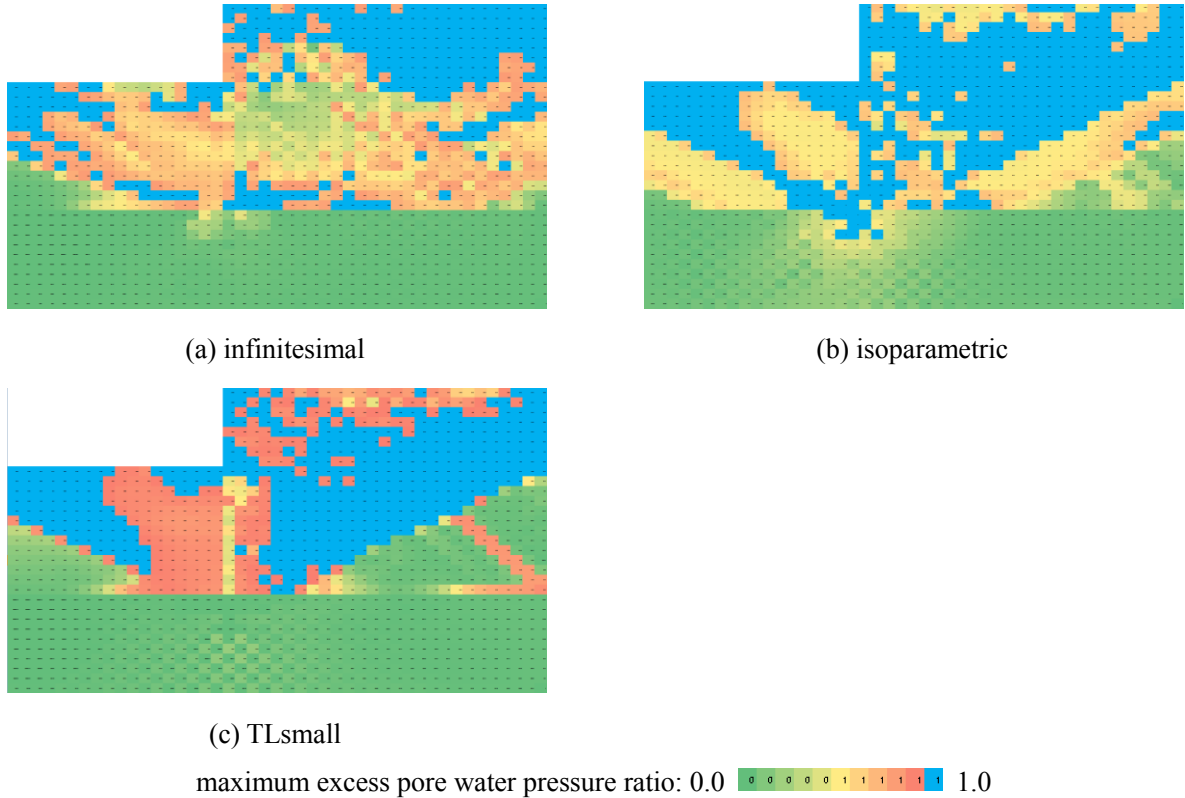


Fig. 6.25 - Comparison of elements that suffered liquefaction during LD-analysis (bright blue elements suffered liquefaction).

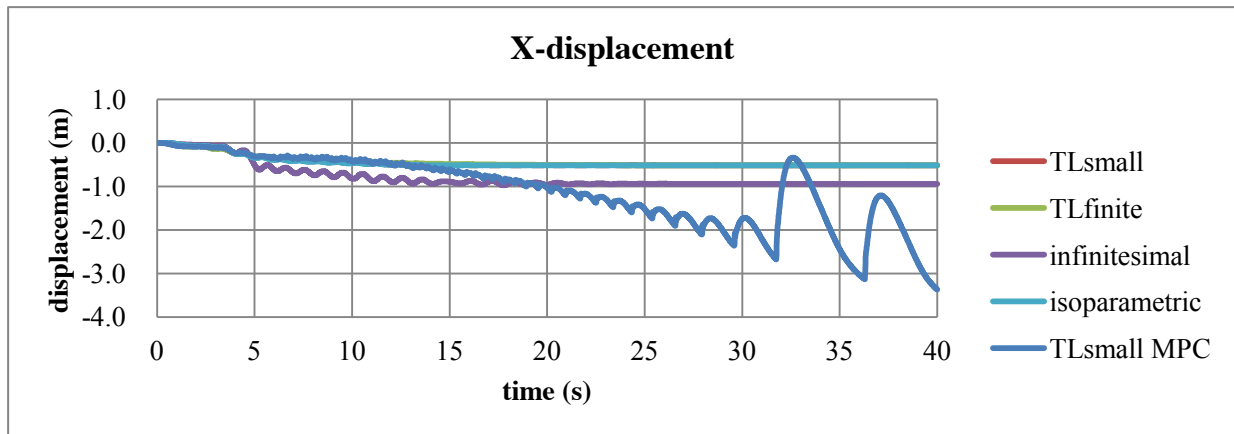
### 6.2.2 Refined LD-analysis

This analysis is almost the same as the initial LD-analysis, except for the fact that an aggressive stance towards convergence was adopted. Thus, the amplitude of the input seismic excitation was cut by half. Also, Rayleigh damping parameters were allowed to be varied between analyses within an acceptable range. For purposes of comparison, the same modifications were applied to all analyses, and results are presented in Figs. 6.26 and 6.27.

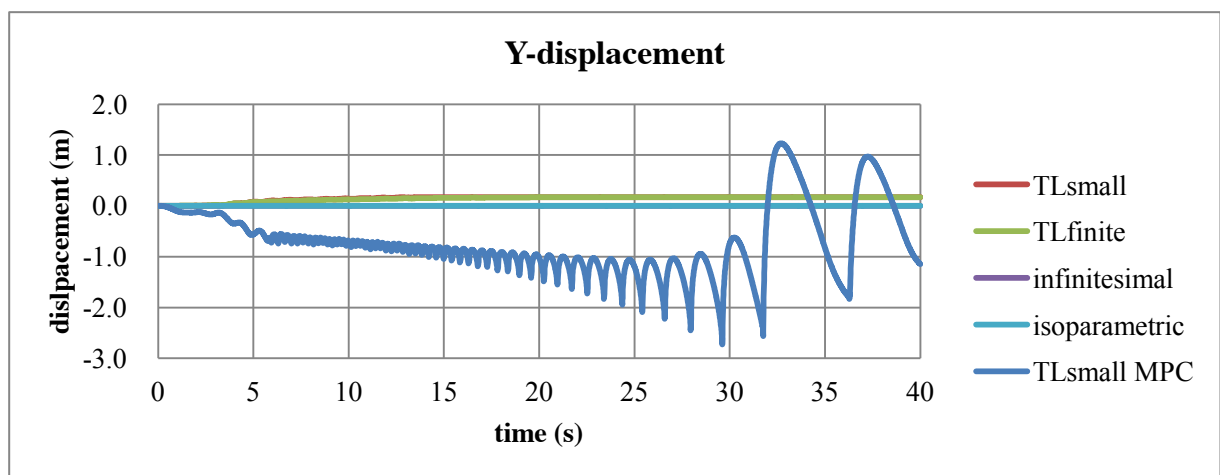
For TLfinite and TLsmall formulations, two distinct types of analyses were implemented, with the one difference being the MPC conditions at the bottom node of the SheetPile. The regular analyses contain these same MPC conditions, whereas in analyses marked as "modified MPC" movement is not constrained in the Y direction for any of the nodes in the beam.

Results show that this modification drastically effects the liquefaction mode, as shown in Fig. 6.27e. This behavior asserts the need for a better way to model the contact between soil and structure. One possible alternative would be to implement joint elements that fully transmit normal force (local normal direction) while only transmitting tangential frictional force (local tangent direction).

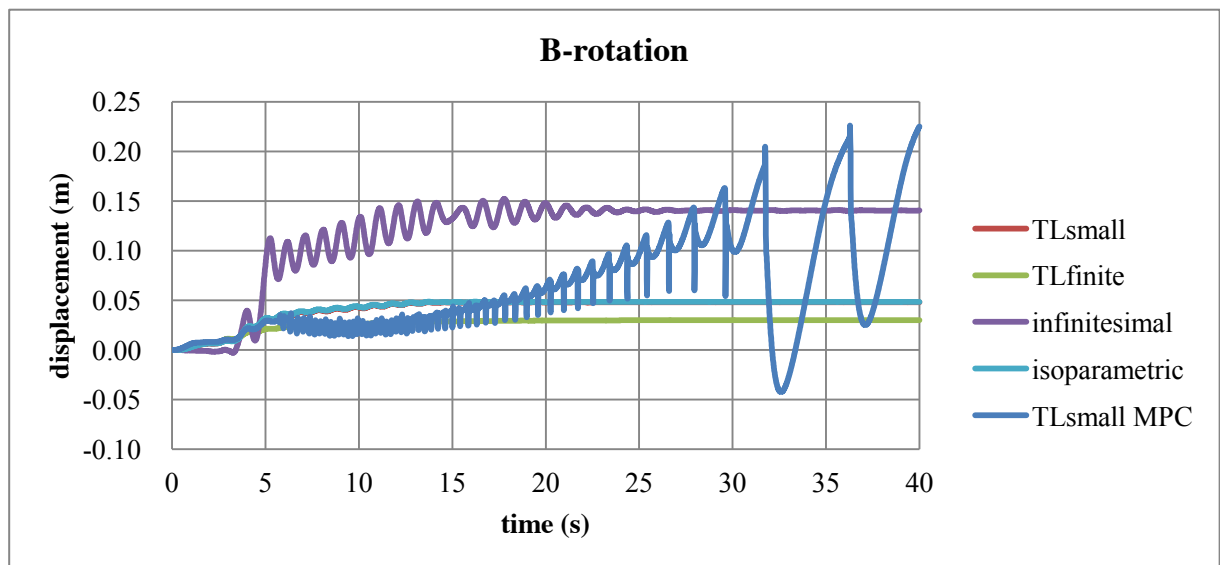
As of the time of this writing, analysis TLfinite with modified MPC conditions is still running.



(a)



(b)



(c)

Fig. 6.26 - Comparison of displacements for the top node of the beam for refined SheetPile LD-analysis.



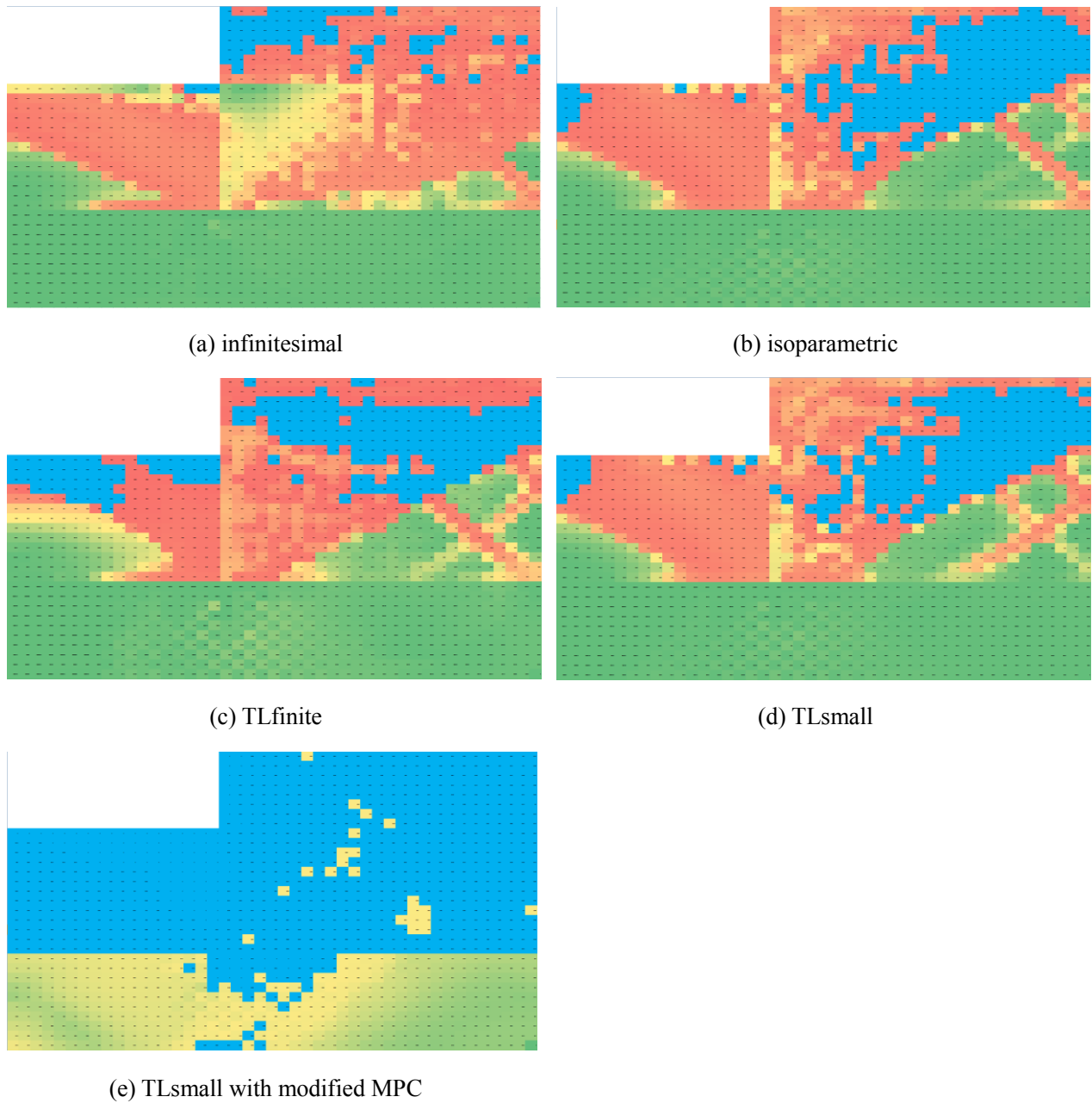


Fig. 6.27 - Comparison of elements that suffered liquefaction during refined LD-analysis (bright blue elements suffered liquefaction).

### 6.2.3 Conclusions

A recurring theme of LD-analysis and its refined counterpart seems to be the way in which changes to beam behavior strongly affect its surroundings. More importantly, the large displacement beam element implements extra functionality and extra complexity in the analysis. This is accompanied by incorrect collateral effects such as the positive Y-displacement observed in Fig. 6.24b.

## 7 Conclusions & Afterword

This work was a step into the unknown territory of large displacement analysis, and as such its tone is more exploratory than explanatory. The initial phase of formulation and implementation were highly involved tasks, mostly composed of mathematical and programming technicalities. The subsequent phases were focused on proof-testing the proposed elements, and thus ascertaining their sturdiness. Although the elements showed numerically sound behavior, their implementation in SSI analyses revealed the tip of an iceberg: the standard practices in small displacement analysis may or may be applicable to large displacement analysis.

Future lines of inquiry may then take two directions. The first would be to look for loose ends and further exploration in the behavior of large displacement elements. This direction leads to questions such as why there is a peak in deviation when an element's initial position is rotated in relation to the global coordinates, and to the search of possible alternatives or ways to implement the Update Lagrangian formulation for beam elements. The other direction points toward the application of the proposed elements to full-fledged soil-structure interaction analysis. In this case, the following questions would in the order of the day: which beam formulation should be adopted for each distinct type of analysis, what liquefaction modes best correspond to experimentally observed behavior, and what are the benefits and caveats of plucking a single large displacement element within analyses that by and large follow standards set for small displacements.

These are a few possible lines of inquiry for future research. Furthermore, the proposed elements require extensive testing prior to being adopted in the industry.

## References

- 1) HOLZAPFEL, Gerhard A. *Nonlinear Solid Mechanics: a continuum approach for engineering*, John Wiley & Sons: 2007.
- 2) ZIENKIEWICZ, O. C., TAYLOR, R. L. & ZHU, J. Z. *The Finite Element Method: Its Basis & Fundamentals*, Elsevier Butterworth-Heinemann: 2005.
- 3) ZIENKIEWICZ, O.C. & TAYLOR, R. L. *The Finite Element Method: For Solid and Structural Mechanics*, Elsevier Butterworth-Heinemann: 2005.
- 4) BATHE, Klaus-Jurgen. *Finite Element Procedures*, Prentice-Hall: 1996.
- 5) COUNIHAN, Martin. *Fortran 95*, Taylor & Francis: 2007.
- 6) METCALF, Michael, REID, John, COHEN, Malcolm. *Modern Fortran Explained (Numerical Mathematics and Scientific Computations)*, Oxford University Press: 2011.
- 7) ANDRUS, Ronald D., STOKOE, Kenneth H., CHUNG, Riley M. *Draft Guidelines for Evaluating Liquefaction Resistance Using Shear Wave Velocity Measurements and Simplified Procedures*, National Institute of Standards and Technology: 1999.
- 8) LAMBE, T. William, WHITMAN, Robert V. *Soil Mechanics*, John Wiley & Sons: 1969.
- 9) FRANKLIN, Cora Elena Martinez. *A Theoretical and Numerical Evaluation of Nonlinear Beam Elements*, MIT Press: 1997.
- 10) LEE, Haengsoo, JUNG, Dong-Won, JEONG, Jin-Ho & IM, Seyoung. *Finite Element Analysis of Lateral Buckling for Beam Structures*, Computers & Structures, Vol. 53, No. 6, pp.1357-1371, 1994.
- 11) IAI,S., MATSUNAGA,Y. and KAMEOKA,T.: *Strain space plasticity model for cyclic mobility* , Report of the Port and Harbour Research Institute, Vol.29, No.4, pp.27-56, 1990.
- 12) IAI,S., MATSUNAGA,Y. and KAMEOKA,T.: *Parameter identification for a cyclic mobility model*, Report of the Port and Harbour Research Institute, Vol.29, No.4, pp.57-83, 1990.
- 13) HAN, Seon M., BENAROYA, Haym & WEI, Timothy. *Dynamics of Transversely Vibrating Beams Using Four Engineering Theories*, Journal of Sound and Vibration, Vol.25, No.5 ,pp.935-988, 1990.

## Thanks

The accomplishment of the present work would not have been possible without the invaluable guidance and patience of the professors in the Geotechnics Laboratory in the Disaster Prevention Research Institute of Kyoto University: Prof. Susumu Iai, Assistant Professor Tetsuo Tobita and Associate Professor Mamoru Mimura. I'd like to thank especially Prof. Iai and Prof. Tobita, who were always there when the author needed the most.

Also of paramount importance was Kyohei Ueda, alumni of our Geotechnics Laboratory and presently a member of the Port and Airport Research Institute.

To the all students, professors and staff present during this course, my deepest and sincerest thanks.